A Micromachined Wide-Range Vacuum Sensor Employing Phase-Sensitive Detection

by

Priti Pal Singh Juneja
B.Sc.Eng. (Honours), Aligarh Muslim University, India, 1988

A THESIS SUBMITTED IN PARTIAL FULFILLMENT OF
THE REQUIREMENTS FOR THE DEGREE OF
MASTER OF APPLIED SCIENCE

in the School
of
Engineering Science

© Priti Pal Singh Juneja 1993
Simon Fraser University
December 1993

All rights reserved. This thesis may not be
reproduced in whole or in part, by photocopy or
by other means, without the permission of the author.

Approval

Name: Priti Pal Singh Juneja

Degree: Master of Applied Science (Engineering Science)

Title of Thesis: A Micromachined Wide-Range Vacuum Sensor Employing Phase-Sensitive Detection

Examining Committee: Dr. John D. Jones, Chair

Dr. Glenn H. Chapman
Senior Supervisor

Dr. Marek J. Syrzycki
Supervisor

Dr. M. Parameswaran
Examiner

Date Approved: December 24, 1993

PARTIAL COPYRIGHT LICENSE

I hereby grant to Simon Fraser University the right to lend my thesis, project or extended essay (the title of which is shown below) to users of the Simon Fraser University Library, and to make partial or single copies only for such users or in response to a request from the library of any other university, or other educational institution, on its own behalf or for one of its users. I further agree that permission for multiple copying of this work for scholarly purposes may be granted by me or the Dean of Graduate Studies. It is understood that copying or publication of this work for financial gain shall not be allowed without my written permission.

Title of Thesis/Project/Extended Essay

"A Micromachined Wide-Range Vacuum Sensor Employing Phase-Sensitive Detection"

Author:

(signature)

Priti Pal S. Juneja
(name)

December 24, 1993
(date)

Abstract

The measurement of vacuum levels is of considerable importance with applications in both scientific and industrial areas. This thesis explores the development of a CMOS-compatible micromachined vacuum sensor. The sensor has maximum sensitivity from 100 Torr to 10^{-2} Torr. It has extended range from 100 Torr to 760 Torr, and from 10^{-2} Torr to below 10^{-4} Torr at lower sensitivity. It employs a novel design, and measures the pressure-dependent heat flow from a thermally isolated micro heater across a 6 μm gap to a sense resistor. The sensor's rapid thermal response allows the application of phase-sensitive AC measurement technique, and enables detection of temperature changes of less than 0.5 millidegree Celsius. This measurement technique also eliminates the various compensations required by the Wheatstone-bridge method, widely employed in existing vacuum gauges. Thermal modeling of the device has been done using ANSYS, and it confirmed that average temperature change of less than 0.5 millidegree Celsius at the sense resistor can be detected.

The purpose of this research was two-fold: to verify the use of AC phase-sensitive technique in micro heater-sensor combination, and to test its application to the new vacuum sensor design. This thesis considers the significant sensitivity gain, and the wide-range of vacuum sensor obtained by applying an alternating current driving signal to the heater and measuring only the resulting AC change in the sensor.

Dedicated to ....

my mother, Prakash Kaur Juneja

my father, Balwant Singh Juneja

my brother, Ravneet Singh Juneja

my uncle, Amarjit Singh Chhabra

my Canadian mom, Rose Robin

my Canadian dad, Peter Robin

my Canadian aunt, Lindi Lewis

my Canadian uncle, Don Lewis

and a sweet friend, Brigitte Rabold

Acknowledgments

I wish to express my sincere appreciation to Dr. Glenn Chapman for his encouragement and direction throughout the research. I also wish to thank Dr. Marek Syrzycki, Dr. Ash Parameswaran and Dr. John Jones for their useful comments. I would also like to thank Dr. Andrew Rawicz, Ms. Sylvia Wessel, Mr. Steve Prescesky, Mr. Gary Houghton, Mr. Zi Xie, Mr. Bill Woods and Ms. Stephanie Chong for their help during various stages of the research. In addition, I offer thanks to Canadian Microelectronics Corporation for providing the access to NTE's CMOS3 DLM process for the fabrication of various devices.

This research project was funded by a grant from British Columbia Advanced Systems Institute.

Table of Contents

Approval ii

Abstract iii

Acknowledgments v

List of Tables viii

List of Figures ix

1 Introduction 1

- 1.1 Conventional Vacuum Gauges 3
- 1.2 Silicon Vacuum Gauges 6
- 1.3 Scope of Thesis 15

2 Principle and Design 16

- 2.1 Heat Flow in Rarefied Gases 16
- 2.2 Design and Fabrication 21
- 2.3 Measurement Technique's Requirement 32
- 2.4 Phase-Sensitive Detection 36

3 Experiments and Results 41

- 3.1 Temperature Coefficient of Resistivity 41
- 3.2 AC Measurement on Microstructures 43
- 3.3 The Vacuum System 46
- 3.4 Thermal Time Constant 47
- 3.5 Frequency of Operation 50
- 3.6 Sensing Signal 52
- 3.7 A Sample Calculation 55
- 3.8 Comparison of Various Structures 59
- 3.9 Minimum Temperature Change 60
- 3.10 Orientation Dependent Heat Transfer 63
- 3.11 Response at Various Pressures 64
- 3.12 Constant Voltage Operation 64

3.13 Constant Temperature Operation 67
3.14 Response in Nitrogen and Argon 72
3.15 Summary 72

4 Modeling 74
4.1 Finite Element Analysis 74
4.2 Thermal Analysis 76
4.3 Thickness of Various Layers 76
4.4 Thermal Conductivity of Various Layers 78
4.5 2-D Modeling using ANSYS 81
4.6 Modeling of 1 Plate Beam-type Poly Resistor Structure 86
4.7 Modeling of 3 Plate Beam-type Poly Resistor Structure 95
4.8 Summary 95

5 Analysis and Future Work 98
5.1 Saturation of the Output 98
5.2 Radiative Heat Transfer 99
5.3 Crosstalk 99
5.4 Electromagnetic Induction 102
5.5 Outgassing 103
5.6 Future Work 105

6 Conclusion 107

Appendix 108
Appendix A: CDL Program 108
Appendix B: Integrated Circuit Designs 116
Appendix C: ANSYS Finite Element Listings 120
C.1 ANSYS 4.4 Input Listing for Thermal Conductivity Mergence Example 120
C.2 ANSYS 4.4 Input Listing for Modeling of Structure 1 Plate Beam-type Polysilicon Resistor 123
C.3 ANSYS 4.4 Input Listing for Modeling of Structure 3 Plate Beam-type Polysilicon Resistor 127

List of References 131

List of Tables

Table 1.1 Vacuum pressure range subdivision and applications 2

Table 2.1 Dimensions of various micromachined structures designed 26

Table 3.1 Slope and intercepts of sensor output at 700 Torr and 10^{-5} Torr for sensing signal of strengths 0.1 mA, 0.2 mA and 0.4 mA 52

Table 3.2 Measured heater power dissipation, lock-in output and the estimated temperature change of sense resistor for Sample 1 at 700 Torr 61

Table 4.1 Thickness of various layers of NT's CMOS3 DLM integrated circuit fabrication process 77

Table 5.1 Crosstalk measurements 100

List of Figures

Figure 1.1 Typical operating range of conventional vacuum gauges 2
Figure 1.2 Thermocouple, Pirani and ionization gauge 5
Figure 1.3 Silicon membrane-type pressure sensors 8
Figure 1.4 Micromachined silicon vacuum sensors 10
Figure 1.5 Micromachined silicon vacuum sensors 11
Figure 1.6 Micromachined silicon gas flow sensors 14
Figure 1.7 Schematic cross-sectional view of proposed micromachined vacuum sensor 14
Figure 2.1 Molecular density, mean free path and molecular incidence rate versus pressure 19
Figure 2.2 Schematic of proposed measurement of heat flow 20
Figure 2.3 Schematic of structure 1 plate meander-type polysilicon resistor 22
Figure 2.4 Schematic of cross-sectional view of structure1 plate meander-type polysilicon resistor after etching 23
Figure 2.5 Schematic of proposed placement of the designed ICs IC3SFCP1 and IC3SFCP2 25
Figure 2.6 Schematic of structure 2 plate meander-type polysilicon resistor 28
Figure 2.7 SEM photograph of etched 2 plate meander-type polysilicon resistor structure 29
Figure 2.8 Schematic of structure 1 plate beam-type polysilicon resistor 30
Figure 2.9 SEM photograph of etched 1 plate beam-type polysilicon resistor structure 31
Figure 2.10 Schematic of structure 3 plate beam-type polysilicon resistor 33
Figure 2.11 SEM photograph of etched 3 plate beam-type polysilicon resistor 34
Figure 2.12 SEM photograph of etched 3 plate meander-type polysilicon resistor structure 35
Figure 2.13 Block diagram of major components of a lock-in amplifier 38
Figure 3.1 Change in resistance of polysilicon with temperature 42
Figure 3.2 Circuit set-up for measuring the output voltage, and induced heat transfer from the heater resistor to the sense resistor 45
Figure 3.3 Schematic diagram of the vacuum system 47
Figure 3.4 Applied square-pulse heater current and the corresponding sense resistor AC current 49

Figure 3.5 Line-fit to the downloaded data points of sense AC signal to obtain the time constant of the microstructures 51
Figure 3.6 Response of sensor to sensing signal of amplitudes 0.1 mA, 0.2 mA and 0.4 mA at 700 Torr 53
Figure 3.7 Response of sensor to sensing signal of amplitudes 0.1 mA, 0.2 mA and 0.4 mA at 10^{-5} Torr 54
Figure 3.8 Comparison of response of various structures designed for investigation as a vacuum sensor 59
Figure 3.9 Output voltage and the estimated average temperature change of sense resistor for various power dissipation in the heater resistor at 700 Torr 60
Figure 3.10 Output voltage and the estimated average temperature change of sense resistor for various power dissipation in the heater resistor at various pressures 62
Figure 3.11 Output voltage and the estimated average temperature change of sense resistor for various orientations at 700 Torr 63
Figure 3.12 Output voltage and the estimated average temperature change of sense resistor with pressure for constant voltage operation of the heater resistor 65
Figure 3.13 Heater temperature variation with pressure for constant voltage operation of the heater resistor 66
Figure 3.14 Output voltage and the estimated average temperature change of sense resistor with pressure of Sample 1 for constant heater temperature excitation of 200° C, 125° C, 75° C and 40° C 68
Figure 3.15 Output voltage and the estimated average temperature change, on magnified scale, of sense resistor with pressure of Sample 1 for constant heater temperature excitation of 200° C and 40° C 69
Figure 3.16 Output voltage and the estimated average temperature change of sense resistor with pressure of Sample 2 for constant heater temperature excitation of 200° C, 125° C, 75° C and 40° C 70
Figure 3.17 Output voltage and the estimated average temperature change, on magnified scale, of sense resistor with pressure of Sample 2 for constant heater temperature excitation of 200° C and 40° C 71
Figure 3.18 Comparison of sensor response in nitrogen and argon atmosphere for constant heater temperature excitation of 125° C and 40° C 73

Figure 4.1 SEM photograph of the cross-section of a beam-type polysilicon resistor 77
Figure 4.2 Thermal conductivity of SiO_2, polysilicon and metal layers 80
Figure 4.3 Equivalent 2-D ANSYS model of the example 3-D structure 82
Figure 4.4 Temperature distribution obtained by ANSYS for 3-D model of the example structure 83
Figure 4.5 Temperature distribution obtained by ANSYS for 2-D model of the example structure 85
Figure 4.6 2-D model of structure 1-plate beam-type polysilicon resistor generated using ANSYS 86
Figure 4.7 Material layers and their composition for the structure 1 plate beam-type poly resistor 88
Figure 4.8 Temperature distribution across the surface of structure 1 plate beam-type polysilicon resistor at 3×10^{-7} Torr 90
Figure 4.9 Comparison of experimental and modeling values of average temperature change of sense resistor at 3×10^{-7} Torr for the structure 1 plate beam-type poly resistor 91
Figure 4.10 Model of structure 1 plate beam-type poly resistor, showing 3-D conduction elements, used for simulation of heat transfer at room pressure 92
Figure 4.11 Temperature distribution across the surface of structure 1 plate beam-type polysilicon resistor at 700 Torr 93
Figure 4.12 Comparison of experimental and modeling values of average temperature change of sense resistor at 700 Torr for the structure 1 plate beam-type poly resistor 94
Figure 4.13 Top view of the ANSYS model of structure 3 plate beam-type poly resistor 96
Figure 4.14 Comparison of experimental and modeling values of average temperature change of sense resistor at 700 Torr for the structure 3 plate beam-type poly resistor 97
Figure 5.1 Circuit setup to measure crosstalk 100
Figure 5.2 Rise time of heater current 102
Figure 5.3 Comparison of output voltage measured before and after degassing of a sample device at 100° C 104
Figure 5.4 Proposed improvement in design by back-etching the silicon substrate to open the cavity 106

1 Introduction

A vacuum is a space filled with gas at below atmospheric pressure, i.e. the space has a density of molecules less than 2.5 x 10^{19} molecules/cm^3 [1]. A 'perfect' vacuum is the total absence of gaseous fluid, an unattainable condition in practice. Even at lowest pressures that can be obtained by modern pumping methods there are still hundreds of molecules in each cm^3 of the evacuated space. The degree of vacuum attained in a system is most often characterized by the absolute gas pressure in the system[2], and is given by the expression

$$P = \frac{1}{3} n m \left(\frac{8kT}{\pi m} \right)^2 \quad (1.1)$$

where n is the concentration and m is the molecular mass of the gas particles, k is Boltzmann's constant, and T is the absolute temperature[3]. The System Internationale (SI) pressure unit is *pascal* (Pa), and is equal to 1 Newton/m^2. SI also accepts *bar* as a pressure unit. *Torr* is another widely used unit to discuss high, very high and ultra high vacuum levels. One Torr is a gas pressure able to balance 1 mm of Hg at 0° C. These units are related as

$$1 \text{ Pascal} = 10^{-5} \text{ Bar} = 7.5 \times 10^{-3} \text{ Torr} \quad (1.2)$$

Vacuum technology is used in an array of processes such as railway brakes, lamp manufacturing, electronics, deposition of various thin films, etching, molecular distillation, metallurgy, dehydration and surface physics[4]. The pressure may vary from 760 Torr to below 10^{-16} Torr for the various processes, and can be sub-divided into several ranges, as shown in Table 1.1 .

Physical situation	Pressure range (Torr)			Applications
Low vacuum	750	→	25	Pneumatic, Dehydration, Holding, Filtering, Cleaning, Moulding
Medium vacuum	25	→	7.5×10^{-4}	Lamps, Melting, Sintering, Encapsulation, Leak detection
High vacuum	7.5×10^{-4}	→	7.5×10^{-7}	Molecular distillation, Sputtering, Space simulation, Insulation
Very High vacuum	7.5×10^{-7}	→	7.5×10^{-10}	Accelerators, Mass spectrometers, Electron microscopes
Ultra High vacuum	7.5×10^{-10}	→	below	Surface physics studies - Friction & Adhesion, Molecular beam epitaxy

Table 1.1 - Vacuum pressure range subdivision and applications.

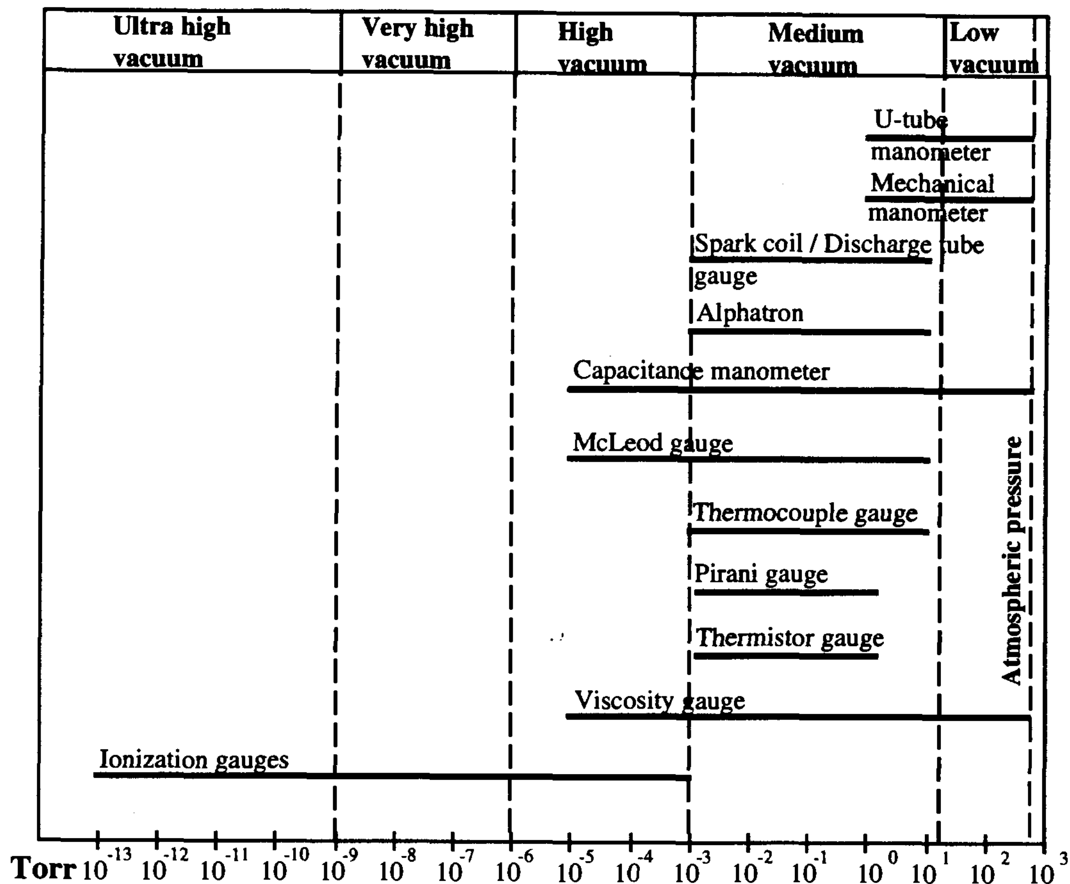

Figure 1.1 - Typical operating range of conventional vacuum gauges.

1.1 Conventional Vacuum Gauges

The instruments used to measure absolute pressures from 760 Torr to below 10^{-12} Torr are known as *vacuum gauges.* There is no universal gauge that can measure pressure from atmospheric to ultra high vacuum. The instrument chosen to measure pressure depends on the range, and the gas composition. Mechanical gauges, in which a liquid or a solid diaphragm is moved by the force exerted by the gas molecules, give absolute pressure measurements unaffected by the gas composition. Unfortunately, they are ineffective below 10^{-5} Torr as the force exerted by the gas molecules becomes very weak. Gauges that measure some bulk gas property such as heat conduction and viscosity give readings that are dependent on gas composition. They are effective over limited pressure ranges below approximately 100 Torr and above 10^{-4} Torr. Gauges suitable for high vacuum to ultra-high vacuum measurement use charge collection phenomenon. The residual gas molecules are ionized and the resulting current is measured.

The chart (see Figure 1.1) gives the approximate pressure range covered by various vacuum gauges. The principle of operation, advantages and disadvantages of these gauges[5] are discussed briefly below.

U-tube manometers measure the height of a liquid in communicating tubes, and these can measure the pressure down to 10^{-2} Torr. These have the advantage of direct reading independent of the nature of gas, but have limited accuracy.

Mechanical manometers, such as Bourdon gauges, measure the elastic bending of a tube, or a diaphragm, and can measure pressures down to 10^{-2} Torr. These offer the advantage of gas-independent direct reading but suffer from limited accuracy, elastic after-effects and temperature-dependence.

Spark coil or discharge tube gauges use the pattern and colour of an electric discharge as an indication of the pressure. These are simple to operate but provide only a very rough qualitative pressure indication and the readings are gas-dependent.

Alphatrons measure the electric current generated by the ionization of a gas caused by α-particles released from a radio-active source such as radium. These have the advantages of direct reading and a very consistent calibration curve. However, these

require precautions in using the gauge to avoid possible physiological effects arising from the radium emanation, and readings are dependent on the nature of the gas.

Capacitance manometers use the electrical capacitance between a diaphragm and a stationary electrode to precisely measure the diaphragm's movement. These devices are mechanically similar to mechanical manometers but are more sensitive. These are quite accurate devices for measuring the differential pressure (with a known gas pressure on the reference side), or absolute pressure (with a vacuum on the reference side). The drawbacks are cost, requirement of a reference pressure, high sensitivity to temperature and a dynamic range of approximately 10^4 Torr for any one gauge head[6].

McLeod compression gauges measure the volume of a known gas quantity after compression and provide the sum of partial pressures of non-condensable gases. These offer the advantage of extracting calibration curves from the dimensions of the gauge. These gauges are widely used as a standard for gauge calibration. McLeod compression gauges are bulky in design, complex in operation, cannot be used for continuos pressure indication and the condensation of vapour in the gauge prevents measurement of total pressure.

Thermocouple gauges measure the thermoelectric EMF generated in one or more thermocouples in contact with a constant-wattage heated filament (see Figure 1.2a). A change in pressure alters the thermal conductivity of the gas, and subsequently the temperature of the heater. This alters the temperature of the thermocouple and hence its EMF. The heating filament operates at high temperatures of about 200° C[1] at 10^{-3} Torr and the conduction saturates as the radiative heat transfer, which is independent of pressure, starts dominating. The disadvantages of thermocouple gauges are variation of pressure reading caused by the contamination of the thermocouple surface, a short working range and gas-dependent readings.

Pirani gauges measure the electrical resistance of a heated wire which forms one branch of a Wheatstone bridge (see Figure 1.2b). A second resistor in a tube sealed at a fixed low pressure forms the reference resistor arm of the bridge. A change in pressure alters the temperature of the heated wire and hence its resistance. These are operated in either constant current or constant temperature mode, and the conduction saturates at 10^{-3} Torr when radiative heat transfer, which is independent of pressure starts dominating. The disadvantages of the Pirani gauges are variation of pressure reading caused by the

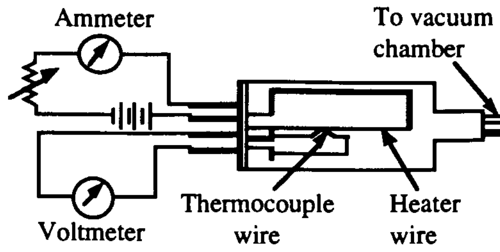

Figure 1.2a - Thermocouple gauge.

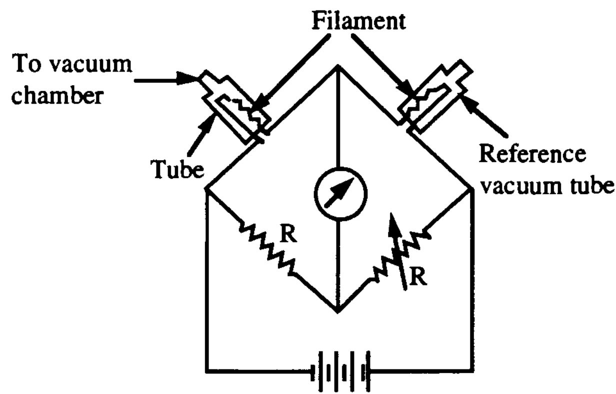

Figure 1.2b - Pirani gauge.

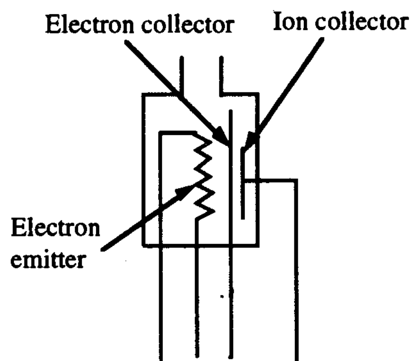

Figure 1.2c - Ionization gauge.

Figure 1.2 - Thermocouple, Pirani and ionization gauge.

contamination of the metal surfaces in the gauge, alteration of calibration curve during usage, a short working range and gas-dependent readings.

Thermistor gauges are similar to the Pirani gauges but instead of a resistance wire a semiconductor bead, because of its higher temperature coefficient of resistance, is used as a temperature-sensing element. The influence of surface contamination of the semiconductor bead is much less than on the heated wire used in the Pirani gauges. However, semiconductor beads have the disadvantage of greater mass than resistance wires, and hence slower thermal response time.

Viscosity gauges use the phenomenon of pressure dependence of gas viscosity and measure either the damping of oscillations in a quartz fiber or the current in a constant amplitude oscillating ribbon. These do not contain hot or cold metal parts which can cause cracking of the gas molecules in case of non-monatomic gases, or gas clean-up, respectively. Their disadvantages are sensitivity to vibrations, superimposed oscillations, extraneous magnetic field interference and gas-dependent response.

For pressure measurements below 10^{-3} Torr ionization gauges are employed (see Figure 1.2c). These gauges measure the electric current generated by the ionization of the gas molecules caused by electrons emitted from a hot filament or by a glow discharge. Their advantage is the ability to measure the pressure in the high to ultra high range. However, these are expensive and are easily damaged if used at pressures above 10^{-3} Torr as the filament is likely to burn out because of oxidation and bombardment by the positive ions formed in the space between the cathode and the grid. They also require frequent degassing, common to all high vacuum gauges, for accurate measurements and gas-dependent readings. Degassing is the removal of adsorbed gases by increasing the grid temperature to as high as 1000° C.

1.2 Silicon Vacuum Gauges

A wide range of micro electromechanical devices are emerging from the technology developed for integrated circuits. Micromotors, accelerometers, gas chromatographs, torsional mirrors, ink jet nozzles, microbridges, membranes, cantilever beams, orifices, pits, pyramids, and other structures[7,8,9] of the size of a fraction of a millimeter are being fabricated by researchers in the micromachining field. The technology to fabricate these

three-dimensional silicon based microstructures uses a combination of chemical and plasma etching, substrate bonding techniques, inter-layer connections, and various standard integrated circuit manufacturing processes such as photolithography and thin-film deposition[10]. When fabricated on silicon substrates these actuators can easily be coupled with on-substrate signal-processing circuitry to realize 'smart sensors'[11]. Thus far, the silicon diaphragm pressure sensor has been the main commercial success with many uses in the medical equipment, energy management, automotive, avionics, and process-control industries.

Basically, there are two types of silicon pressure sensors employed to measure below atmospheric pressure. The first type utilizes the excellent elastic and piezoresistive property of silicon material[7] and uses a membrane, enclosing a cavity of reference vacuum (see Figure 1.3a). The membrane carries a suitably placed resistor bridge (see Figure 1.3b) or a ring oscillator (see Figure 1.3c) on it[12,13]. These vacuum sensors are similar to the mechanical and capacitive manometers in their principle of operation. The deflection of the membrane due to the pressure causes a change in the resistance due to the piezoresistive effect, and hence gives the measure of the pressure. These sensors are employed widely to measure pressure from 75 Torr and higher. They fail to measure lower pressures due to insignificant deflection of the membrane resulting in undetectable resistor change. However, with special designs employing bossed diaphragms and precision etch-stop, pressures down to 5 Torr can be measured[14].

The second type is based on the pressure dependence of the heat transfer from a heated element through a gas. This thermal flow is directly proportional to the pressure below approximately 10 Torr when the mean free path of molecules becomes larger than the spacing between opposite surfaces[1]. Conventional thermocouple, Pirani, and existing silicon micromachined thermal vacuum gauges operate on this principle. Compared to silicon micromachined thermal vacuum gauges, thermocouples have slow response, high power consumption and a short working range of 4 decades of pressure as the conduction saturates at 10^{-3} Torr when the radiative heat transfer, which is independent of pressure, starts dominating.

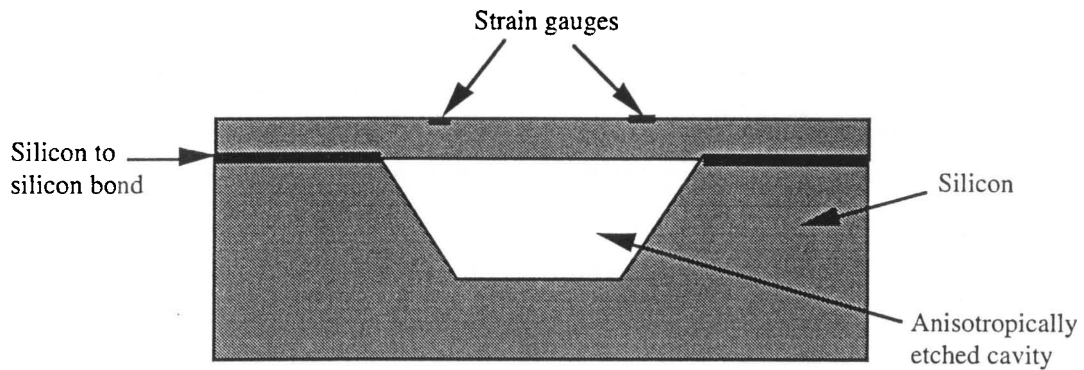

Figure 1.3a - Schematic diagram of a silicon membrane-type pressure sensor.

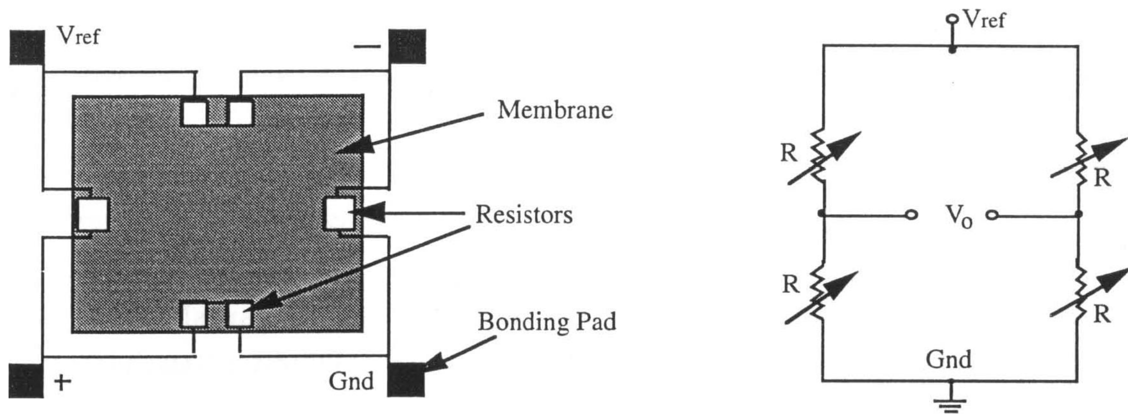

Figure 1.3b - Top view of a pressure sensor with a suitably placed resistor bridge[12].

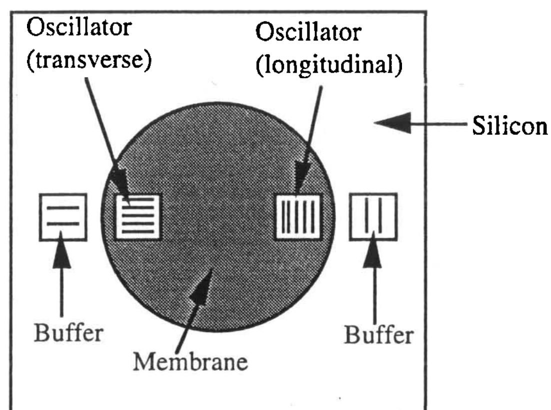

Figure 1.3c - Top view of a pressure sensor with suitably placed ring oscillators[13].

Figure 1.3 - Silicon membrane-type pressure sensors.

The various vacuum sensors reported in the silicon micromachining literature by some of the major researchers are summarized below.

A.W. van Herwaarden, P.M. Sarro and H.C. Meijer[15] report a vacuum sensor which employs an n-type heating resistor and thermopiles on a p-type substrate etched to form a cantilever or a membrane. A thermopile is a group of thermocouples connected in series or in parallel. These are placed in proximity to the heater (see Figure 1.4a and 1.4b) to detect change in the temperature of the cantilever or the membrane with change of pressure. The range of operation is from 750 Torr to 10^{-4} Torr but the device suffers from saturation effects which decrease its sensitivity at pressure higher than 1 Torr.

More recently, A.W. van Herwaarden, D.C. van Duyn and J. Groeneweg[16] report a much smaller and more sensitive vacuum sensor with an improved design of the membrane (see Figure 1.4c) incorporating longer bridge arms. This design provides better thermal isolation from the substrate thereby increasing the sensitivity. The device has the same range of 750 Torr to 10^{-4} Torr but the saturation effect does not dominate until pressures of 75 Torr or greater.

C.H. Mastrangelo and R.S. Muller[17] report a heated microbridge type vacuum sensor fabricated in NMOS technology with signal processing circuitry on the same chip. A beam-type polycrystalline (poly) silicon resistor (see Figure 1.5a) is used to heat the SiN coated silicon dioxide bridge at constant temperature and the change in power with pressure is interpreted as a measure of the absolute gas pressure. The chip provides digital output but has a short working range of 75 Torr to 0.75 Torr.

Huang Jin-Biao and Tong Qin-Yi[18] report a multifunction sensor for flow, temperature and vacuum measurements fabricated using a conventional CMOS process. This design is based on the amount of heat transfer from a chip at constant temperature to the ambient. A diode coupled with an operational amplifier on the chip is used to measure the temperature, but the device has a short operating range of 760 - 10^{-1} Torr.

A.M. Robinson, P. Haswell, R.P.W. Lawson and M. Parameswaran[19] report a thermal conductivity microstructural pressure sensor fabricated in CMOS (complimentary metal-oxide-semiconductor) technology and operated as a Pirani gauge. A polysilicon 'meander-type' resistor (see Figure 1.5b) is used to heat the thermally isolated micro bridge which is aluminum coated to produce a more uniform distribution of heat. The device is

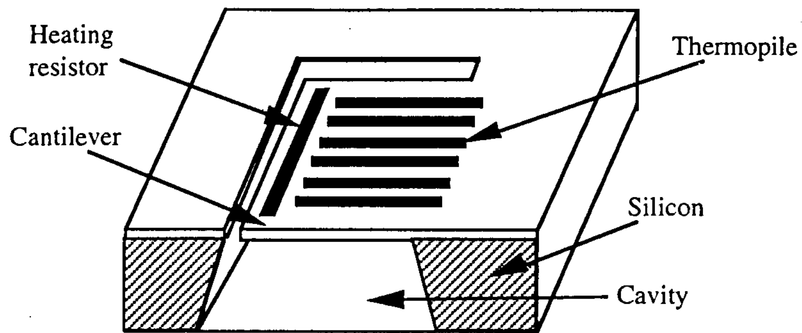

Figure 1.4a - Schematic drawing of an electrochemically etched cantilever-beam vacuum sensor reported by A.W. van Herwaarden, P.M. Sarro and H.C.Meijer[15].

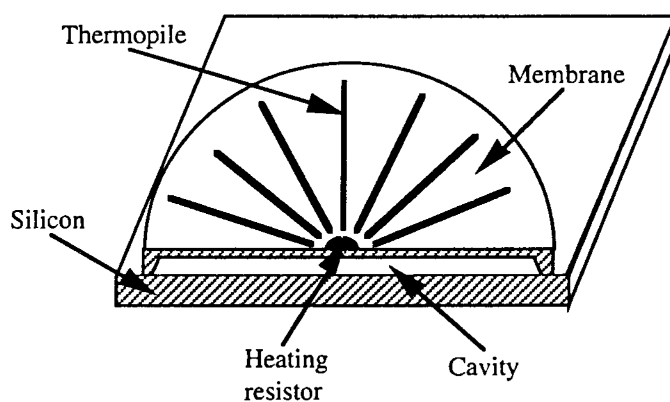

Figure 1.4b - Schematic drawing of a membrane vacuum sensor reported by A.W. van Herwaarden, P.M. Sarro and H.C. Meijer[15].

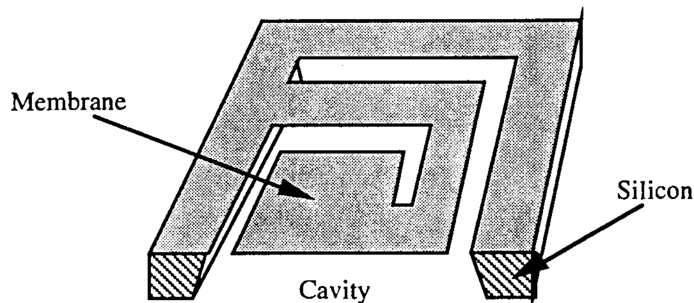

Figure 1.4c - Schematic drawing of a floating-membrane structure vacuum sensor by A.W. van Herwaarden, D.C. van Duyn and J. Groeneweg[16].

Figure 1.4 - Micromachined silicon vacuum sensors.

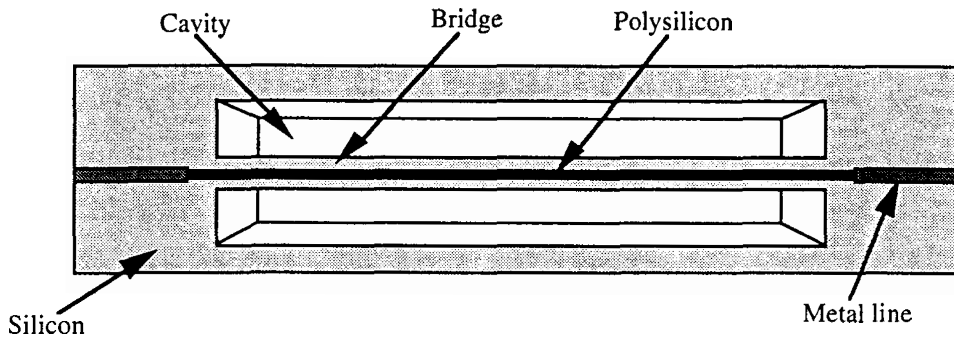

Figure 1.5a - Top view of the microstructure vacuum sensor reported by C.H. Mastrangelo and R.S. Muller[17].

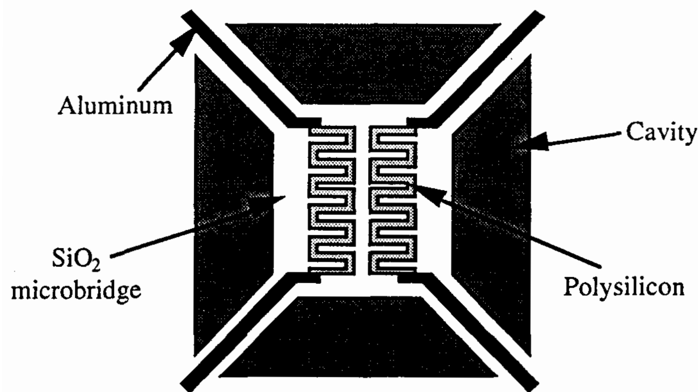

Figure 1.5b - Top view of the CMOS vacuum sensor microstructure reported by A.M. Robinson, et al[19].

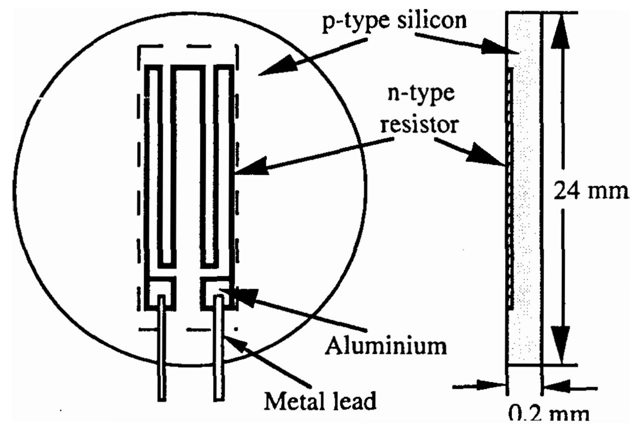

Figure 1.5c - Schematic view of the vacuum gauge head reported by J. Bretschi[21].

Figure 1.5 - Micromachined silicon vacuum sensors.

operated in constant current mode and the change in voltage with pressure is measured directly. The device has a short working range of 100 - 0.01 Torr.

S.D. James, R.G. Johnson and R.E. Higashi[20] report a small size (6 μm x 90 μm) microbridge vacuum sensor for measurements above 1 Torr. The design of the bridge and the resistor is similar to that of Figure 1.5a . The sensor operates by measuring the change in power required to keep a thermally isolated silicon nitride microbridge heated by a beam-type, NiFe temperature sensitive resistor at constant temperature. A Wheatstone bridge, together with an error integrator, is employed to sense changes in the power necessary to keep the microbridge structure at constant resistance and therefore at a constant temperature. Its drawbacks are its inability to measure pressure below 1 Torr and the various Wheatstone-bridge compensations required.

Vacuum sensors made using thin film technology also show a good range and stability. J. Bretschi[21] reports a vacuum sensor which employs an n-type resistive network formed by solid state diffusion in p-type silicon substrate (see Figure 1.5c). A Wheatstone bridge is employed to measure the variation in the resistive network output with change in pressure. These have good stability and a broad working range of 760 to 10^{-5} Torr but are large in size (24 mm diameter wafer).

S.M. Patel and M.D. Mahajan[22] report a thin film vacuum sensor employing large area GaSb films deposited on glass or mica substrates. It employs a Wheatstone bridge to detect the resistance imbalances caused with change in temperature as pressure varies. The device has a range of 10 - 10^{-5} Torr. Its drawbacks are large area and non-silicon substrate which prevents the fabrication of the interface electronics on the same substrate.

A wide range of flow sensors based on the thermal conductivity principle have also been fabricated using silicon micromachining techniques. In many instances the same structure has also been used as a vacuum sensor. Thus flow sensors also provide an insight to the designs of the thermally isolated micromechanical structures which can be modified or extended to be used as a vacuum sensor element. A brief survey of flow sensors follows.

M. Parameswaran, A.M. Robinson, Lj. Ristic, K. Chau and W. Allegretto[23] describe a thermally isolated gas flow sensor fabricated using standard CMOS technology.

It has two polysilicon meander-type resistors on a thermally isolated SiO_2 bridge (see Figure 1.5b) similar to the design of the vacuum sensor described earlier[19]. A constant current is passed through one polysilicon resistor and due to the air flow a change in temperature of the bridge is reflected by the change in the resistance of the other resistor on the bridge.

T.R. Ohnstein, R.G. Johnson, R.E. Higashi, D.W. Burns, J.O. Holmen, E.A. Satren and G.M. Johnson[24] describe a wide dynamic range airflow sensor which uses three thin film platinum resistors - one as a heater and two meander-type sensor elements, one placed on either side of the heater, on a silicon nitride diaphragm (see Figure 1.6a).

B.W. van Oudheusden and A.W. van Herwaarden[25] describe a two-dimensional thermal flow sensor. It employs a heated resistor and thermopiles on a floating membrane similar to that of the vacuum sensor discussed earlier[16].

D. Moser, R. Lenggenhager and H. Baltes[26] describe CMOS and bipolar flow sensors consisting of a heated free-standing cantilever beam. The temperature difference between the tip of the cantilever heated by a polysilicon resistor and the bulk substrate is dominated by the gas flow rather than the thermal conduction through the cantilever, and is measured by a thermopile (see Figure 1.6b).

All the thermal sensors described above are based on the measurement of the heat loss in a heated resistor with change in pressure or flow of gas, and employ a thermopile or a Wheatstone bridge to detect the variations in the resistance. These resistance shifts are typically less than a few percent[19]. This fact requires care be taken in the design of the balance resistors, and temperature compensation of the load balances[27].

S. Middelhoek, P.J. French, J.H. Huijsing and W.J. Lian[28] discuss the advantages of silicon sensors with digital or frequency measurement technique. They propose that the integration of sensor elements and signal conditioning on one chip might eventually lead to a family of sensors with a microprocessor-compatible output, which can easily be applied in bus-organized data-acquisition systems. Frequency measurement techniques also have advantages in terms of noise and temperature-drift.

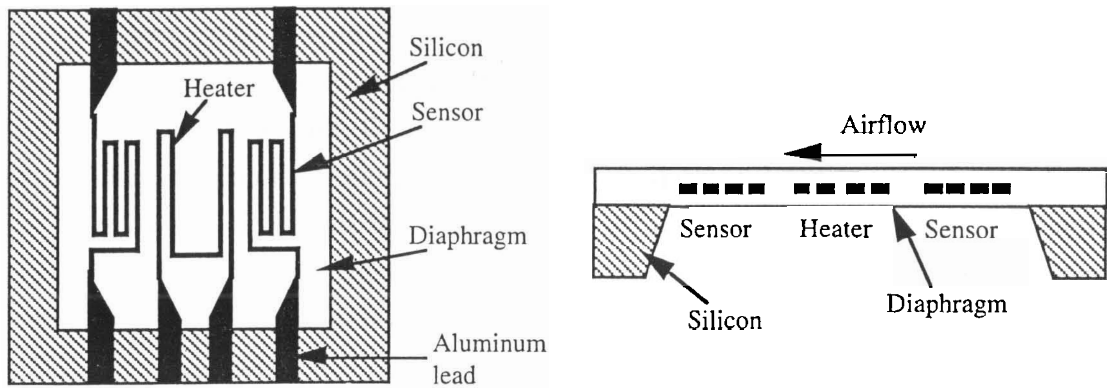

Figure 1.6a - Top and cross-sectional view showing the heater and sensor elements of the airflow sensor diaphragm reported by T.R. Ohnstein, et al[24].

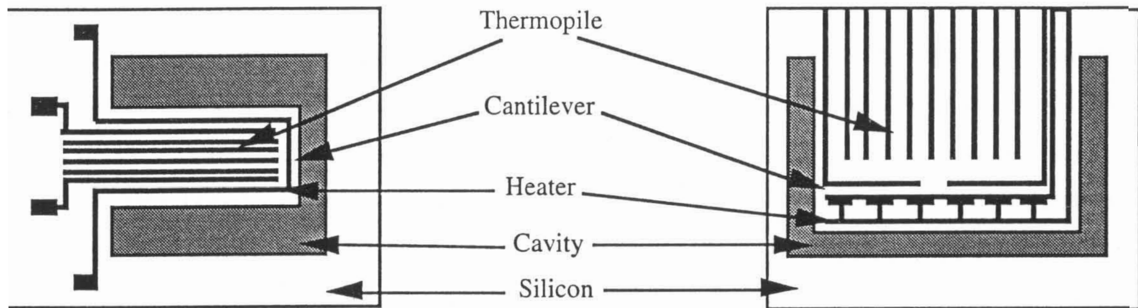

Figure 1.6b - Schematic view of the CMOS and bipolar gas flow sensors reported by D. Moser, et al[26].

Figure 1.6 - Micromachined silicon gas flow sensors.

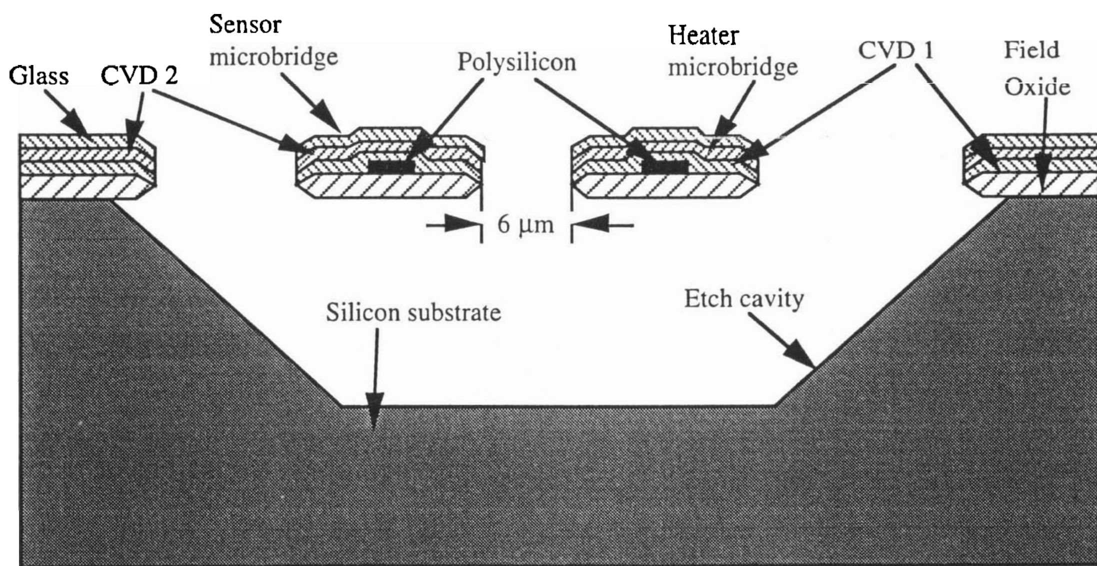

Figure 1.7 - Schematic cross-sectional view of proposed micromachined vacuum sensor.

Pressure sensors with frequency output have been designed but only for those based on mechanical deflection of the membrane. R. Schorner, M. Poppinger and J. Eibl[12] & J. Neumeister, G. Schuster and W. Von Munch[13] describe this kind of sensors. They employ ring oscillators suitably placed on a silicon membrane (see Figure 1.3c). With change in pressure the mechanical stress in the membrane changes thus altering the mobility of the charged carriers in the ring oscillator's MOSFETs and hence the drain current. This changes the delay time per inverting gate and the frequency of the ring oscillators becomes a function of the pressure.

1.3 Scope of Thesis

A typical arrangement of two gauges is required to cover the pressure range of 760 Torr to 10^{-7} Torr widely used in sputtering, etching and chemical vapour deposition. Some processes use a third gauge, a capacitance manometer for precise measurements in the range 10^{-1} Torr to 10^{-3} Torr for reproducible processing. It would be desirable to have a single vacuum gauge which covers the pressure range of 760 Torr to below 10^{-7} Torr, and is fabricated using a commercial batch silicon process to benefit from its advantages of small size and low cost.

We have developed a vacuum sensor that employs a unique design in which two thermally isolated microbridges, separated by a narrow gap, are suspended over a micromachined cavity (see Figure 1.7). The heat flow from one microbridge's resistor, kept at a higher temperature, across the gap to the other sense resistor microbridge is dependent on the concentration of molecules, and hence the pressure in the chamber. The sensor's small thermal inertia due to the micro size of the structure results in rapid thermal responses in the order of few milliseconds. This allows the application of phase-sensitive AC measurement techniques. The purpose of this research was two-fold: to test the operation of the new vacuum sensor design and to verify the use of AC phase-sensitive technique in micro heater-sensor combination. This thesis considers the significant sensitivity gained, and the wide-range of vacuum sensor obtained by using an AC driving signal to the heater and measuring only the resulting AC change in the sensor.

2 Principle and Design

In this chapter, theory of heat flow in rarefied gases and its application to the thermal conductivity gauges is discussed. The principle of operation of the proposed vacuum sensor, and the various structures designed for its realization are reported. The concept of phase-sensitive measurement technique is also introduced.

2.1 Heat Flow in Rarefied Gases

A heated object in a gaseous environment in a container can lose energy in three ways. The first energy loss is by thermal radiation to the walls of the enclosing container, and is given by

$$q_{rad} = \sigma A_1 \left(\varepsilon_1 T_1^4 - \varepsilon_2 T_2^4 \right) \tag{2.1}$$

where A_1 is the radiating area at temperature T_1, emissivity ε_1 of body 1 which radiates energy to body 2 of emissivity ε_2 at temperature T_2 [29], and σ is the Stefan-Boltzmann constant.

The second energy loss is by heat conduction through solids, such as support arms and connecting leads, and the general three-dimensional heat-conduction equation is given by

$$\frac{\partial}{\partial x}\left(k\frac{\partial T}{\partial x}\right) + \frac{\partial}{\partial y}\left(k\frac{\partial T}{\partial y}\right) + \frac{\partial}{\partial z}\left(k\frac{\partial T}{\partial z}\right) + q_{gen} = \rho c\frac{\partial T}{\partial \tau} \tag{2.2}$$

where q_{gen} is the energy generated per unit volume, k is the thermal conductivity, T is the temperature, τ is the time, and x, y, z are the three coordinate directions of the heat flow. For steady-state and constant thermal conductivity, heat flow in one dimension is given by

$$q_{cond} = - kA\frac{\partial T}{\partial x} \qquad (2.3)$$

where q_{cond} is the heat conduction, A is the cross-sectional area normal to the temperature gradient $\frac{dT}{dx}$.

The third energy loss is by thermal conduction or convection to a surrounding fluid or a gas. At high pressure the gas acts as a solid insulating material and the heat flow is governed by equation 2.2 . In large objects the temperature difference in gases can cause convection driven fluid flow and subsequent heat transfer. However, heat loss through free convection does not take place in small cavities, or for the geometries found in micromachining devices[30]. Heat loss by convection was not observed during any measurements done on the designed microstructures, and as such will not be discussed.

Consider an object, similar to the suspended membranes and microbridges discussed in Chapter 1, which generates internal heat and is thermally isolated from the heat sink except for solid support arms. If the rate of supply of energy is kept constant, and radiation plus support lead heat losses are minimized, the temperature of the heated object depends primarily on the loss of energy due to thermal conductivity of the gas[1]. The amount of heat lost is proportional to the thermal conductivity k of the gas, surface area A of the heated object, the temperature gradient, and is given by

$$q_{gas} = - kA\frac{dT}{dx} \qquad (2.4)$$

The above relationship holds for a wide range of pressures greater than 10 Torr, with thermal conduction loss constant within a few percent. This region from 760 Torr to 10 Torr is known as the viscous, Maxwell or molar region[32]. In this region the mean free path of the molecules, i.e. the average distance that molecules travel in a gas between two successive collisions with other molecules of that gas, is very small compared with the distances within the container of the gas. For air at 27° C the mean free path λ in millimeters is given by

$$\lambda_{mm} = \frac{0.05}{P} \tag{2.5}$$

where P is the pressure in Torr[3]. In the viscous region only the mutual collisions between the molecules dominate, not their individual exchange of heat from the hot to cold surfaces. In this region the flow of the gas can be turbulent or laminar[31]. When the velocity of the gas exceeds certain values the flow is turbulent and the flowing gas layers are not parallel. At lower velocities the flow is laminar and the gas layers are parallel.

At low pressures when the distance from hot to cold object is less than the molecular mean free path, the conduction of heat becomes independent of the geometry and is proportional to the pressure although it has molecular mass dependence. This is known as the Knudsen or molecular region. In this region the flow is molecular, intermolecular collisions are negligible and only the collisions of the gas molecules with the surfaces play a dominant role. This behavior is used in several types of medium-vacuum conventional thermocouple, Pirani and thermistor gauges, and various silicon micromachined vacuum gauges. These gauges have been discussed in Chapter 1. In general, these employ an electrically heated resistor whose temperature is determined by the balance of energy supplied and the heat losses to surrounding walls. These devices fail to measure pressure below 10^{-3} Torr due to saturation of heater temperature, and the heat conduction through support arms and radiation dominate over heat transfer to the gas.

Even at ultra low pressures a large number of molecules are present per unit volume and have a high incidence rate. Figure 2.1 shows values of molecular density, molecular incidence rate and mean free path as a function of pressure. If, instead of measuring heater temperature, transfer of heat from a constant-temperature heater to a temperature-sensitive resistor separated by a gap is measured, this measure should depend on the number of molecules present and hence the pressure.

However, the process of heat transfer by gases from a hot to a cold object is different in the case of the viscous region and in that of molecular region. In the viscous region the group behavior of molecules is responsible for the heat transfer, and the heat transferred between two parallel plates whose temperatures are T_1 and T_2, and distance d apart, is given by

$$q_{vis} = \frac{1}{4}\eta c_v A(9\gamma - 5)(T_1 - T_2)/d \tag{2.6}$$

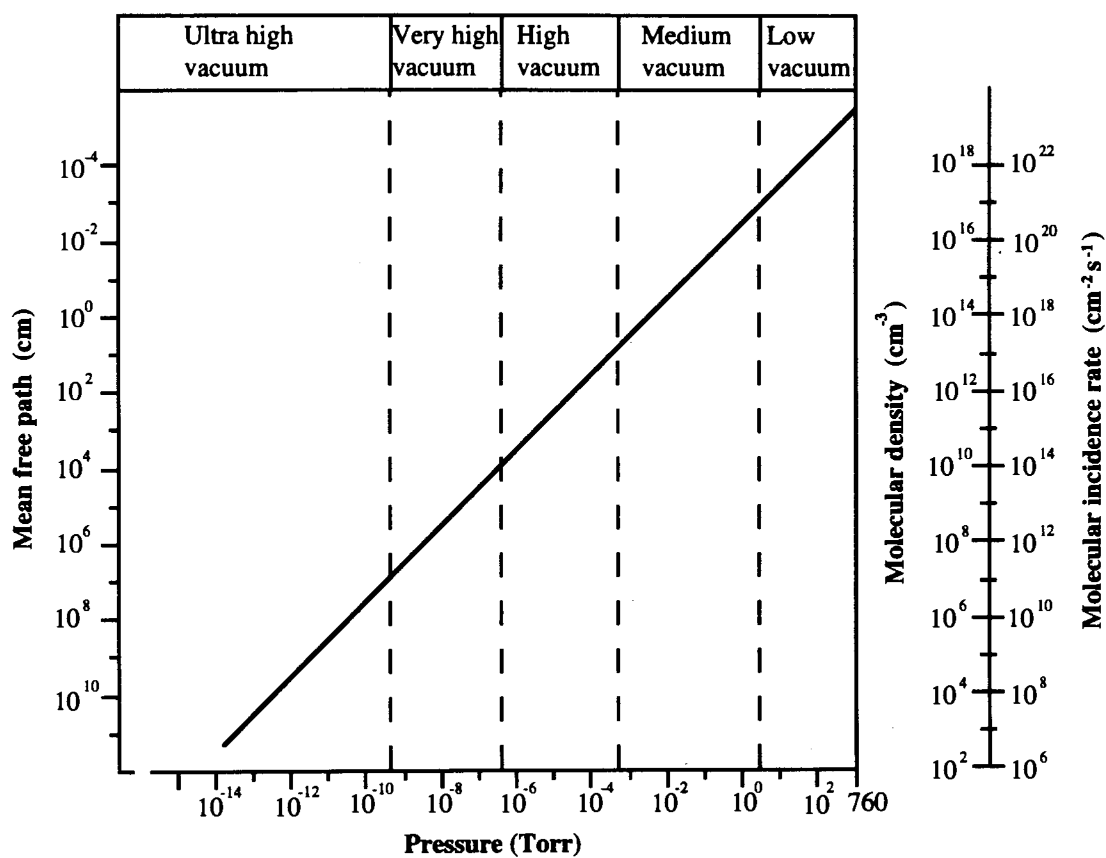

Figure 2.1 - Molecular density, mean free path and molecular incidence rate versus pressure.

where η is the viscosity, c_v is the specific heat at constant volume, A is the area, and γ is the isentropic constant of the gas. The viscosity η is proportional to λ, and the approximate relationship is given by

$$\eta = \frac{1}{3}\rho v_{av} \lambda \qquad (2.7)$$

where ρ is the density of the gas, and v_{av} is the average velocity of the gas molecules. In the viscous region, these parameters vary within only a few percent with pressure and thus cause only a small variation in the heat transfer[1]. In the molecular region individual molecules carry the heat, and the heat transfer is given as

$$E = \Lambda_o \alpha \sqrt{\frac{273}{T_2}} (T_1 - T_2) P \qquad (2.8)$$

where α is the accommodation coefficient and P is the pressure. Λ_o is the free molecular conductivity at 0° C given by

$$\Lambda_o = \frac{1.47 \times 10^{-12}}{M^{1/2}} \left(\frac{\gamma + 1}{\gamma - 1} \right) \qquad (2.9)$$

where M is the molecular mass[1]. The equations 2.8 and 2.9 indicate that the heat flow in the molecular region is directly proportional to the pressure and is inversely proportional to the square root of the molecular mass of the gas specie.

Thus, the transfer of heat by the molecules from a heater resistor to a sense resistor (see Figure 2.2) is dependent on the density of molecules, and is a measure of the pressure in the vacuum chamber. This forms the basis for our designs of a vacuum sensor.

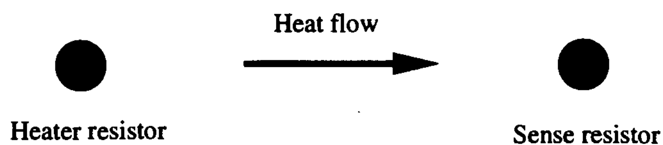

Figure 2.2 - Schematic of proposed measurement of heat flow.

2.2 Design and Fabrication

The proposed measurement of heat flow from a hot object to a cold object to indicate the level of vacuum requires a heater resistor and a temperature-sensitive sense resistor separated by a gap (see Figure 2.2). The temperature-sensitive resistor measures the heat flow from the heater resistor across the gap. This heat flow changes with pressure because the concentration of molecule changes.

The designed vacuum sensors have been fabricated using Canadian Microelectronics Corporation's (CMC) fabrication service which is provided by Northern Telecom's (NT) 3-micron CMOS double layer metal (DLM) process. Special layout design rules were followed which allow the formation of thermally isolated microbridges after a single micromachining step of an anisotropic etching. M. Parameswaran, et al[32,33], describe in detail this procedure, which has been used successfully to fabricate cantilevers, grooves, pits and microbridges. Many sensors, including a thermal pressure sensor[19], a flow sensor[23], a visual-to-thermal converter[34], and a thermal radiation emitter[35] fabricated by using this technique have already been reported in the literature. The use of unconventional design layout rules for the fabrication of micromachining structures does not affect the actual fabrication process, therefore, signal processing circuitry can be realized on the same chip, thus realizing 'smart sensors'. The use of a standard IC technology also offers the benefits of mass production at low cost.

We designed many structures to investigate the feasibility of a vacuum sensor based on the proposed principle and measurement technique. The basis of all structures is a polysilicon[36,37,38] resistor with metal leads embedded in the various oxide layers of the NT's CMOS3 DLM process[39]. Figure 2.3 shows one such structure, termed as 1 plate meander-type polysilicon resistor. Polysilicon has a temperature coefficient of approximately $2 \times 10^{-3}\ ^{\circ}C^{-1}$ (see Chapter 3, Section 3.1), and is used to realize both heater and the sense resistor. C Design Language (CDL) [40] was used to generate layout designs of all the structures. It offered the advantage of generating similar structures of varied sizes easily, once a basic structure program had been written. A sample program for generating one of these structures is attached (see Appendix 1).

The gray areas in Figure 2.3b, which shows top view of the structure, represent the section where the unconventional design layout rules have been followed. This consists of

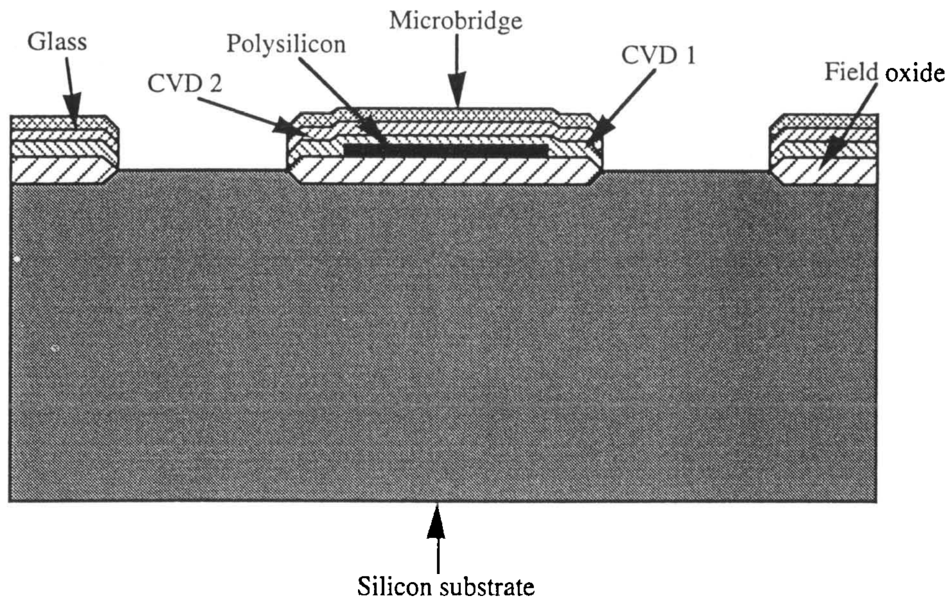

Figure 2.3a - Cross-sectional view of structure 1 plate meander-type polysilicon resistor.

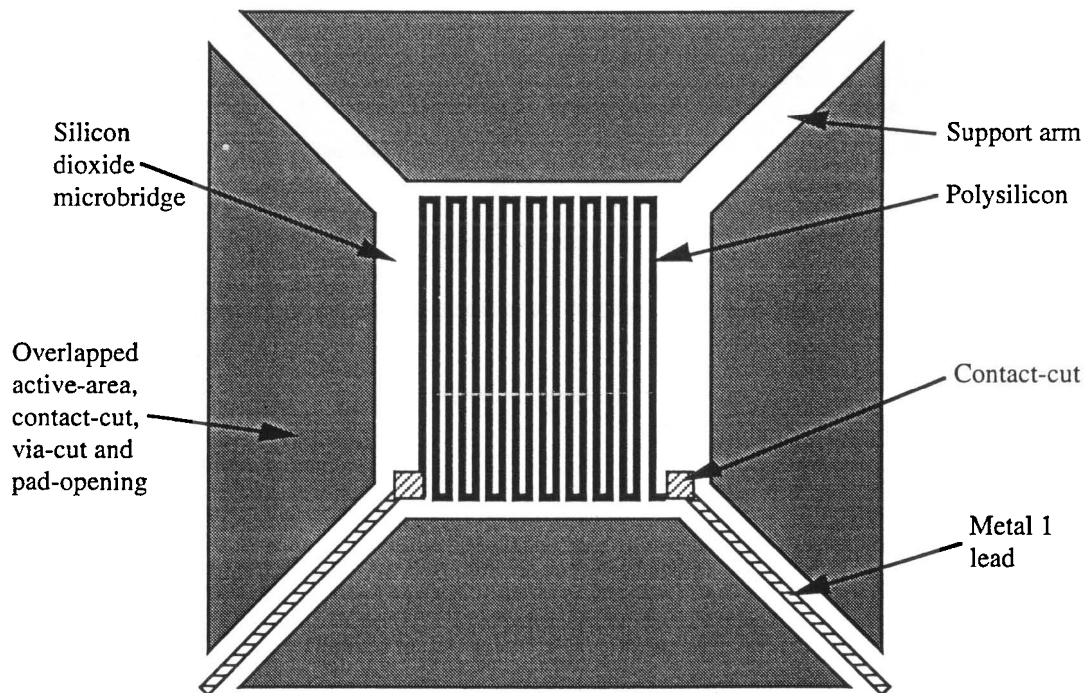

Figure 2.3b - Top view of structure 1 plate meander-type polysilicon heater resistor.

Figure 2.3 - Schematic of structure 1 plate meander-type polysilicon resistor.

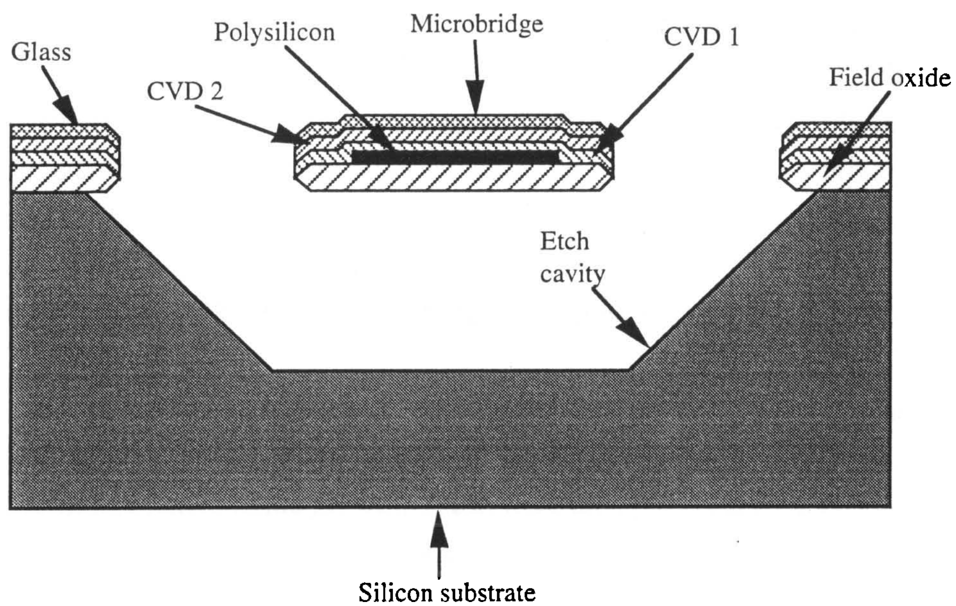

Figure 2.4 - Schematic of cross-sectional view of structure 1 plate meander-type polysilicon resistor after etching.

overlapping the active area, contact-cut, via-cut and pad-opening layers of the CMOS3 layout design procedure. This is not allowed for conventional electrical circuit design and is considered a design rule error. However, this overlapping of the layers results in the exposure of substrate silicon at these openings. These structures were then placed in the standard pad frame designs using KIC, an integrated circuit (IC) layout design software package, and the connecting metal wires were drawn. Appendix 2 shows the schematic layout of the four ICs which contain various structures studied for the feasibility of a vacuum sensor.

The complete chip design files were then sent for fabrication. After the ICs containing these structures were received, they were prepared for the final post processing step of an anisotropic etching using PSE-300 ethylene diamine pyrocatechol and water (EDPW) solution manufactured by Transene Co. Inc.. The EDPW solution selectively etches the <100> and <110> crystal orientation, leaving the <111> orientation relatively unetched as the etch ratio is 50:30:3 respectively for the three planes[41]. This creates sidewalls set at an angle of 54.7° with respect to the surface in <100> silicon, which is also the substrate wafer in NT's CMOS3 DLM fabrication process.

Before the samples were put in the EDPW solution they were dipped in buffered oxide etch (BOE) solution, which is a weak solution of HF acid, for 15 seconds to clean the surface of any native oxide growth. These were then placed in EDPW solution at 95° C for two hours. The temperature has to be kept very stable as EDPW's etching performance is very temperature-sensitive. The etching solution attacks the exposed silicon, cuts under the SiO_2 layers enveloping the polysilicon and metal lines, and forms a cavity in the form of a trench (see Figure 2.4). This results in the formation of a microstructural plate suspended over the cavity by the bridge's SiO_2 arms and the metal leads. The suspension provides thermal isolation from the substrate, and the plate can now attain a high temperature at low excitation powers. The ICs containing the etched structures were epoxy bonded to the 24 pin DIP and the chip to package interconnections were made with 25 μm gold wire bonds.

The intent of this design was to realize a structure, similar to two parallel plates separated by a small gap, in which the heat transfer can be measured from one plate, which is kept at high temperature, to the other unheated plate. The first approach consisted of an arrangement of two ICs, IC3SFCP1 and IC3SFCP2, each having a structure, termed as 1 plate meander-type poly resistor, with meander-type polysilicon resistor on a SiO_2 microbridge (see Figure 2.5a). There is another similar structure on the ICs but with a

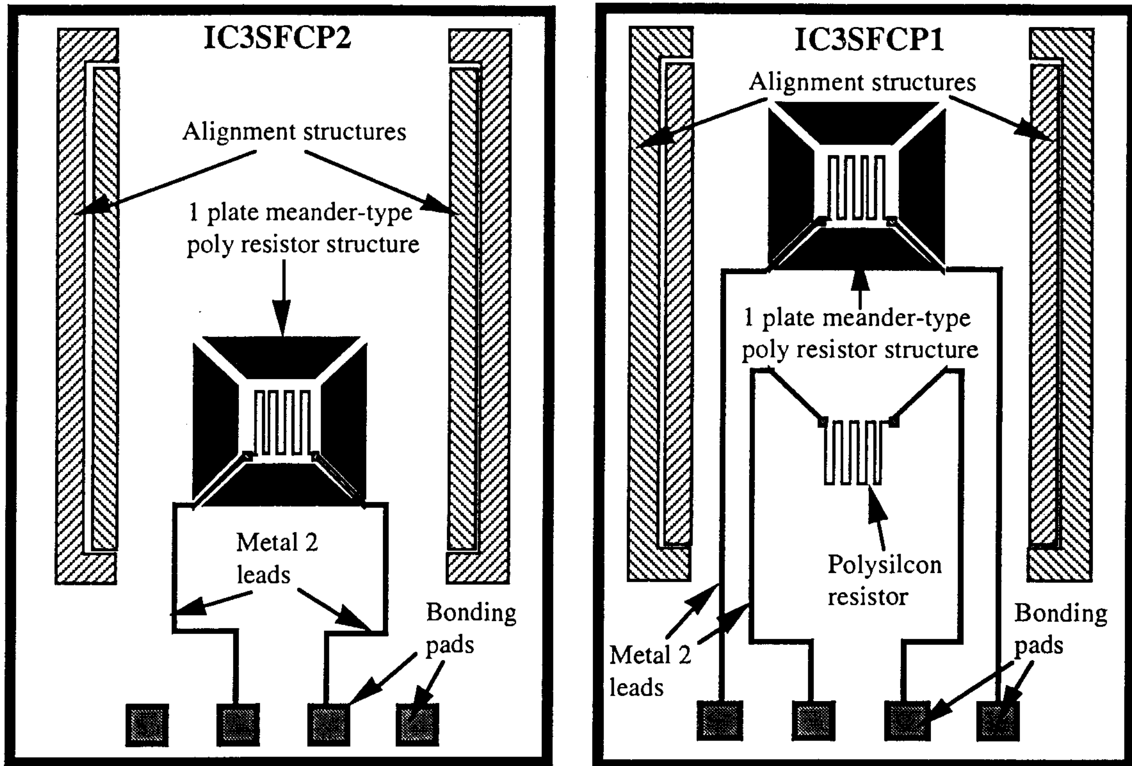

Figure 2.5a - The alignment structures and 1 plate meander-type polysilicon resistor structure on each of designed IC3SFCP1 and IC3SFCP2 integrated circuit chips.

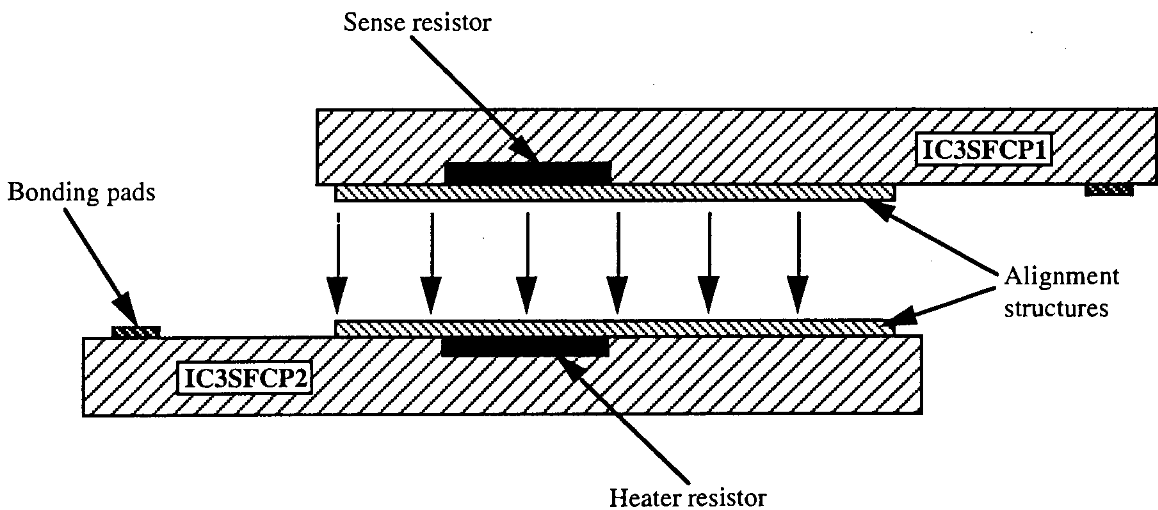

Figure 2.5b - Proposed placement and bonding of ICs IC3SFCP1 and IC3SFCP2.

Figure 2.5 - Schematic of proposed placement of the designed ICs IC3SFCP1 and IC3SFCP2.

Structures	Cavity	Heater-side (All dimensions in microns)				Sense-side (All dimensions in microns)			
		Heater microbridge	Support arms	Poly line	Metal line	Sensor microbridge	Support arms	Poly line	Metal line
1 plate beam-type poly resistor structure	456 x 117	355 x 42	68 x 15	334 x 4	71 x 3	N/A	N/A	334 x 4	71 x 3
1 plate meander-type poly resistor structure	240 x 240	120 x 120	91 x 12	1626 x 4	90 x 3	N/A	N/A	1626 x 4	90 x 3
1 plate meander-type long poly resistor structure	360 x 240	240 x 120	91 x 12	3488 x 4	90 x 3	N/A	N/A	3488 x 4	90 x 3
2 plate meander-type poly resistor structure	300 x 300	132 x 132	123 x 12	1735 x 4	127 x 3	112 x 22	96 x 14	92 x 4	98 x 3
3 plate beam-type poly resistor structure	888 x 188	703 x 20	119 x 12	691 x 4	127 x 3	698 x 22	92 x 14	680 x 4	98 x 3
3 plate meander-type poly resistor structure	300 x 300	132 x 132	123 x 12	1744 x 4	127 x 3	112 x 112	96 x 14	92 x 4	98 x 3

Table 2.1 - Dimensions of various micromachined structures designed. (All dimensions are in microns)

longer meander-type polysilicon resistor. The dimensions of the various structures are listed in Table 2.1 . The ICs also have alignment structures so that when IC3SFCP1 is placed on the IC3SFCP2, the meander-type polysilicon resistor microbridges on the two ICs face each other across a small gap (see Figure 2.5b). The additional polysilicon resistor on IC3SFCP1 is the reference resistor, of same dimension and shape, required if Wheatstone-bridge measurement techniques were to be employed. Once aligned and bonded, the IC3SFCP2 polysilicon resistor is excited as a heater and the IC3SFCP1 polysilicon resistor is used as a sensor. Unfortunately, this arrangement did not work because of the complexity involved in the bonding, alignment and wire connections.

The failure of the above technique of coupling the sensor and heater resistor placed on two separate ICs led to the approach of integrating the heater and sense resistor in a single structure on one chip. The chip, IC3SFCP3, contains such structures which have a meander-type polysilicon resistor as a heater and a small beam-type polysilicon resistor on the side as a sensor (see Figure 2.6a and 2.6b). This structure is referred to as 2 plate meander-type poly resistor structure. The gap between the central and the side microbridge is designed to be 6 μm, and is the smallest opening in the silicon substrate allowed by the special layout design rules for fabrication of microstructures using NT's CMOS3 DLM process. Constraints were also placed by the opening requirements in the silicon substrate for a successful EDPW etch. The aim was to have the smallest gap possible so as to achieve the mean free path criteria at a pressure as high as possible. This implies that the mean free path of the gas molecules equals the microbridge separation at about 10 Torr (from equation 2.5). After the EDPW etching, when the bridges are isolated from the substrate, the side microbridge bends upwards due to the stress in its support arms (see Figure 2.7). This formation of two microbridges separated by a small gap, and thermally isolated over a cavity, was the first structure of its kind in the micromachining field, and formed the basis for further designs of a vacuum sensor. The other structures of the IC3SFCP3 are to investigate the isolation and uniformity of thermal distribution for various suspended plate structures.

The complexity in the design due to the meander-type polysilicon resistor did not allow analytical thermal modeling of the device. To investigate the thermal flow, and allow ease of modeling, several structures with straight beam-type polysilicon heater resistor, instead of the meander-type, were designed. The chip, IC3SFCP4 contains many such structures. Figure 2.8a, 2.8b, and 2.9 show the lateral, top view and SEM photograph respectively of one such structure, referred to as 1 plate beam-type poly resistor structure.

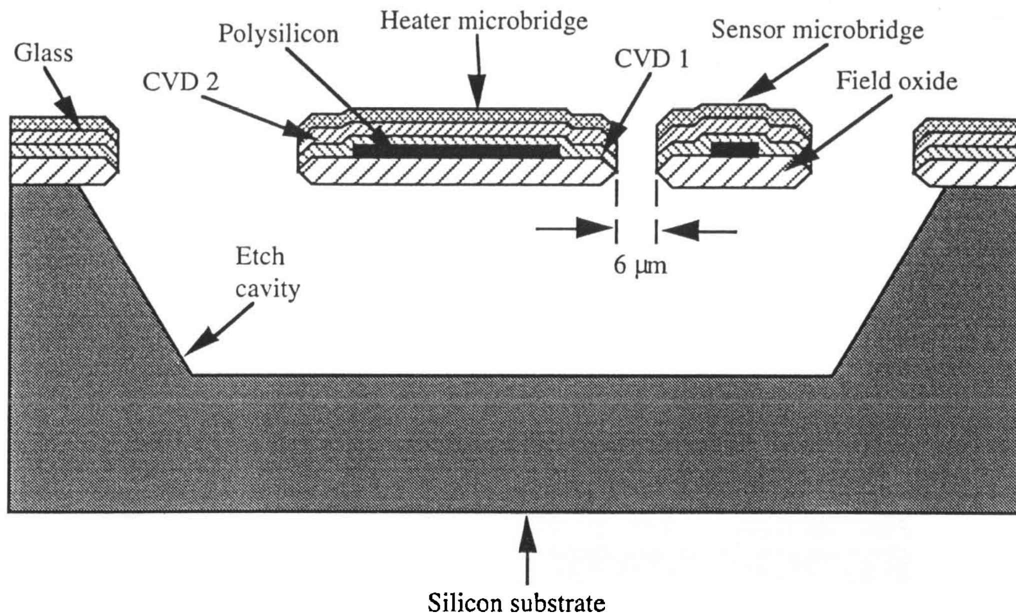

Figure 2.6a - Cross-sectional view.

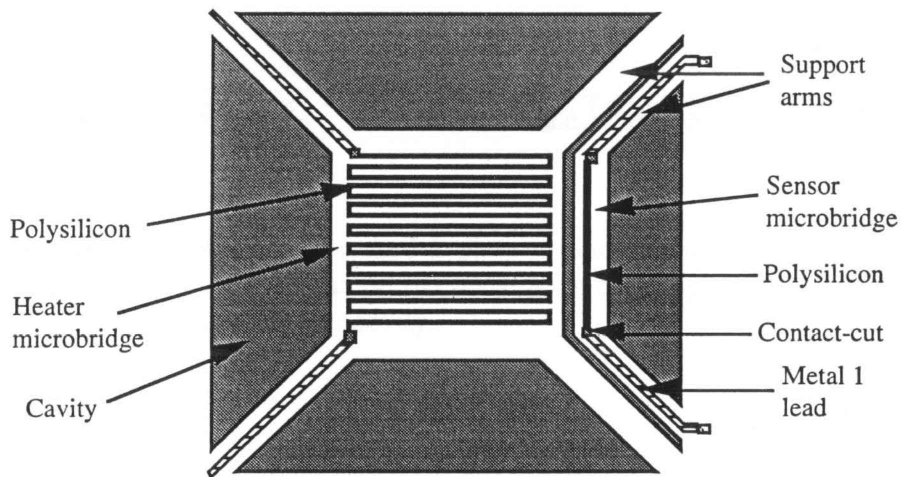

Figure 2.6b - Top view.

Figure 2.6 - Schematic of structure 2 plate meander-type polysilicon resistor.

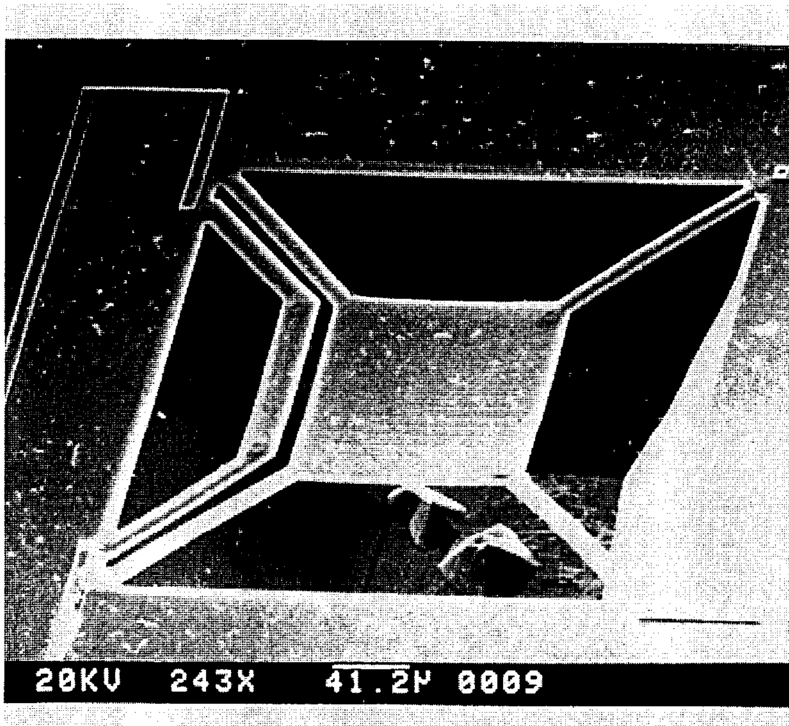

Figure 2.7 - SEM photograph of etched 2 plate meander-type polysilicon resistor structure. Noticeable is bending of the sense resistor microbridge, and trench cavity with some impurity at the bottom of the cavity.

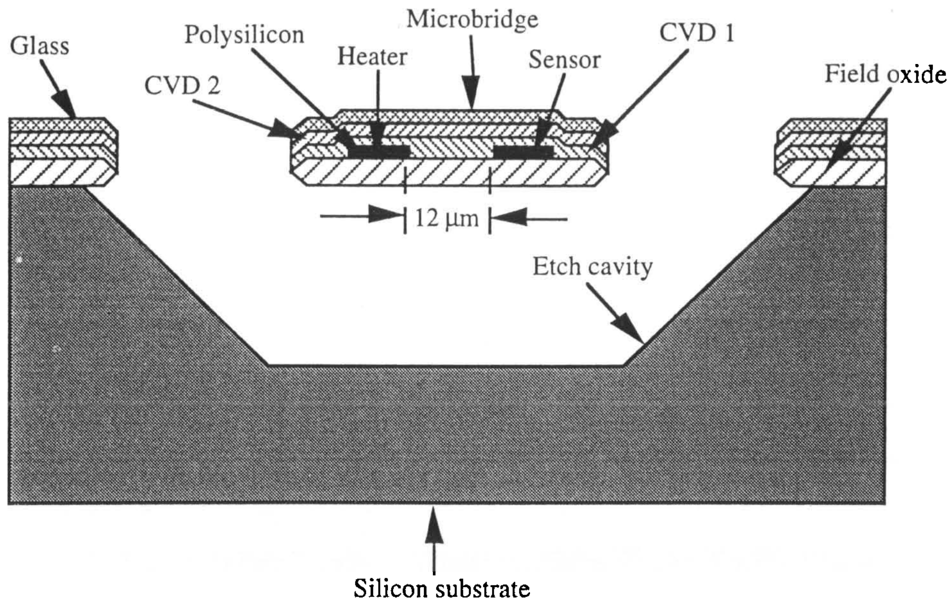

Figure 2.8a - Cross-sectional view.

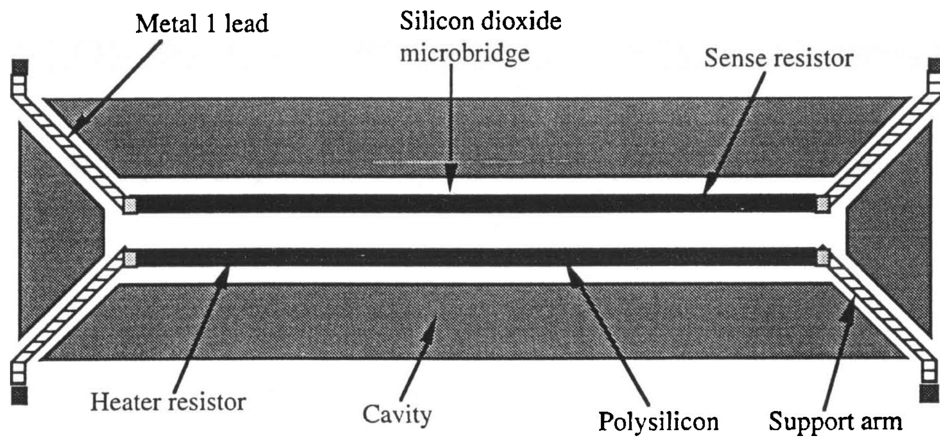

Figure 2.8b - Top view.

Figure 2.8 - Schematic of structure 1 plate beam-type polysilicon resistor.

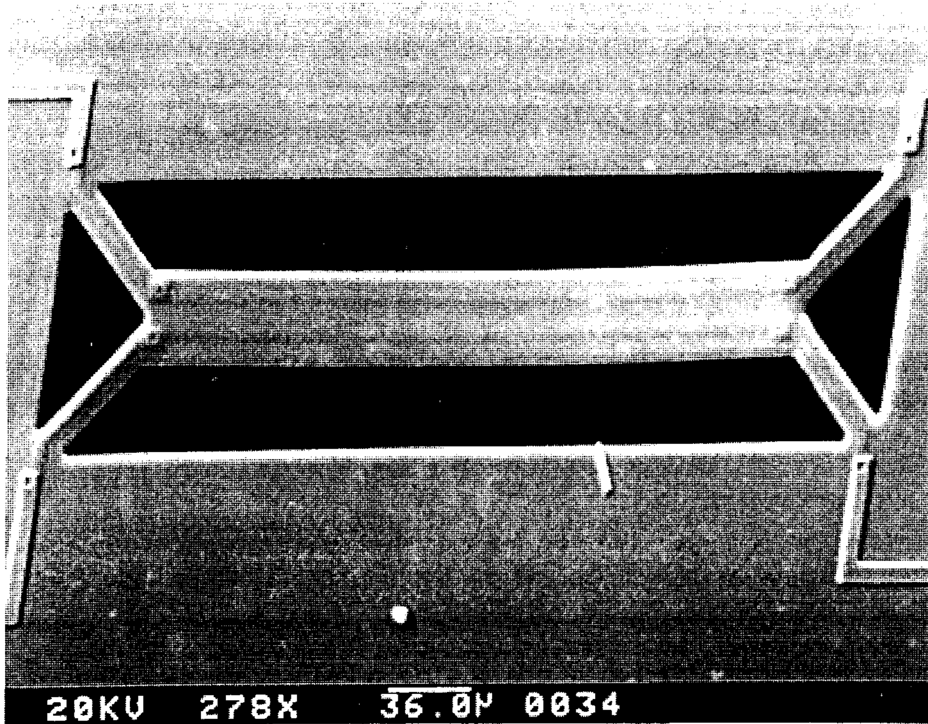

Figure 2.9 - SEM photograph of etched 1 plate beam-type polysilicon resistor structure.

In this structure much of the heat flow from a beam-type polysilicon heater resistor to another beam-type polysilicon sense resistor is through the SiO_2 layers. It simplifies the analytical analysis, and eliminates the uncertainty of the heat flow across a gap of air as experienced with the previous structures.

Figures 2.10a and 2.10b show lateral and top view of another structure of the IC3SFCP4 which has three microbridges separated from each other by a gap of 6 µm. Each microbridge has a long beam-type polysilicon resistor. The central microbridge polysilicon resistor is activated as a heater and the polysilicon resistor on either of the side microbridges can be used as a sensor. This is the structure investigated in detail for feasibility as a vacuum sensor and is referred to as 3 plate beam-type poly resistor structure. Only two microbridges are required for operation of the structure as a vacuum sensor, and so the additional side microbridge provides redundancy. Figure 2.11 shows the SEM photograph of the structure. The chip IC3SFCP4 also has other three plate structures, with meander-type heater resistor and beam-type sense resistors on two sides (see Figure 2.12), for response comparisons.

2.3 Measurement Technique's Requirement

Consider the energy transfer from the central heater resistor of the structure 3 plate beam-type poly resistor at a temperature of 100° C to the sense microbridge at 22° C by air at 10^{-2} Torr[1]. The heat flow will be governed by the molecular region equations 2.8 and 2.9 .

For air, $\gamma = 7/5$, diatomic gases and $M = 28.98$,

$$\Lambda_0 = \frac{1.47 \times 10^{-2}}{\sqrt{28.98}} \left(\frac{2.4}{0.4}\right) = 1.64 \times 10^{-2} \text{ Watts/cm}^2\ {}^\circ\text{C Torr} \qquad (2.10)$$

Thus, for $\alpha = 0.8$, the heat conduction per unit area given by the equation 2.8 is equal to

$$\begin{aligned} E &= 0.8 \times 1.64 \times 10^{-2} \sqrt{\frac{273}{295}} (373 - 295) \times 10^{-2} \\ &\approx 10^{-2} \text{ Watts/cm}^2 \end{aligned} \qquad (2.11)$$

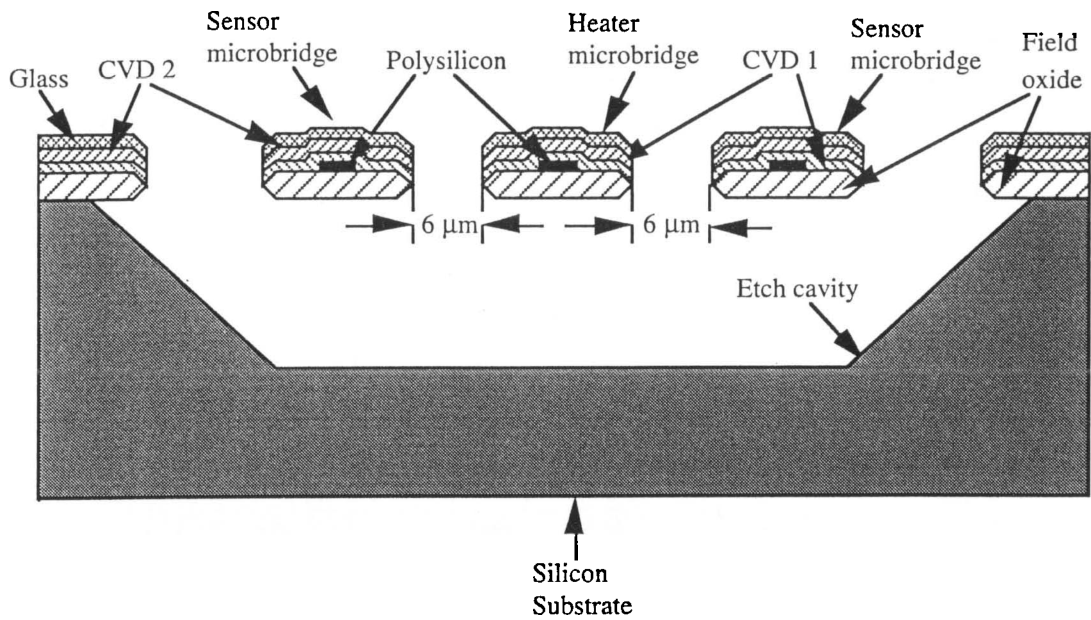

Figure 2.10a - Cross-sectional view.

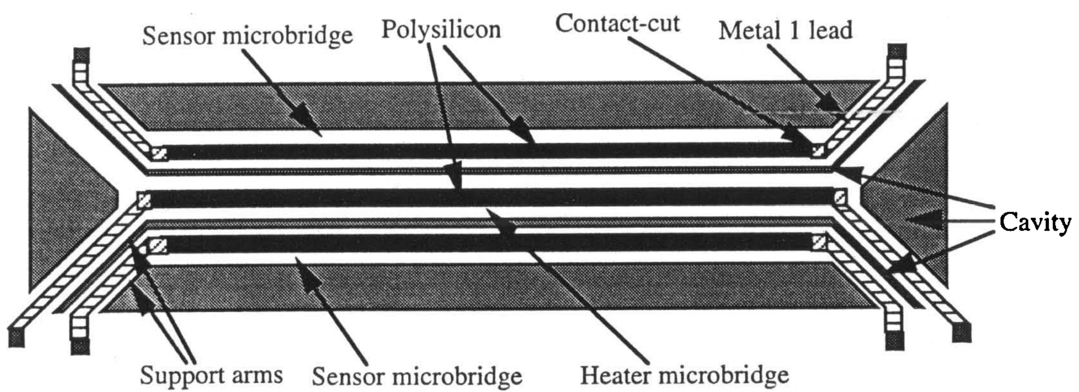

Figure 2.10b - Top view.

Figure 2.10 - Schematic of structure 3 plate beam-type polysilicon resistor.

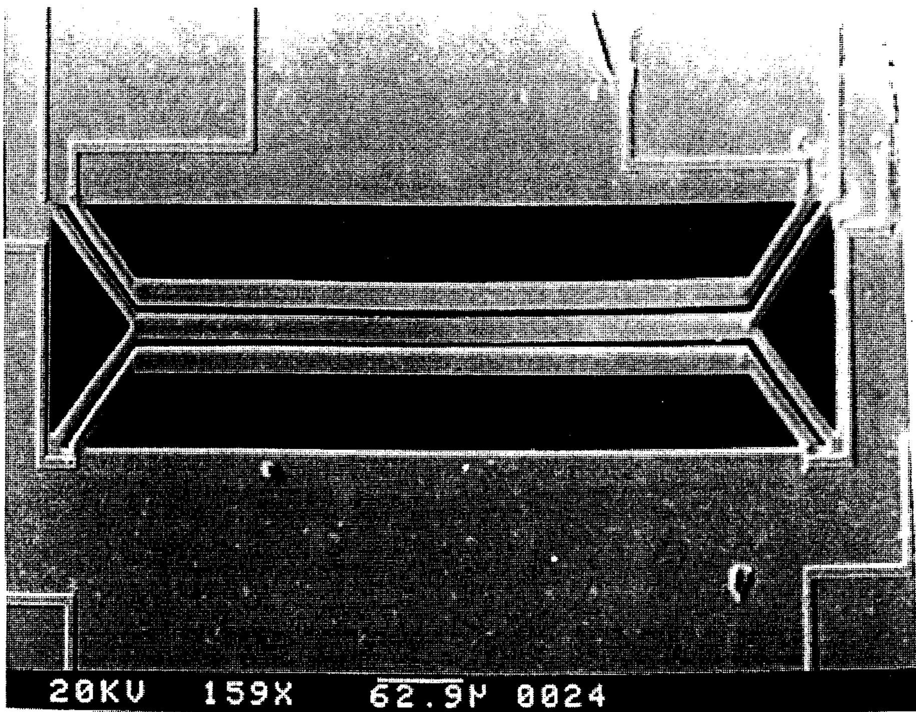

Figure 2.11 - SEM photograph of etched 3 plate beam-type polysilicon resistor structure.

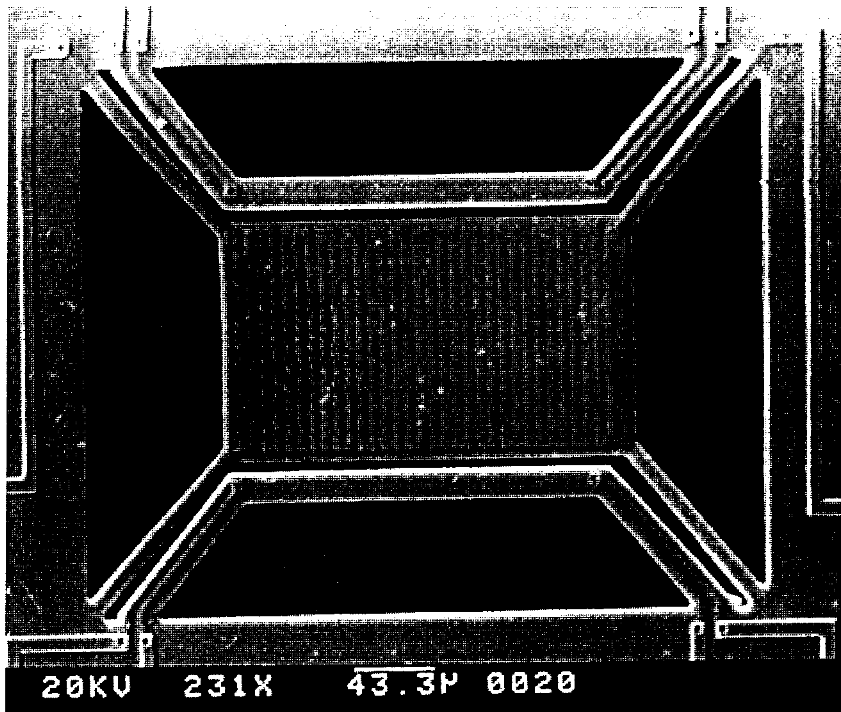

Figure 2.12 - SEM photograph of etched 3 plate meander-type polysilicon resistor structure.

The facing cross-sectional area for sensor microbridge of approximate length 700 μm and width 4 μm is about 3×10^{-5} cm^2. Thus, the total heat transfer is approximately equal to

$$E = 3 \times 10^{-5} \times 10^{-2} = 3 \times 10^{-7} \text{ Watts} \tag{2.12}$$

At the sensor end, this heat transfer will cause a rise in the temperature of the microbridge and hence the polysilicon sense resistor. The heat from the sensor microbridge is conducted mainly through the two aluminum leads of the resistor. For the aluminum leads, the cross-sectional area A is 3.5×10^{-8} cm^2, the length L is 10^{-2} cm, the thermal conductivity k is 2.36 W/cm °C[7], and the temperature rise can be approximately calculated using the equation 2.3 as

$$T_2 = 22 + \frac{3 \times 10^{-7} \times 10^{-2}}{2 \times 2.36 \times 3.5 \times 10^{-8}} = 22.018 \text{ °C} \tag{2.13}$$

Thus the sense resistor notes a temperature rise of about 1.8×10^{-2} °C. This implies a resistance change of approximately 2.2×10^{-5} Ω since temperature coefficient of resistivity of polysilicon is approximately equal to 2×10^{-3} °C^{-1} . The sense resistor of the structure 3 plate beam-type poly resistor is about 3 KΩ which means that the resistance change is of the order of 10^{-6} percent. Conventional methods including Wheatstone-bridge are incapable of measuring such small changes. This requires a technique which is capable of measuring very small resistance changes. AC phase-sensitive detection technique is capable of measuring very weak signals even in the presence of a much larger noise source and is being applied widely in many fields, but has not been reported for applications in microsensors. The small time constant of these micromachined structures (see Chapter 3, section 3.4) allows the use of time-varying signals, and thus it is possible to use phase-sensitive detection technique for the measurement of the heat flow.

2.4 Phase-Sensitive Detection

The phase-sensitive detection technique is designed to respond specifically to a time-varying information bearing signal having the same frequency as the fundamental excitation frequency, or bear a harmonic relation to it. These systems are also known as 'lock-ins', because they are phase locked to the signal of interest by a synchronous

reference voltage[42]. The detection with respect to the synchronous reference enables the use of long averaging time thus improving the signal-to-noise ratio.

The operation of a lock-in can be explained with the help of Figure 2.13a which shows the block diagram of major components of a single-phase lock-in amplifier. The input signal s(t) passes through a low-noise differential amplifier to a set of filters. The purpose of the filtering at this stage is to eliminate noise from known or suspected sources. It usually consists of two notch filters of 60 Hz and 120 Hz, to suppress the first and second harmonic of power-line noise, and a tracking band pass filter. The conditioned signal then passes through a high-gain amplifier to boost the gain and provide a noise-match to the signal sources, and then the signal enters one of the inputs of the demodulator.

Meanwhile, a reference signal r(t) enters the reference signal channel, where it passes through a Phase-locked loop (PLL) and a phase detector to provide a stable reference signal. This signal is fed to the other input of the demodulator. The demodulator output can be expressed as following,

The input time-varying signal s(t) can be written as

$$s(t) = V_s \cos(2\pi f_s t + \phi_s) \tag{2.14}$$

where V_s is the amplitude, f_s is the frequency, t is the time, and ϕ_s is the phase of the input signal.

The reference time-varying signal r(t) can be written as

$$r(t) = V_r \cos(2\pi f_r t + \phi_r) \tag{2.15}$$

where V_r is the amplitude, f_r is the frequency, t is the time, and ϕ_r is the phase of the reference signal. The output v_p of the demodulator is given as

$$\begin{aligned} v_p(t) = {} & \frac{1}{2} V_s V_r \cos[2\pi(f_s + f_r)t + \phi_s + \phi_r] \\ & + \frac{1}{2} V_s V_r \cos[2\pi(f_s - f_r)t + \phi_s - \phi_r] \end{aligned} \tag{2.16}$$

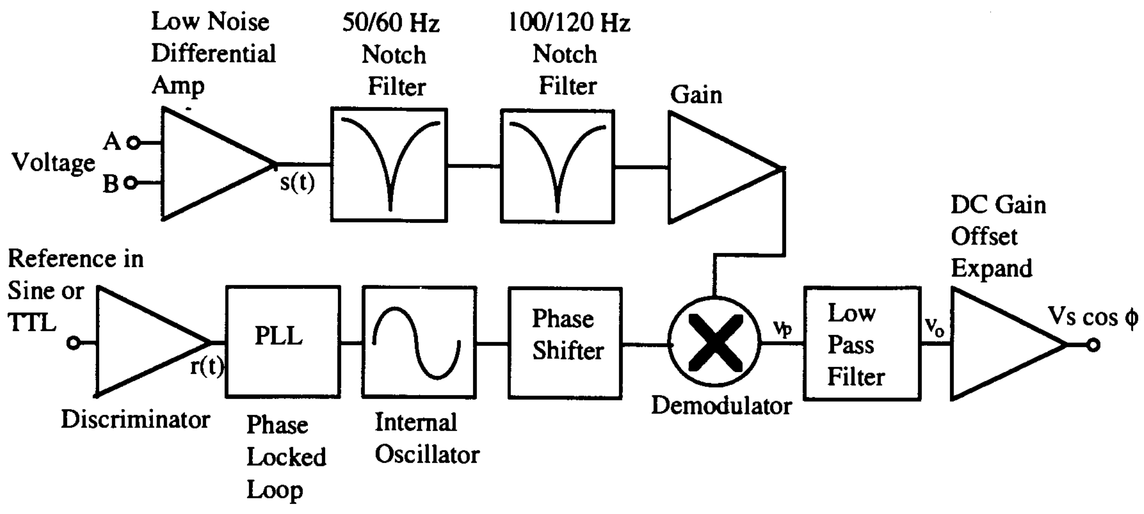

Figure 2.13a - Single-phase lock-in amplifier.

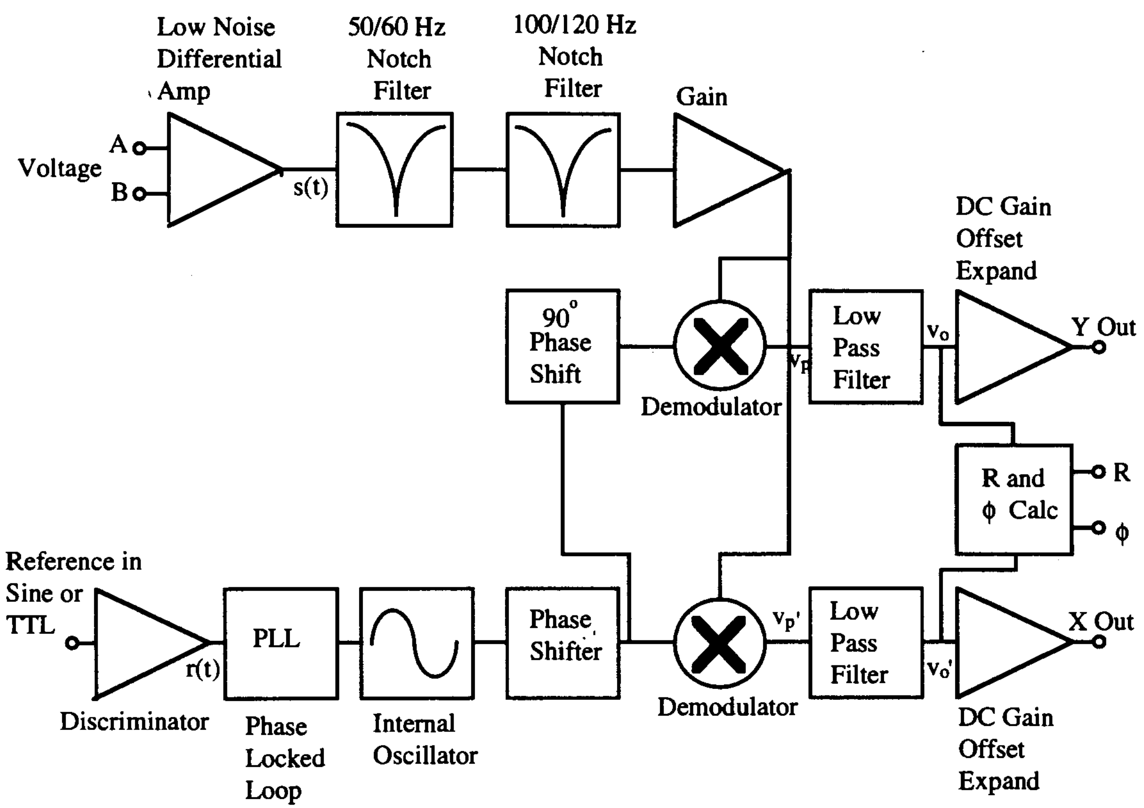

Figure 2.13b - Dual-phase lock-in amplifier.

Figure 2.13 - Block diagram of major components of a lock-in amplifier.

The higher frequency components are removed after the signal is passed through a low-pass filter. If s(t) and r(t) have the same frequency, then the output at the low pass filter is a DC signal given by

$$v_o = k_r V_s \cos\phi \qquad (2.17)$$

where $\phi = (\phi_s - \phi_r)$, and k_r is a constant scaling factor. By adjusting ϕ_r, ϕ can be made equal to zero, in which case one can measure V_s ($\cos\phi = 1$). Conversely, if ϕ is 90°, there will be no output at all. The signal then passes through a high-gain DC amplifier to the output. A lock-in with a single demodulator is called a single-phase lock-in and its output is $V_s \cos\phi$. The phase dependency of the output is eliminated by adding a second demodulator (see Figure 2.13b [43]). The second demodulator multiplies the input signal with the reference signal shifted by 90°, i.e. $V_r \cos[\omega_r t + \phi_r + 90°]$, and its low pass filtered output is given by

$$v_o'(t) = \frac{1}{2} V_s V_r \sin[2\pi(f_s - f_r)t + \phi_s - \phi_r] \qquad (2.18)$$

or,

$$v_o' = k_r V_s \sin\phi \qquad (2.19)$$

for $f_s = f_r$ and $\phi = (\phi_s - \phi_r)$.

Now there are two outputs, one proportional to $\cos\phi$ and the other proportional to $\sin\phi$. If the two output is called X and Y respectively, then

$$X = V_s \cos\phi \qquad (2.20)$$

and,

$$Y = V_s \sin\phi \qquad (2.21)$$

These two quantities represent the signal as a vector relative to the lock-in reference signal. X is called the 'in-phase' component and Y is called the 'quadrature' component. This is because when $\phi = 0$, X measures the signal while Y is zero.

By computing the magnitude R of the signal vector, the phase dependency is removed as

$$R = \left(X^2 + Y^2\right)^{1/2} = V_s \tag{2.22}$$

Thus, R measures the signal amplitude and does not depend upon the phase between the input signal and the reference signal.

Most of the lock-in amplifiers now in the market use microprocessors for digital operation of the front panel display and controls. However, the signal and reference paths remain entirely analog. The newest generation of lock-ins employs digital signal processing using DSP chips and A/D converters. The conventional lock-in signal processing tasks such as filtering, amplification, multiplication, phase-locked loop, phase shifter, reference signal generation, control and display are done by the DSP chip after the conversion of the analog input signal to digital signal using the A/D converters. R. Baylor, et al[44], describe this type of lock-in and reports 100 - 120 dB of real dynamic range without gain errors, output drift, noise penalties and pre-filtering.

Phase-sensitive detection is the chosen measurement technique because of its ability to detect very weak AC shifts. This means that even minute changes in the heat flow caused by a small pressure change can be detected, and therefore high sensitivity can be achieved. The next chapter discusses the application of phase-sensitive detection to the microstructures, and the various experiments performed to investigate the operation of the designed microstructure as a vacuum sensor.

3 Experiments and Results

This chapter discusses the experimental set up for the application of phase-sensitive detection technique as applied to microstructures. The response of various structures to this measurement technique is reported. Also, the investigation of a specific microstructure as a vacuum sensor, in constant voltage and constant temperature excitation mode, and response in nitrogen and argon gases is presented.

3.1 Temperature Coefficient of Resistivity

It is necessary first to report the findings of the temperature coefficient of resistivity (TCR) of polysilicon, which constitutes the heater and sense resistors in the designed microstructures, as the TCR value is dependent on the batch and fabrication process. TCR of polysilicon is used to translate the change of resistance of the heater and the sense resistor to their average temperature change. TCR of a material is defined as the increase in resistance per unit resistance per degree rise in temperature of the material and is given as,

$$\alpha = \frac{\Delta R / R}{\Delta T} \tag{3.1}$$

where α is the temperature coefficient of resistance, ΔR is the change in the resistance, R is the nominal resistance, and ΔT is the change in temperature. The unit of temperature coefficient of resistance is per degree Celsius.

TCR of polysilicon was determined by placing a number of structures having polysilicon resistors, both unetched and etched, in a Isotemp Uniform Temperature Oven.

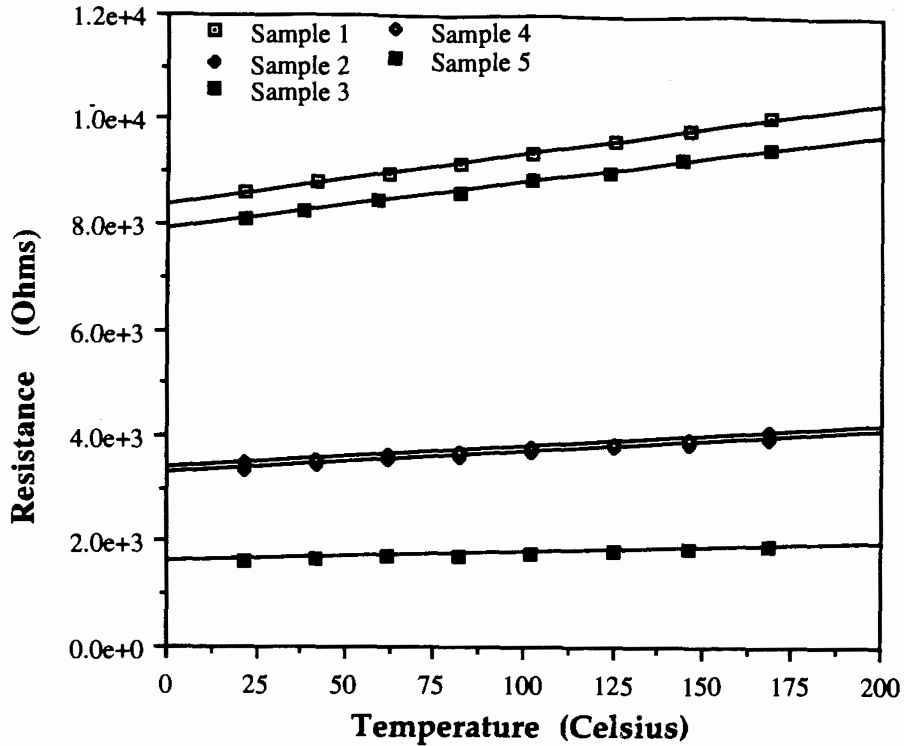

Figure 3.1a - Change in resistance of unetched polysilicon resistors with temperature.

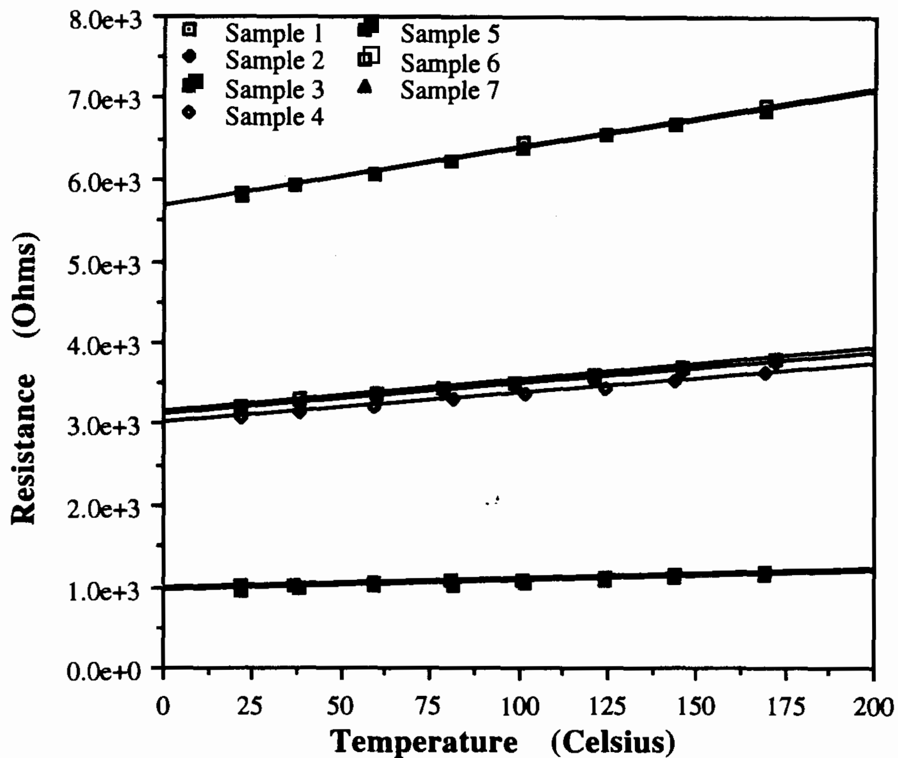

Figure 3.1b - Change in resistance of etched polysilicon resistors with temperature.

Figure 3.1 - Change in resistance of polysilicon with temperature.

The nominal resistance of various sample polysilicon resistors at room temperature varied from approximately 1 KΩ to 8 KΩ. The oven employs a thermocouple to monitor the temperature which is indicated on a digital display. The temperature of the oven was varied from 22° C to 170° C and the resistance of the polysilicon resistors was measured at various intermediate temperatures. A 0.1 mA current was injected in the resistors using a current source and the voltage across the resistors measured to give the value of the resistance. Figures 3.1a and 3.1b show the variation of the resistance of the polysilicon resistors with temperature for the unetched and etched structures respectively. A least-squares straight line fit was done to each set of data. The average temperature coefficient of resistance for the unetched polysilicon resistors was calculated as $1.175 \times 10^{-3} \pm 0.016 \times 10^{-3}$ °C^{-1} for the temperature range 22° C to 170° C, which is very close to 1.2×10^{-3} °C^{-1} reported by E. Obermeier, et al[46]. However, for etched structures the TCR of polysilicon has been found to be $1.247 \times 10^{-3} \pm 0.017 \times 10^{-3}$ °C^{-1} for the temperature range 22° C to 170° C, which is slightly higher than the TCR of unetched structures. The difference in the TCRs of etched and unetched polysilicon is $0.065 \times 10^{-3} \pm 0.023 \times 10^{-3}$ °C^{-1}, which is a difference of 3 standard deviations. Hence, the TCRs show a difference with a statistical confidence of more than 99% [47]. Also, the measurements on the samples were taken in several batches, with three samples in a batch. There was no statistically significant difference between the TCRs of same sample-type (unetched or etched) measured in different batches. Hence, the TCR values of unetched and etched polysilicon are statistically different. Since all the following investigations were done on the etched structures, the TCR of etched polysilicon is used in all the calculations.

3.2 AC Measurement on Microstructures

For the AC measurement on the designed microstructures, square-wave pulses were applied from zero to a peak current to generate on-off heat pulses to the heater polysilicon resistor. The rise and fall in the temperature of the heater resistor is transmitted through the surrounding medium and causes a corresponding temperature variation in the sense resistor. This temperature variation generates a resistive change in the sense resistor due to its temperature coefficient of resistivity which results in AC variations in an applied sensing signal. These AC shifts were measured as a voltage across a 1 KΩ resistor using an oscilloscope in the higher amplitude region of 2 mV and more. A lock-in amplifier was employed to measure the weak AC shifts of less than 2 mV.

The basic circuit for all the AC measurements on the designed microstructure is as shown in Figure 3.2 . On the heater side, V_{pulse} is a square-wave pulse generator, R_h is the heater resistor of the microstructure, R_{hs} is a 1 KΩ load resistor employed to measure the current in the heater circuit and R_d is a decade resistance box employed to load the circuit to regulate currents of very low-amplitudes in the circuit. On the sensor side, V_{dc} is a DC voltage source, R_1 and R_2 form the voltage divider, R_s is the sensor resistor of the microstructure and R_{ss} is a 1 KΩ load resistor to measure the current in the sense resistor.

A Wavetek 178 Programmable Waveform Synthesizer was used to generate the square-wave pulses to drive the heater. It can drive a 50 Ω load from 1 mV to a full 20 Volts peak to peak, and the amplitude can be entered through numeric key pads up to 3 digits of accuracy. The model can generate square-wave signal of frequency 1 mHz to 50 MHz.

A Tektronix 2232 storage oscilloscope was used to measure the AC shifts for signal stronger than 2 mV. It was also employed to store and download various waveforms as ASCII data.

A Stanford Research Systems SR850 DSP lock-in amplifier was employed for the phase-sensitive detection. It is a dual-phase equipment that uses digital signal processing to replace the demodulator, low-pass filter and DC gain circuits found in conventional lock-in amplifiers. The equipment has a CRT to display data and provides a menu based interface. The voltage signal input can be single-ended or differential, and full-scale sensitivity ranges from 10 nV to 1 V. It has 4 auxiliary BNC digital to analog outputs and 4 auxiliary analog to digital inputs. The internal data sample rate ranges from 512 Hz to 1 point every 16 second. In total, 64 K data points may be stored, and displayed in strip chart mode. It also has the capability to calculate mean and standard deviation of trace regions. The heater voltage and current are measured using the auxiliary inputs of the SR850 lock-in amplifier. A constant DC voltage from one of the auxiliary outputs is applied to the sensor side voltage divider bridge to drive a sense signal through the sense resistor.

The output voltage of the lock-in amplifier was stored at a sample rate of 256 Hz, and the statistical deviation of the output was obtained for a minimum time period of 20 seconds, i.e. over 5120 data points.

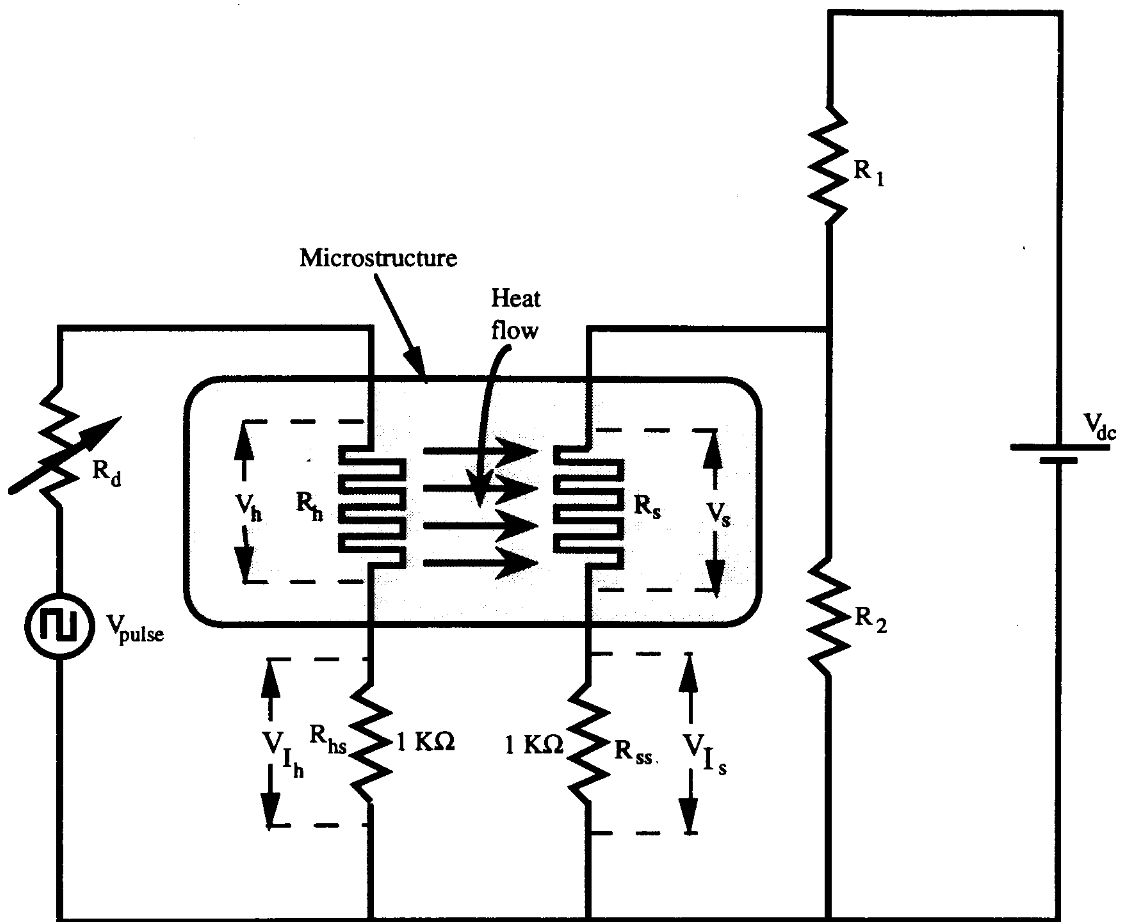

Figure 3.2 - Circuit set-up for measuring the output voltage, and induced heat transfer from the heater resistor to the sense resistor.

3.3 The Vacuum System

The vacuum system consists of a stainless steel chamber, pumps necessary to evacuate the chamber, and valves to control the evacuation procedure (see Figure 3.3). A mechanical pump is used to rough out the chamber to less than 100 mTorr and a diffusion pump is used to reduce the pressure to the low 10^{-6} Torr pressure region. The mechanical pump also serves the second purpose of removing the gases that the diffusion pump has pumped (commonly referred to as "backing the diffusion pump"). A liquid nitrogen cold trap freezes out water vapour from the chamber at a very high rate, and prevents any oil vapour from the mechanical pump and/or the diffusion pump from entering the chamber. The vacuum system is a part of the sputter coater system by Corona Vacuum Coaters[48].

A Series 275 Mini-Convectron vacuum gauge[49] by Granville-Phillips Inc. is used to measure the chamber pressure from 760 Torr to 50 mTorr. This pressure transducer is a convection enhanced Pirani gauge. It is calibrated for nitrogen but also measures the pressure of air correctly within the accuracy of the instrument. Calibration curves are provided for conversion of the analog output voltage for true pressure indication for various gases such as Ar, CO_2, He and O_2. For pressure measurements below 10^{-3} Torr, a Bayard Alpert type Ionization gauge with Varian ratiomatic gauge control is used[50]. The gauge is calibrated for nitrogen, and gas-sensitivity tables are provided to convert the readings from the ionization gauge control for true pressure readings when used with other gases.

The sample structures to be investigated in the vacuum environment were placed in the stainless steel vacuum chamber, and the connections were drawn out through the feedthroughs. The vacuum chamber was then pumped down and stabilized at various pressures by closing the control valves which isolated the evacuation pumps, and controlling the gas flow through the mass flow controllers. The measurements were taken once the desired pressure was achieved.

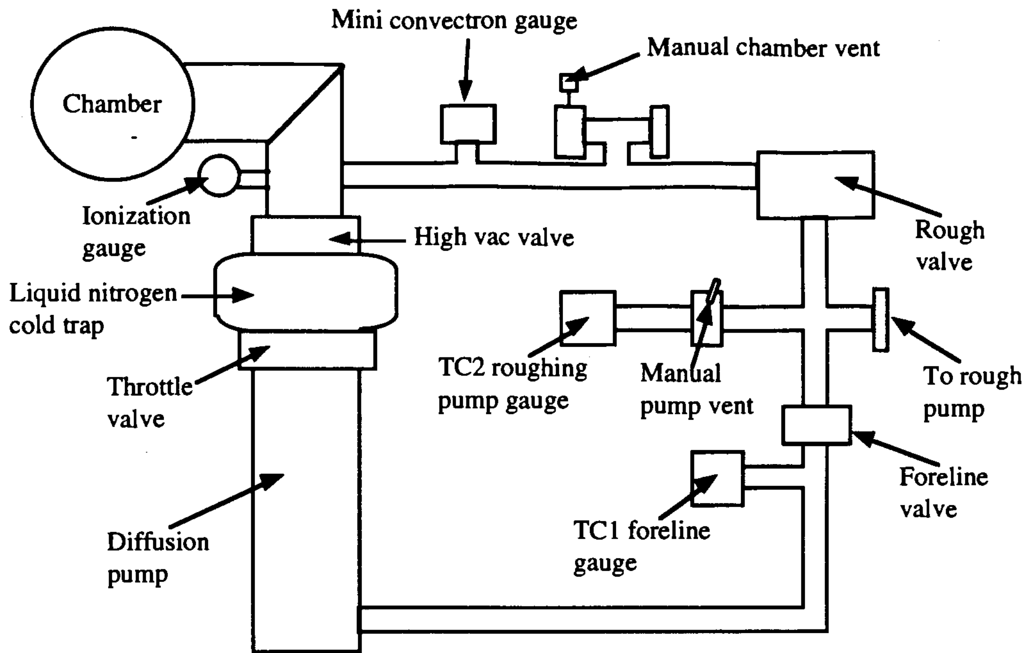

Figure 3.3 - Schematic diagram of the vacuum system.

3.4 Thermal Time Constant

Every mass has a thermal inertia which determines its response speed to changes in heat flow or temperature. Conventional thermal vacuum gauges have a large thermal inertia due to large mass and size. Silicon microstructures have minute dimensions in the order of hundreds of micrometers and low mass of a few micrograms. Thus, these have low thermal inertia and fast response time. This allows the application of a time-varying excitation signal to the heater and an AC response detection at the sense resistor. The relationship between the time constant and the frequency is given as

$$T_c = \frac{1}{2\pi f} \tag{3.2}$$

where T_c is the time constant of the structure and f is the frequency. The thermal time constant of these microstructures determines the upper limit of the frequency of operation for the AC measurement technique.

To determine the thermal time constant of a micromachined structure with polysilicon heater and sense resistors separated by a distance, the heater resistor was driven by a 1 mA zero to peak current square-pulse wave at some frequency. This created sense resistor temperature shifts producing variations in a 0.2 mA bias current flowing through the sensor. The waveform was stored on the Tektronix 2232 storage oscilloscope and was then downloaded as an ASCII file to a Macintosh using Versaterm communication software. The thermal time constant of the structure generated the resulting AC signal as shown in Figure 3.4 .

Note that for 1 mA heater current, there is a spike of about 4% at the rising edge, after which the heater current falls and becomes constant (see Figure 3.4a). This is caused by the change of heater resistance due to the temperature increase resulting from the current drive[35]. This increase in the heater current is noticeable only at high heater current excitation. Figure 3.4b shows that for 0.5 mA heater current, the rise is not even observable. Thus, the electrical time constant has a very small effect on the sense resistor whose response is dominated by the much longer thermal time constant.

For the rising part of the sense signal,

$$I_t = I_1 \exp\left(- {}^{t}/_{T_c}\right) \tag{3.3}$$

$$\ln I_t = \ln I_1 - {}^{t}/_{T_c} \tag{3.4}$$

where I_t is the current at time t, I_1 is the peak current, and T_c is the time constant of the structure. A line fit of the above form to the obtained data thus gave the time constant of the structure.

Thermal time constant of structure 1 plate beam-type poly resistor:

This structure consists of a micromachined oxide suspended plate which thermally isolates two identical 333 μm long, 3.6 μm wide, beam-type polysilicon heater and sense resistors separated by 12 μm, and connected by aluminum lines to the outside world (see Figures 2.8 and 2.9). The 1500 Ω heater resistor was driven by a pulse generator at 80 Hz and the decade resistor box was set to generate a peak current of 1 mA. This created sense resistor temperature shifts producing variation in the sense resistance, and hence the

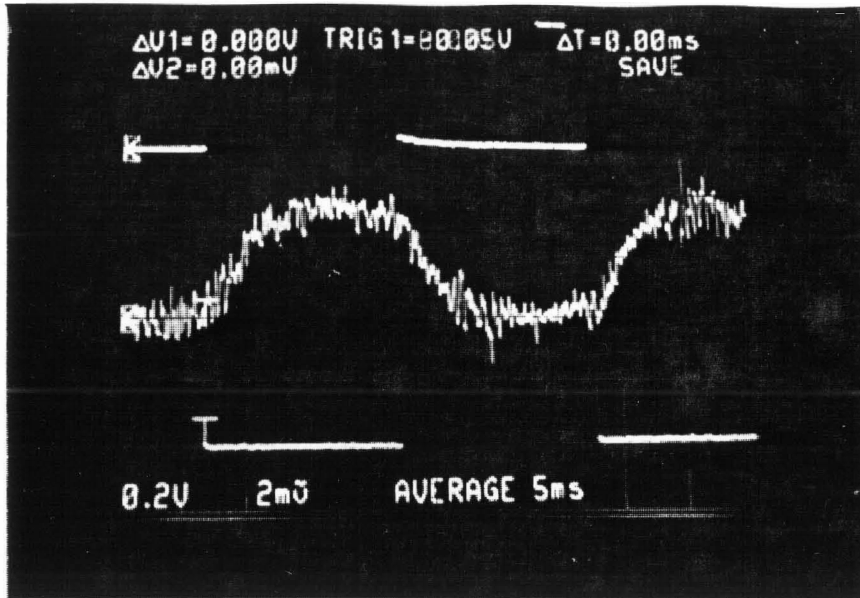

Figure 3.4a - 1 mA heater current. Note the fall in heater current at the rising edge.

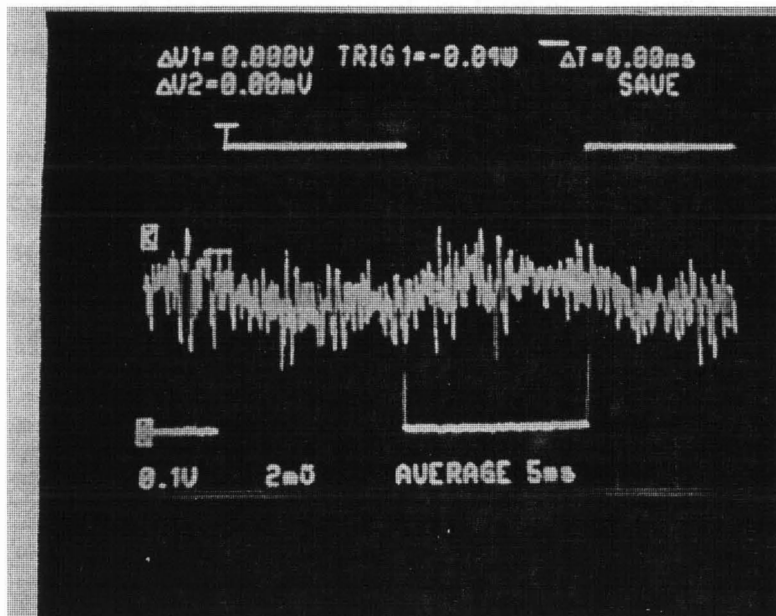

Figure 3.4b - 0.5 mA heater current. Note the fall in heater current at rising edge is absent.

Figure 3.4 - Applied square-pulse heater current and corresponding sense resistor AC current (measured as voltage across 1 KOhm resistor). Note the rise/fall of sensor signal is due to the thermal time constant of the device.

0.2 mA bias current flowing through it. The thermal time constant of the structure generated the resulting AC signal similar to that of Figure 3.5a . The waveform was stored on the Tektronix 2232 storage oscilloscope and was then downloaded as an ASCII file to a Macintosh. Only relevant data points, out of a total of 512, which described the rising behavior of the sense signal were selected for the computation. A linear regression of the form of equation 3.4 to the obtained data (see Figure 3.5a) gave the time constant of the structure as approximately 1.5 msec.

Thermal time constant of structure 3 plate beam-type poly resistor:

This structure consists of three micromachined oxide suspended plates separated by a gap of 6 μm, with approximately 680 μm long, 3.6 μm wide, beam-type polysilicon heater and sense resistors (see Figures 2.10 and 2.11). The 3 KΩ heater resistor was driven by a pulse generator at 55 Hz and the decade box was loaded to generate a current of 1 mA. This created sense resistor temperature shifts producing variations in a 0.2 mA bias current flowing through the sensor. The waveform was again stored on the Tektronix 2232 storage oscilloscope and was then downloaded as an ASCII file to a Macintosh. Only relevant data points which described the rising behavior of the sense signal were selected for the computation. A linear regression of the form of equation 3.4 to the obtained data (see Figure 3.5b) gave the time constant of the structure as approximately 1.8 msec.

As expected, the time constant of structure 1 plate beam-type poly resistor is smaller than the time constant of the structure 3 plate beam-type poly resistor as the latter structure is larger. Also, the thermal time constant of the designed microstructures is close to the 5 msec thermal time constant reported by M. Parameswaran, et al[19], for similar NT's CMOS3 DLM micromachined devices.

3.5 Frequency of Operation

As the frequency of the heater activation signal was increased the amplitude of the AC components in the sense signal was decreased. However, at frequencies lower than 1 Hz the response of the device to changes was slow, and was accompanied by poor rejection of the noise components. Also, for downloading the heater voltage and current waveforms without distortion using the SR850's auxiliary inputs required that the frequency be a multiple of 2^n. A lock-in amplifier fails to measure weak signals at, and near, first and second harmonics of power-line frequency. For these reasons, and

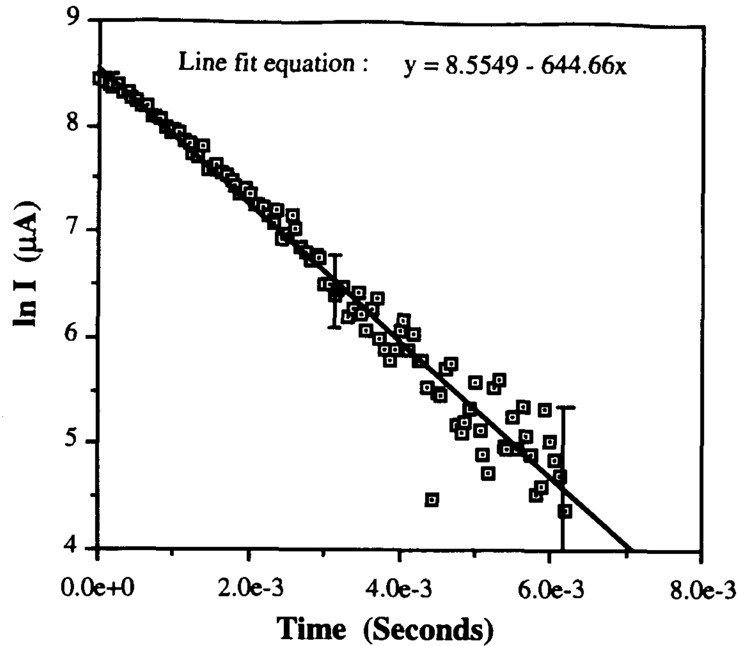

Figure 3.5a - Microstructure 1 plate beam-type poly resistor.

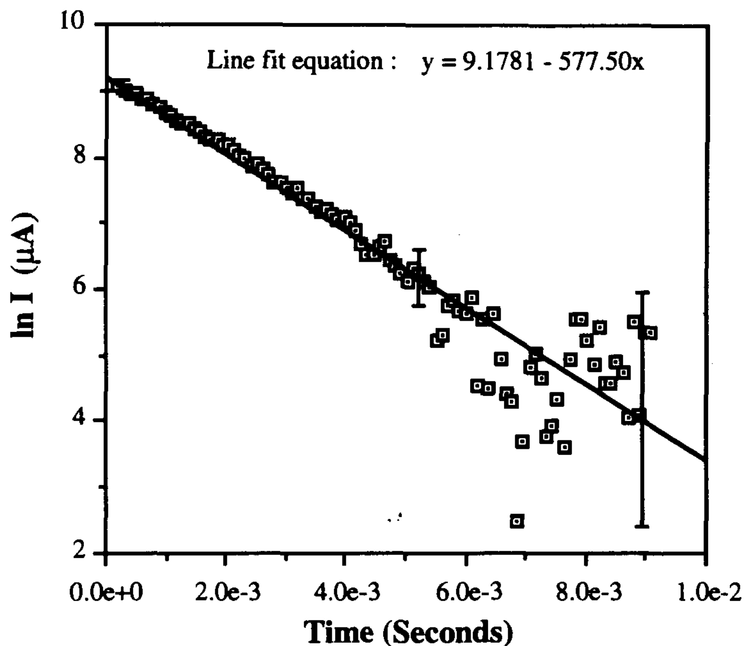

Figure 3.5b - Microstructure 3 plate beam-type poly resistor.

Figure 3.5 - Line-fit to the downloaded data points of sense AC signal to obtain the time constant of the microstructures. The error in the measurement of current from the oscilloscope is 0.2 µA, is constant for all points, and is shown with the error bars for selected points.

experimental observations, 32 Hz was chosen as the excitation frequency of the heater square-pulse signal in all the following investigations. Also, for this frequency the heater driving current time period is 8.8 times the thermal time constant of 1.8 msec of the microstructure. This allows the sense resistor signal to reach the saturation level during the heater current on portion of the cycle as shown in Figure 3.4 .

3.6 Sensing Signal

To measure the AC variations transmitted from the heater side, experiments were done to find out the best responding sensing signal in the sense resistor. Figures 3.6 and 3.7 show the response of a typical microstructure, at 700 Torr and 10^{-5} Torr respectively, for sensing signals of amplitudes 0.1 mA, 0.2 mA and 0.4 mA in the sense resistor. For the calculation of average temperature of sense resistor, see Section 3.7. The heater driving current was varied from 1 mA to 1 μA. The figures show that for a sensing signal of 0.1 mA the response of the sensor saturates at a high heater power dissipation. Linear regression was also done to the above data (see Table 3.1). The 0.1 mA sensing signal has a higher slope both in air and vacuum. However, 0.4 mA sensing signal has a lower intercept which means it can detect lower temperature changes at the sensor. Thus, the comparison shows 0.2 mA sensing signal as a good compromise, and it was employed in all in the following investigations.

Pressure / Sensing signal	700 Torr		10^{-5} Torr	
	Slope (°C/Torr)	Intercept (°C)	Slope (°C/Torr)	Intercept (°C)
0.1 mA	8.018e+3	4.166e-4	7.861e+1	1.496e-4
0.2 mA	7.474e+3	1.890e-4	5.682e+1	7.865e-5
0.4 mA	5.911e+3	6.989e-5	3.083e+1	1.606e-5

Table 3.1 - Slope and intercepts of sensor output at 700 Torr and 10^{-5} Torr for sensing signal of strengths 0.1 mA, 0.2 mA and 0.4 mA.

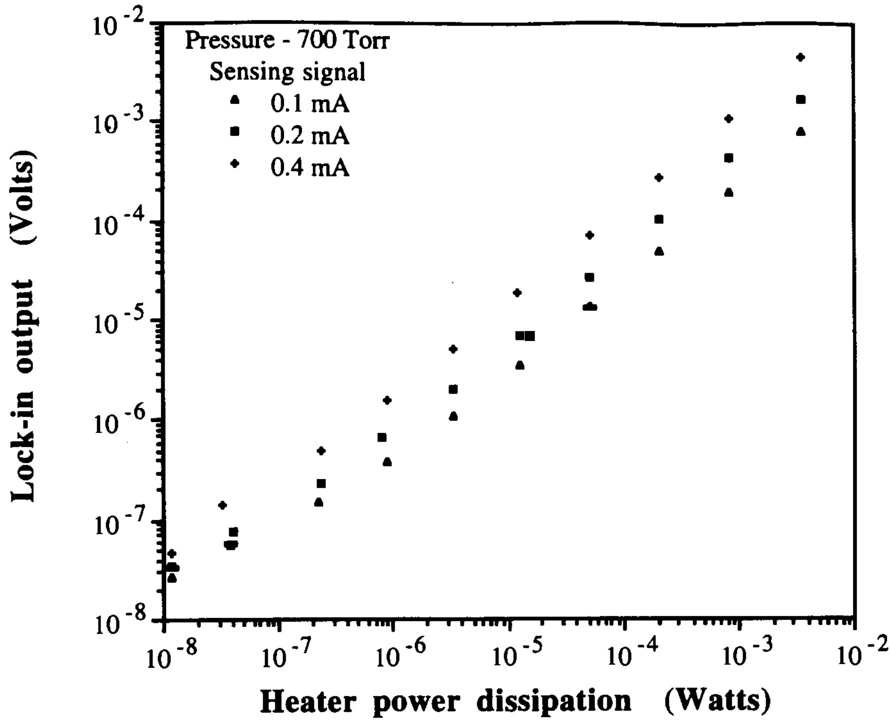

Figure 3.6a - Lock-in output voltage.

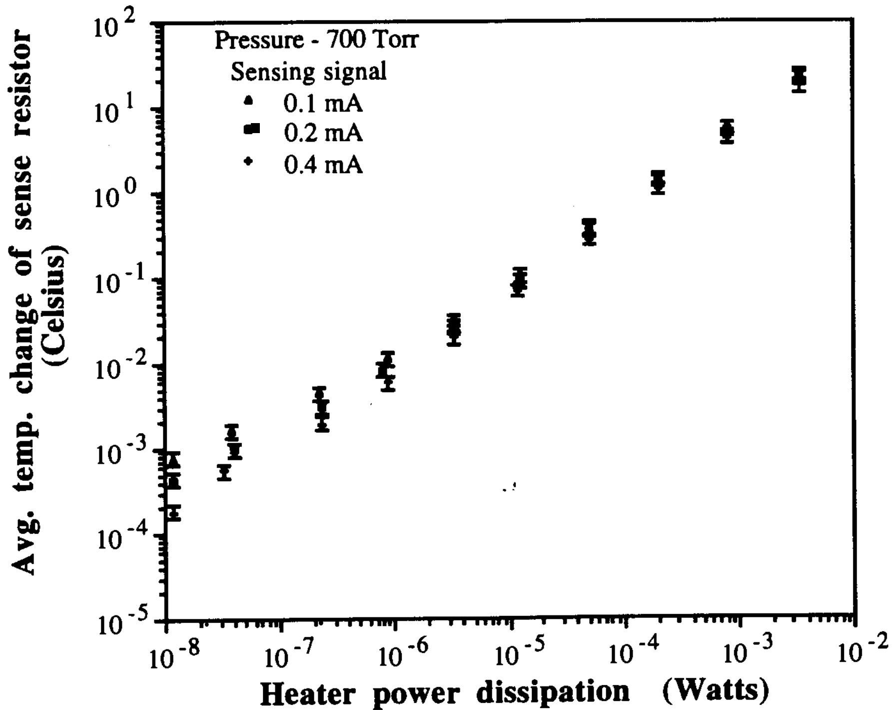

Figure 3.6b - Estimated average temperature change of sense resistor.

Figure 3.6 - Response of sensor to sensing signal of amplitudes 0.1 mA, 0.2 mA and 0.4 mA to various heater power dissipation at 700 Torr.

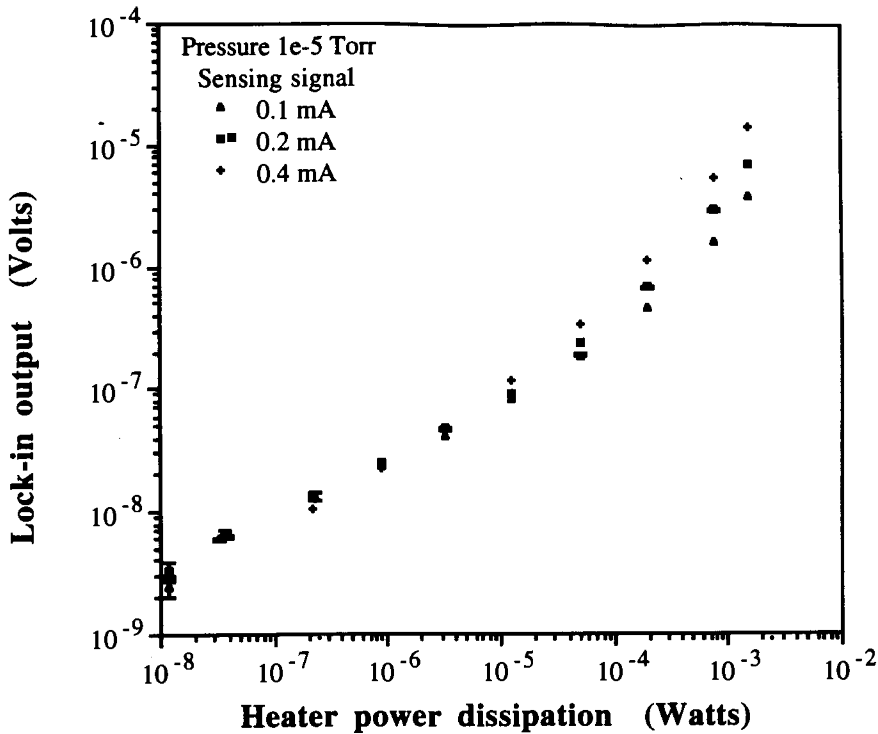

Figure 3.7a - Lock-in output voltage.

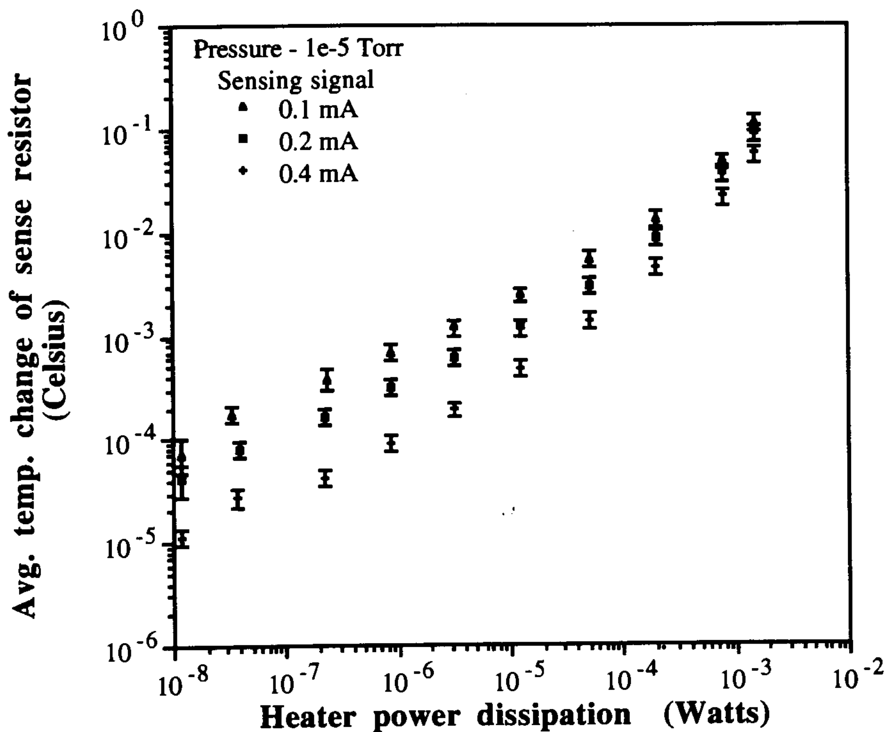

Figure 3.7b - Estimated average temperature change of sense resistor.

Figure 3.7 - Response of sensor to sensing signal of amplitudes 0.1 mA, 0.2 mA and 0.4 mA for various heater power dissipation at 10^{-5} Torr.

3.7 A Sample Calculation

Response of the various devices measured as a voltage by the lock-in is used to estimate the average temperature change of the sense resistor resulting due to the heat flow from the heater resistor for a given heater power dissipation. The measured voltage across the heater resistor R_h and the 1 KΩ resistor R_{hs}, gave the voltage and current for the instantaneous heater power dissipation calculation. To calculate the heater temperature the change in the heater resistance was determined by subtracting the heater resistance at room temperature from the instantaneous resistance obtained by dividing the heater voltage by the heater current. Using the change in resistance and TCR of polysilicon, temperature of the heater was calculated. On the sensor side, the AC shifts in the sensing signal were measured as a voltage across the 1 KΩ R_{ss} resistor. For the readings measured using the lock-in amplifier, a correction factor of 2.48 ± 0.25 was employed to obtain the true amplitude of the signal as it would be obtained from the oscilloscope. The change in current was then translated to change in resistance of the sense resistor using appropriate formula as shown in the following sample calculation. At this stage, using TCR of polysilicon the change in the sense temperature was calculated.

Following is a sample calculation for average change in temperature at the sense resistor at 2×10^{-5} Torr for the 3 plate beam-type poly resistor structure.

Voltage across the heater resistor R_h,

$$V_h = 8.417 \times 10^{-1} \pm 0.021 \times 10^{-1} \text{ Volts}$$

Voltage across the 1 KΩ load resistor R_{hs},

$$V_{hs} = 2.355 \times 10^{-1} \pm 0.015 \times 10^{-1} \text{ Volts}$$

Current through the heater resistor R_h,

$$I_h = \frac{V_{hs}}{10^3} = 2.355 \times 10^{-4} \pm 0.015 \times 10^{-4} \text{ Amperes}$$

Power dissipated in the heater resistor,

$$P_h = V_h \times I_h = 1.982 \times 10^{-4} \pm 0.018 \times 10^{-4} \text{ Watts}$$

Instantaneous resistance of the heater resistor,

$$R'_h = \frac{V_h}{I_h} = 3.574 \times 10^{3} \pm 0.032 \times 10^{3} \text{ Ohms}$$

Resistance of the heater resistor at room temperature,

$$R_h = 3.440 \times 10^{3} \pm 0.010 \times 10^{3} \text{ Ohms}$$

Change in resistance of the heater resistor,

$$\Delta R_h = R'_h - R_h = 1.34 \times 10^{2} \pm 0.42 \times 10^{2} \text{ Ohms}$$

Temperature coefficient of resistance (TCR) of polysilicon (see Section 3.1),

$$\alpha_{poly} = 1.247 \times 10^{-3} \pm 0.017 \times 10^{-3} \text{ Celsius}^{-1}$$

Average change in temperature of the heater resistor,

$$\Delta T_h = \alpha\left(\frac{\Delta R_h}{R_h}\right) = 31 \times 10^{1} \pm 1.0 \times 10^{1} \text{ Celsius}$$

Room temperature, $T_{room} = 22^{\circ}$ Celsius

Average temperature of the heater resistor,

$$T_h = T_{room} + \Delta T_h = 5.3 \times 10^{1} \pm 1.0 \times 10^{1} \text{ Celsius}$$

The estimated value of average temperature of the heater resistor has a high statistical deviation because of a progression in errors, especially after the calculation of the change in the heater resistance derived after subtracting the heater resistance at room temperature from the instantaneous heater resistance for a given power dissipation.

On the sense resistor side,

Voltage across the 1 KΩ load resistor R_{ss},

$$V_{ss} = 6.740 \times 10^{-7} \pm 0.057 \times 10^{-7} \text{ Volts}$$

Correction factor for the lock-in readings, $K_{lock-in} = 2.48 \pm 0.25$

Actual voltage across the 1 KΩ load resistor R_{ss},

$$V'_{ss} = K_{lock-in} \times V_{ss} = 1.67 \times 10^{-6} \pm 0.18 \times 10^{-6} \text{ Volts}$$

Current through the sense resistor R_s,

$$I_s = \frac{V'_{ss}}{10^3} = 1.67 \times 10^{-6} \pm 0.18 \times 10^{-6} \text{ Amperes}$$

Voltage divider resistor, $R_1 = 2.34 \times 10^3 \pm 0.01 \times 10^3$ Ohms

Voltage divider resistor, $R_2 = 7.20 \times 10^3 \pm 0.01 \times 10^3$ Ohms

Total resistance, $R_{total} = R_1 + R_2 = 9.54 \times 10^3 \pm 0.01 \times 10^3$ Ohms

Sense resistor resistance at room temperature,

$$R_s = 3.16 \times 10^3 \pm 0.01 \times 10^3 \text{ Ohms}$$

The source voltage, $V_{dc} = 1.581 \pm 0.004$ Volts

For calculating the change in resistance of the sense resistor refer to the circuit (see Figure 3.2). The current I_s through the sense resistor R_s and the 1 KΩ load resistor R_{ss} is given by,

$$I_s = \frac{V_{dc} R_2}{\left[R_s(R_1 + R_2) + R_{ss}(R_1 + R_2) + R_1 R_2\right]}$$

The resistors R_1, R_2, R_{ss} and the voltage source V_{dc} have fixed values. The sense resistor resistance R_s varies with the heat transfer from the heater resistor R_h. For small changes in the current I_s,

$$\Delta I_s = -\frac{V_{dc} R_2 (R_1 + R_2)}{[R_s(R_1 + R_2) + R_{ss}(R_1 + R_2) + R_1 R_2]^2} \Delta R_s$$

The negative sign indicates that as R_s increases, I_s decrease. Hence, the change in the sense resistor resistance is given by,

$$\Delta R_s = \frac{I_s[(R_s + R_{ss})R_{total} + R_1 R_2]^2}{V_{dc} R_2 R_{total}}$$

For the sample calculation,

$$\Delta R_s = 3.40 \times 10^{-2} \pm 0.55 \times 10^{-2} \text{ Ohms}$$

Average temperature change of the sense resistor,

$$\Delta T_s = \alpha\left(\frac{\Delta R_s}{R_s}\right) = 8.6 \times 10^{-3} \pm 1.5 \times 10^{-3} \text{ Celsius}$$

Hence, for a power dissipation of 198 μW in the heater resistor, an average temperature change of 8.6 millidegree Celsius temperature was measured at the sense resistor (see Figure 3.6b).

Notice that the output voltage measured at the lock-in has less than 1% statistical deviation, but the estimated average temperature change noted at the sense resistor has more than 15% deviation. This is due to the progression in errors as calculations are done, and more parameters with finite standard deviation in their values are taken into account, to convert the output voltage into change of sensor temperature.

3.8 Comparison of Various Structures

Many silicon microstructures such as 3 plate beam-type poly resistor structure, 3 plate meander-type poly resistor structure and 2 plate meander-type poly resistor structure were designed, fabricated and micromachined to realize a vacuum sensor based on the proposed principle of operation and measurement technique. Experiments were done to determine the structure which offered the highest sensitivity to the applied phase-sensitive measurement technique. Figure 3.8 shows the response of the three structures to heater power dissipation from 2 mW to 1 μW. The structure 3 plate beam-type poly structure gives a larger sense response for a given power dissipation in the heater, possibly due to better coupling between the heater and the sense resistor. Also, this structure has a simple design which results in ease of thermal modeling and analysis. Thus, this structure was chosen for further investigations to determine its feasibility as a vacuum sensor.

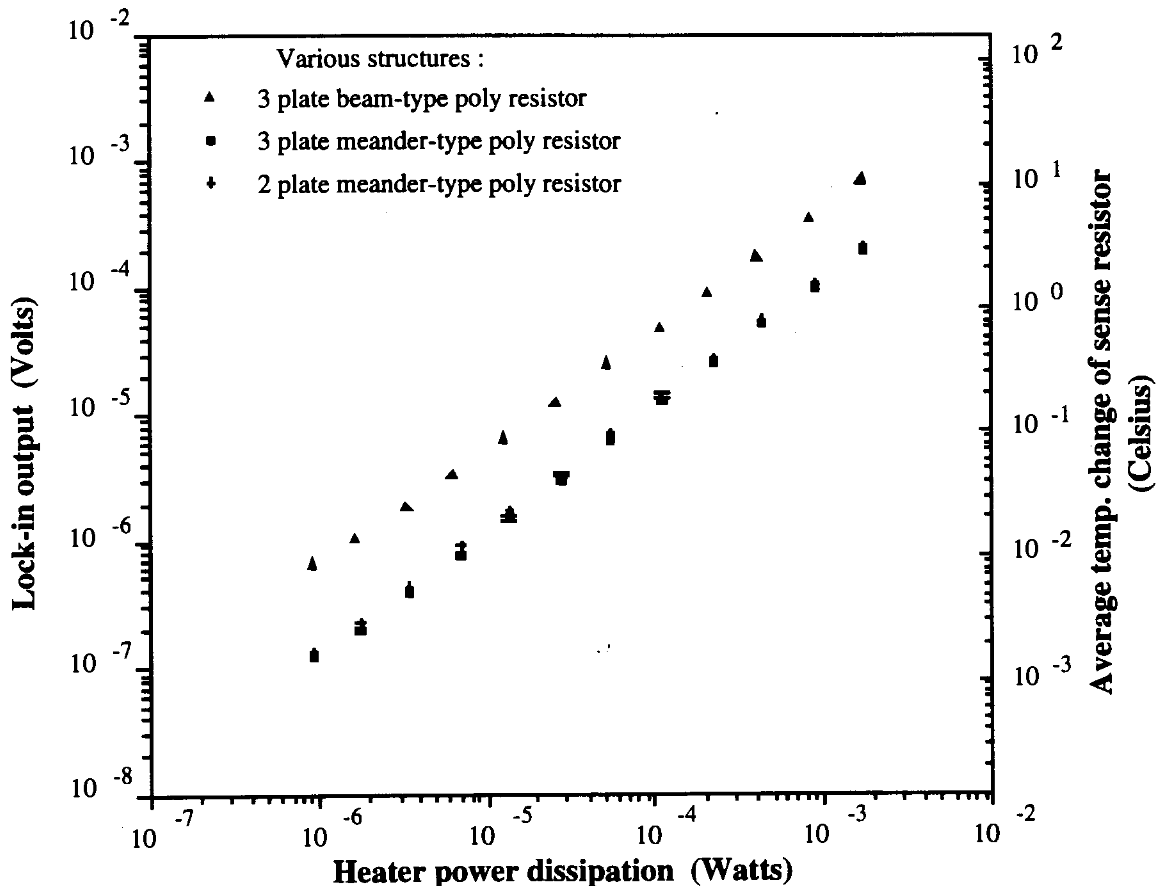

Figure 3.8 - Comparison of response of various structures designed for investigation as a vacuum sensor.

3.9 Minimum Temperature Change

The 3 plate beam-type poly resistor structure was tested for the minimum change in temperature measurable at the sense resistor as power dissipation in the heater resistor was decreased. The 3 KΩ heater resistor of the structure was excited with square-pulses of peak amplitudes 1 mA to 1 μA current and the temperature change at the sense resistor was noted. Figure 3.9 shows the response of two such samples at room pressure 700 Torr. Table 3.2 lists the measured heater power dissipation, lock-in output voltage, the estimated average temperature change of the sense resistor and the statistical deviations calculated over 5120 points at 700 Torr pressure for Sample 1 . It is to be noted that deviation is very small on the measured lock-in output voltage.

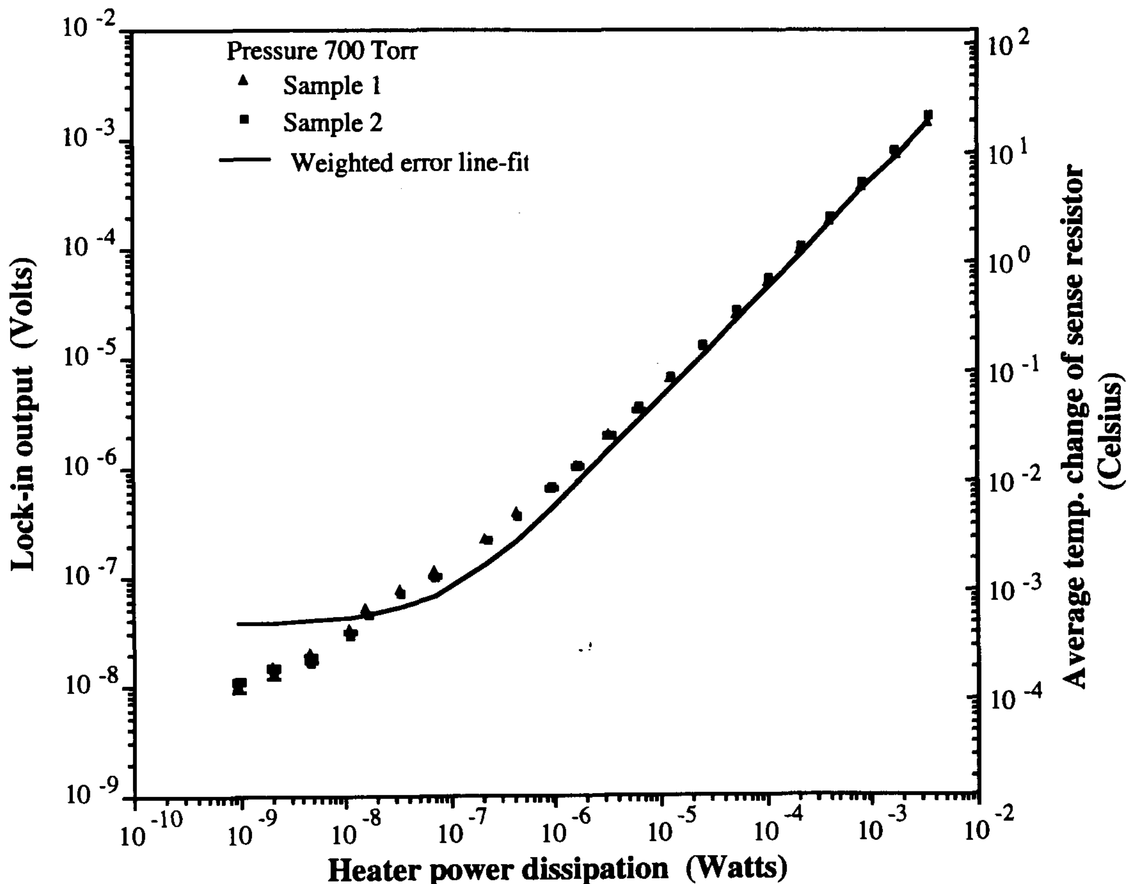

Figure 3.9 - Output voltage and the estimated average temperature change of sense resistor for various power dissipation in the heater resistor at 700 Torr.

Heater power dissipation (Watts)	Lock-in output (Volts)	Standard deviation (Volts)	Average temp. change of sense resistor (Celsius)	Standard deviation (Celsius)
3.455E-03	1.419E-03	6.744E-07	1.952E+01	3.016E+00
1.703E-03	7.148E-04	0.000E+00	9.833E+00	1.515E+00
8.416E-04	3.586E-04	4.915E-07	4.934E+00	7.668E-01
4.102E-04	1.771E-04	2.920E-07	2.436E+00	3.793E-01
2.121E-04	9.280E-05	1.738E-07	1.277E+00	1.991E-01
1.062E-04	4.729E-05	1.043E-07	6.506E-01	1.017E-01
5.323E-05	2.425E-05	4.148E-08	3.336E-01	5.196E-02
2.615E-05	1.227E-05	1.179E-08	1.687E-01	2.616E-02
1.277E-05	6.297E-06	1.324E-08	8.662E-02	1.353E-02
6.374E-06	3.352E-06	8.278E-09	4.612E-02	7.218E-03
3.374E-06	1.912E-06	7.304E-09	2.631E-02	4.153E-03
1.641E-06	1.026E-06	4.610E-09	1.412E-02	2.238E-03
9.103E-07	6.483E-07	2.209E-09	8.918E-03	1.404E-03
4.388E-07	3.773E-07	1.777E-09	5.191E-03	8.241E-04
2.201E-07	2.238E-07	1.294E-09	3.078E-03	4.920E-04
7.005E-08	1.136E-07	6.832E-10	1.562E-03	2.501E-04
3.412E-08	7.536E-08	6.247E-10	1.037E-03	1.769E-04
1.610E-08	5.127E-08	5.956E-10	7.053E-04	1.168E-04
1.086E-08	3.178E-08	3.747E-10	4.372E-04	7.250E-05
4.501E-09	1.939E-08	4.009E-10	2.667E-04	4.660E-05
2.068E-09	1.481E-08	5.040E-10	2.037E-04	3.831E-05
9.403E-10	1.009E-08	1.290E-09	1.388E-04	3.914E-05

Table 3.2 - Measured heater power dissipation, lock-in output and the estimated temperature change of sense resistor for Sample 1 at 700 Torr.

The samples were also placed in the vacuum chamber and the response was measured at various pressures (see Figure 3.10). The plots indicate that temperature change of the order of less than 0.5 millidegree Celsius at the sensor is detected. Thus, a high sensitivity is achieved in the measurement of heat flow due to the design and measurement technique. However, the plots also show a non-linear behavior below sensor output of approximately 1 μV (estimated sense temperature change of 10^{-2} °C), and indicate a saturation in the output of the device. This saturation effect is discussed in detail in Chapter 5.

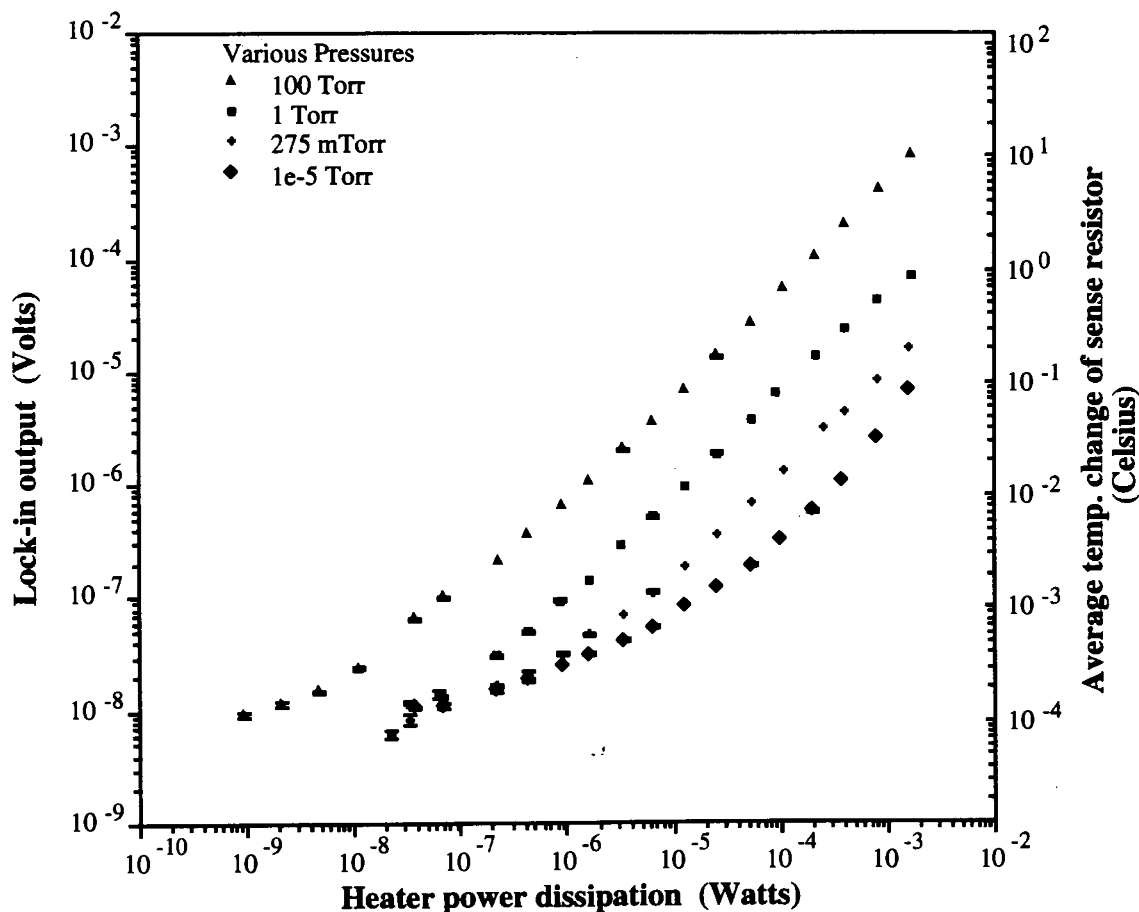

Figure 3.10 - Output voltage and the estimated average temperature change of sense resistor for various power dissipation in the heater resistor at various pressures.

3.10 Orientation Dependent Heat Transfer

To investigate the convective heat loss occurring in the designed microstructure, the samples were placed in different orientations, such as flat and vertical, and the change in temperature at the sensor was measured for various power dissipation in the heater. Figure 3.11 shows the response of a sample at various orientations at 700 Torr. The difference in the change in temperature at the sensor for different orientations is too small to be practically distinguishable. For these reasons, any heat loss or transfer by natural convection currents in the gas is ruled out.

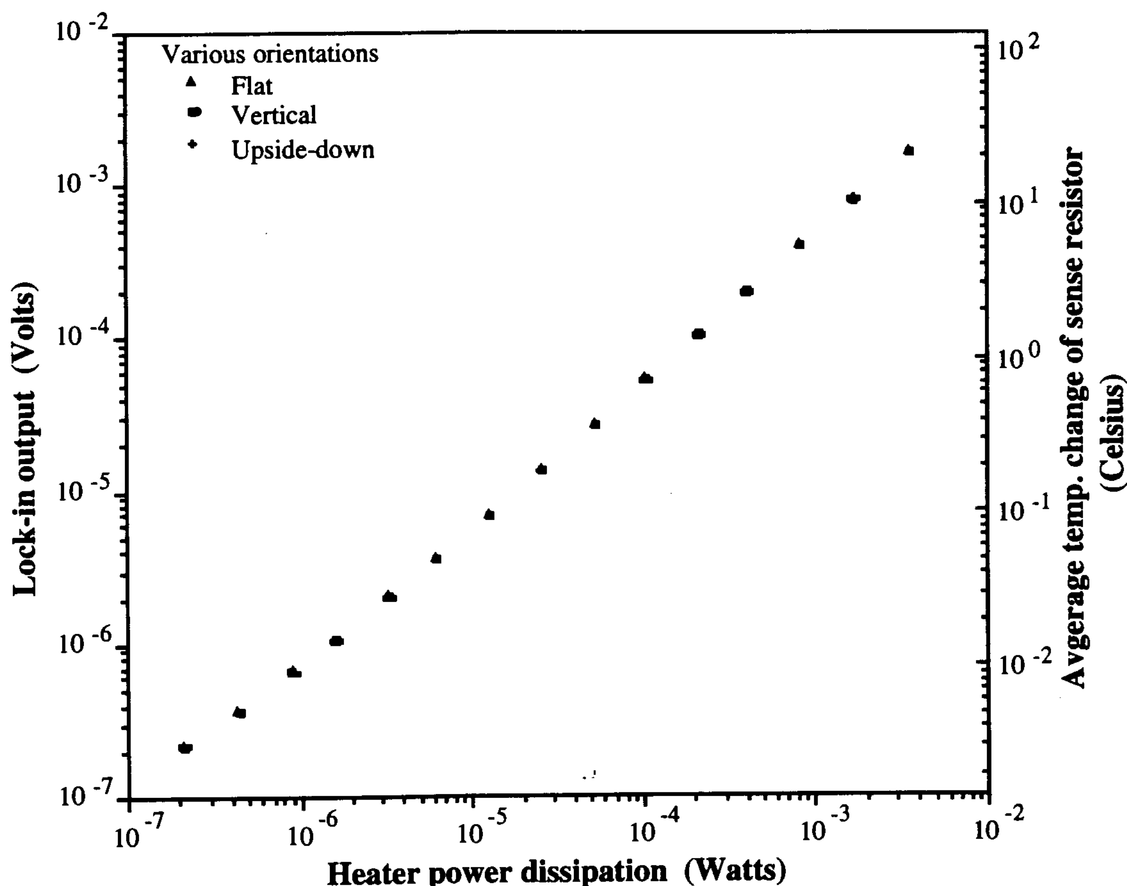

Figure 3.11 - Output voltage and the estimated average temperature change of sense resistor for various orientations at 700 Torr.

3.11 Response at Various Pressures

To investigate the operation of the designed structure 3 plate beam-type poly resistor as a vacuum sensor, the chip containing the device was put in the vacuum chamber of the Corona sputter coater. The connecting wires were taken out of the chamber using an 8-pin feedthrough. The chamber pressure was varied from 700 Torr to approximately 3×10^{-7} Torr, and was stabilized at various intermediate pressures by closing the control valves to isolate the evacuation pumps, and controlling the input of gas through mass flow controllers. The lock-in output was noted for constant voltage and constant temperature excitation of the heater resistor at various pressures, and the estimated average temperature change of sense resistor was calculated. Unless stated, the response of sensor reported is measured in nitrogen gas.

3.12 Constant Voltage Operation

Figure 3.12 shows output voltage, and estimated average temperature change of sense resistor, at various pressures in nitrogen atmosphere for 2.5 Volts and 1.7 Volts constant voltage excitation of the heater resistor. At about 10^{-2} Torr, a saturation in the output of the sensor is noticed. However, a large change in the temperature of heater resistor was noticed as pressure varied from 700 Torr to 10^{-2} Torr. Figure 3.13 shows the temperature of the heater resistor with pressure for constant heater voltage excitations of 2.5 Volts and 1.7 Volts. For 2.5 Volts heater resistor excitation, the heater temperature varies from approximately 50° C at 700 Torr to 450° C at 10^{-2} Torr pressure and saturates. For 1.7 Volts heater excitation, the heater temperature varies from approximately 40° C at room pressure to 250° C at 10^{-2} Torr pressure and saturates. Thus, a constant voltage excitation of the heater which produces negligible rise in the heater temperature at room pressure saturates the heater at high temperature at low pressure. This results in higher heat transfer due to radiation, independent of the gas molecule concentration, thereby giving readings which might not have a relationship to pressure. This suggests that a superior measurement of heat flow would result if the heater temperature remained constant. The next section reports the response of the sensor for constant heater temperature mode.

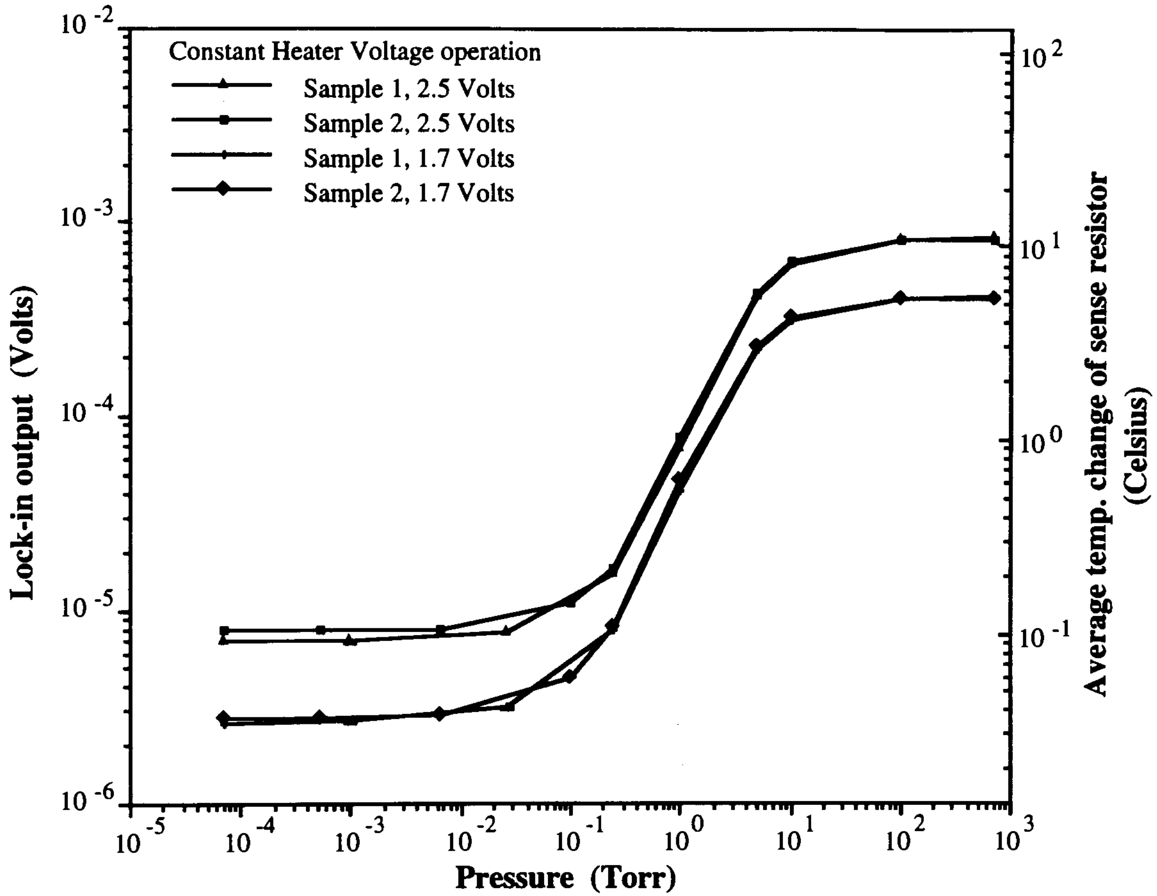

Figure 3.12 - Output voltage and the estimated average temperature change of sense resistor with pressure for constant voltage operation of the heater resistor.

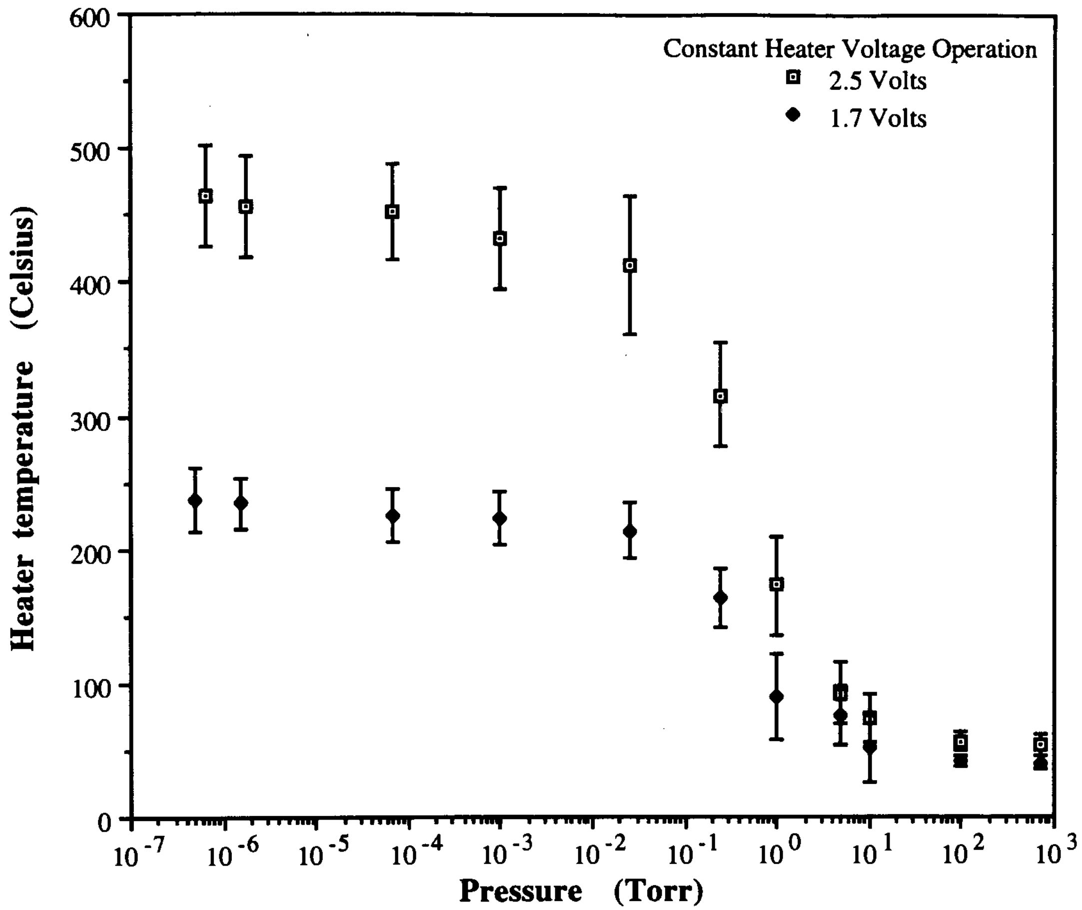

Figure 3.13 - Heater temperature variation with pressure for constant voltage operation of the heater resistor.

3.13 Constant Temperature Operation

Most of the commercial vacuum gauges are operated in constant power mode. The operation of the heater resistor in constant voltage mode indicates a domination of the sense resistance changes due to the change in the heater temperature which increases from 40° C at room pressure to 450° C at 10^{-2} Torr. This suggests that a superior measurement of heat flow would result if the heater temperature remained constant. The circuitry to operate the designed vacuum sensor at a constant temperature has not yet been designed, and was not available. Constant power circuitry existed, but would not generate constant temperature heater operation with change in pressure. Constant temperature circuitry would adjust the current to maintain the change in the heater resistance at a constant value independent of the change in the temperature of the heater resistor with pressure.

To investigate the sense response at constant temperature excitation of the heater, a family of curves of sense response with change in heater power at various pressures (similar to Figure 3.10) was obtained. The sense response corresponding to heater temperatures of 200° C, 125° C, 75° C and 40° C was then obtained by interpolation. Figure 3.14 and Figure 3.16 show the response of sensor at various constant temperature operation of two sample devices.

The plots indicate that for constant heater temperature excitation the sensor response changes very slowly from 700 Torr to about 100 Torr. In this upper pressure range, the molecules are in viscous state and heat transfer is not proportional to pressure. Below 100 Torr, the sensor output changes rapidly. This is the region where heat transfer becomes proportional to the density of the molecules. However, below 10^{-2} Torr the change in the sensor output is small, and does not decrease in proportion to the density of molecules in vacuum the chamber. This behavior indicates saturation, and is discussed in detail in Chapter 5 . However, the output is still distinctively measurable at various pressures below 10^{-2} Torr (see Figures 3.15 and 3.17).

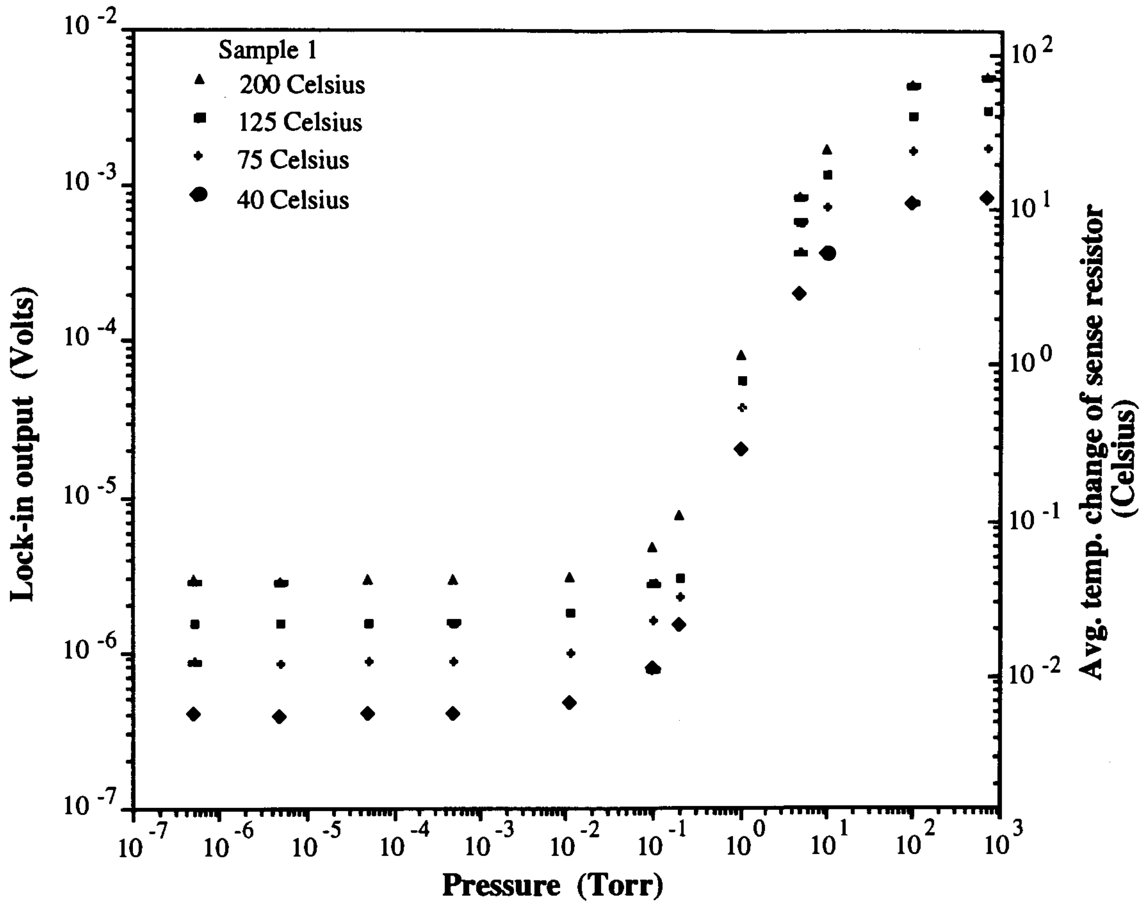

Figure 3.14 - Output voltage and the estimated average temperature change of sense resistor with pressure of Sample 1 for constant heater temperature excitation of 200° C, 125° C, 75° C and 40° C.

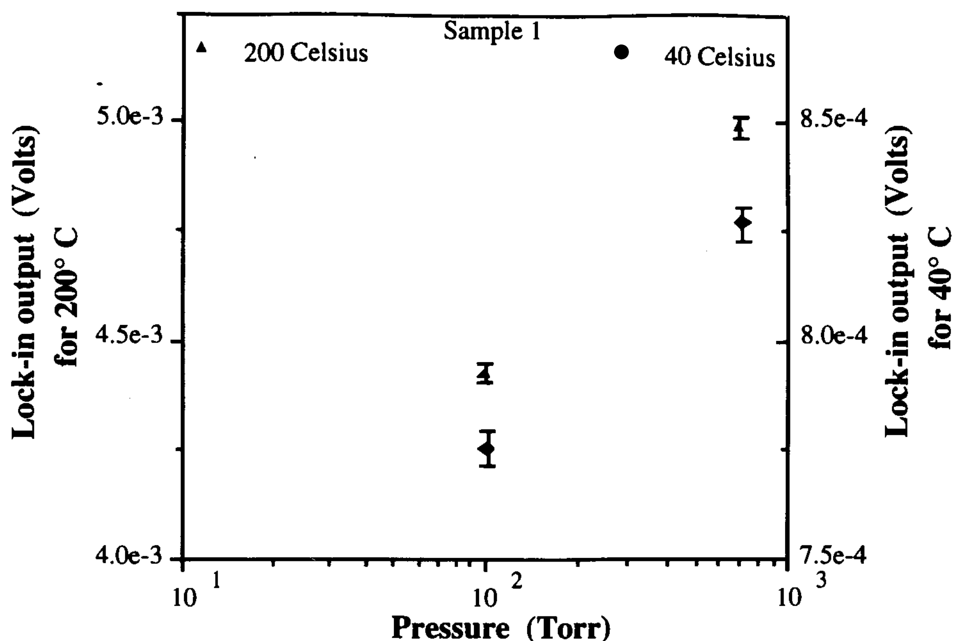

Figure 3.15a - Atmospheric pressure to 100 Torr.

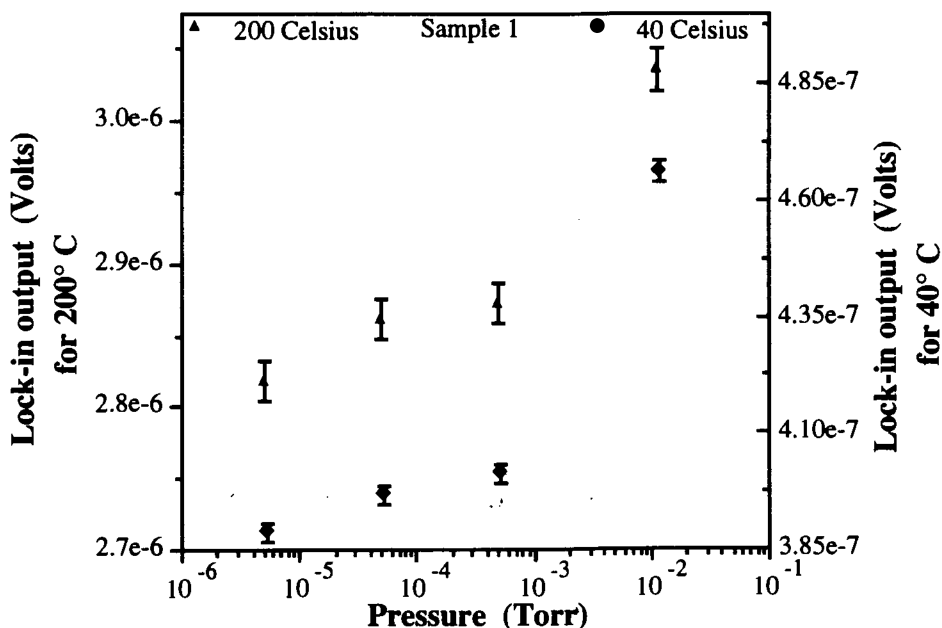

Figure 3.15b - 10^{-2} Torr to 10^{-6} Torr.

Figure 3.15 - Output voltage and the estimated average temperature change, on magnified scale, of sense resistor with pressure of Sample 1 for constant heater temperature excitation of 200° C and 40° C.

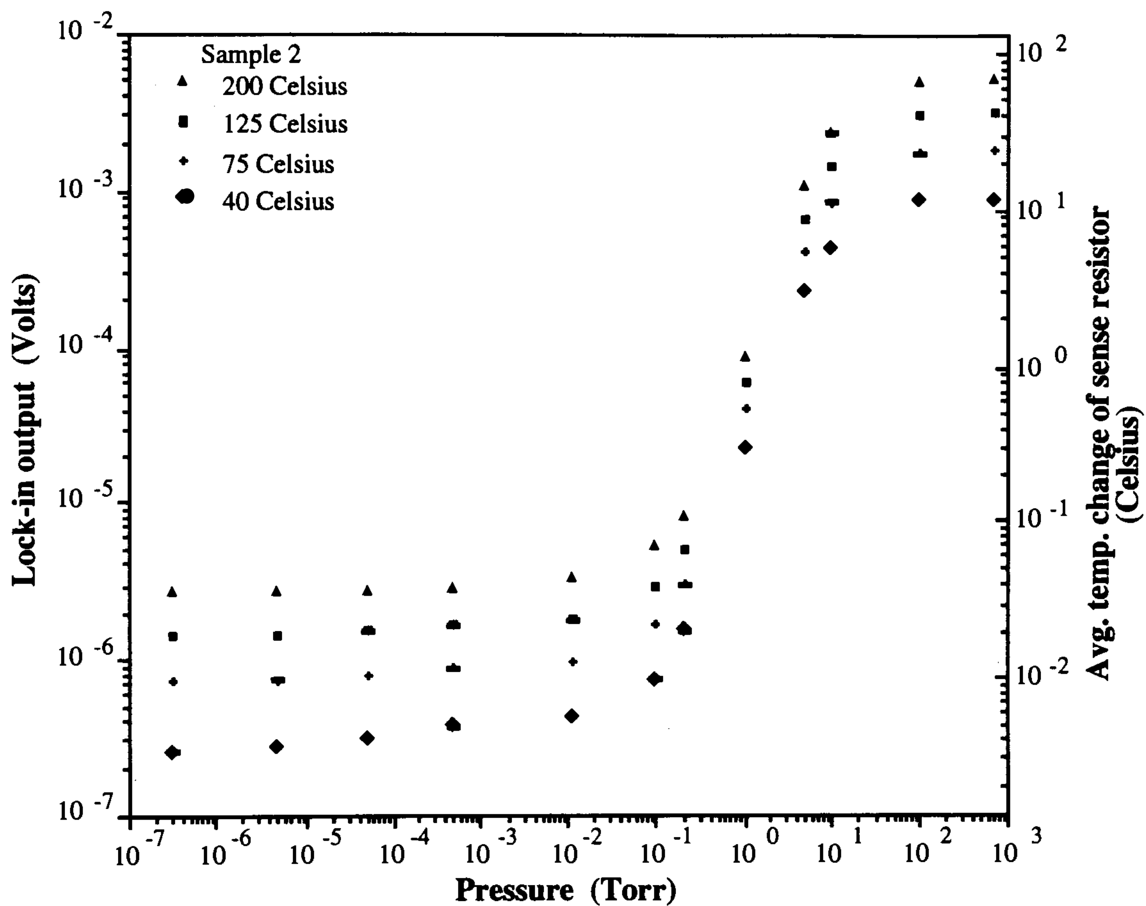

Figure 3.16 - Output voltage and the estimated average temperature change of sense resistor with pressure of Sample 2 for constant heater temperature excitation of 200° C, 125° C, 75° C and 40° C.

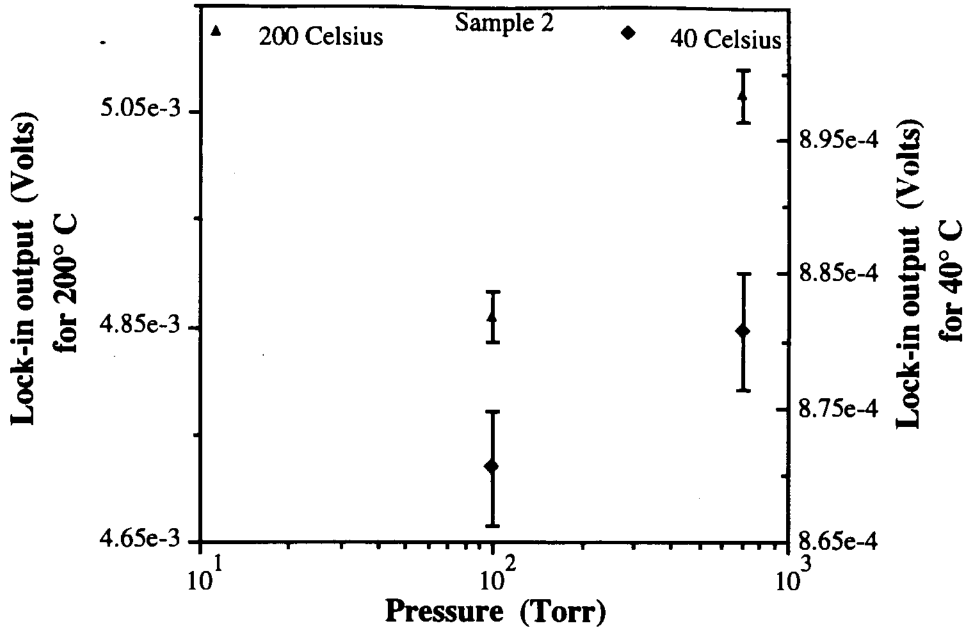

Figure 3.17a - Atmospheric pressure to 100 Torr.

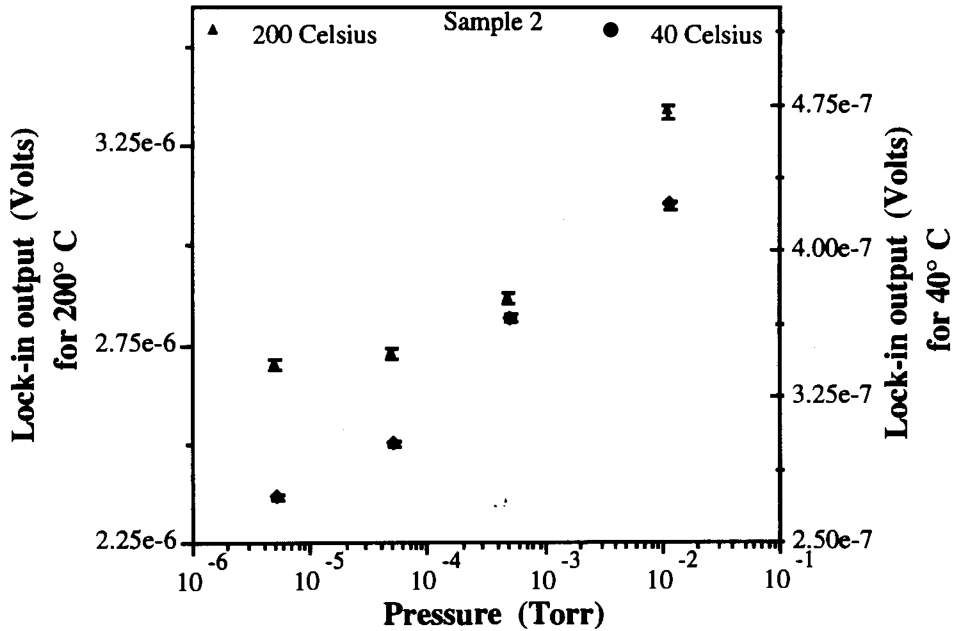

Figure 3.17a - 10^{-2} Torr to 10^{-6} Torr.

Figure 3.17 - Output voltage and the estimated average temperature change, on magnified scale, of sense resistor with pressure of Sample 2 for constant heater temperature excitation of 200° C and 40° C.

3.14 Response in Nitrogen and Argon

The thermal flow through a gas is dependent on the molecular mass of the surrounding gas molecules. Figure 3.18 compares the response of the sensor in argon and nitrogen gas for constant heater temperature excitation at 125° C and 40° C. The average temperature change of sense resistor in argon is less than that in nitrogen, even though the argon molecules are lighter than nitrogen (Ar = 18, N_2 = 28), and the heat transfer is inversely proportional to the square root of the molecular mass (see Equation 2.9) of the gas molecules present. This is because of another gas-dependent term $(\gamma + 1)/(\gamma - 1)$ in the Equation 2.9 as shown below in the relationship with pressure -

$$E = \frac{1.47 \times 10^{-12}}{M^{1/2}} \left(\frac{\gamma + 1}{\gamma - 1} \right) \alpha \sqrt{\frac{273}{T_2}} (T_1 - T_2) P \quad (3.5)$$

For 40° C heater temperature excitation at 700 Torr, the sensor notes an average temperature change of 12.6° C for nitrogen and 10.3° C for argon. Hence, the ratio of the heat transfer is approximately 1.2 . Theoretically, for $\gamma_{nitrogen} = 1.405$ and $\gamma_{argon} = 1.667$ [51], the ratio of heat transfer calculated using equation 2.9 is also 1.2 . This explains the low temperature change observed in the case of argon.

3.15 Summary

To sum up the experimental results, average temperature changes of less than 0.5 millidegree Celsius at the sense resistor can be detected. The heat transfer from heater resistor to the sense resistor is by molecules of the gas present in the vacuum chamber. However, with change in pressure the average temperature change of the sense resistor does not decrease in proportion to the density of molecules in the vacuum chamber. A detailed analysis of this saturation effect observed in the output of the device is reported in Chapter 5. The next chapter discusses the finite-element modeling of the heat transfer from the heater resistor to the sense resistor of the designed vacuum sensor. The modeling results are compared to the experimental results, and the validity of the measured average change in temperature of sense resistor is established.

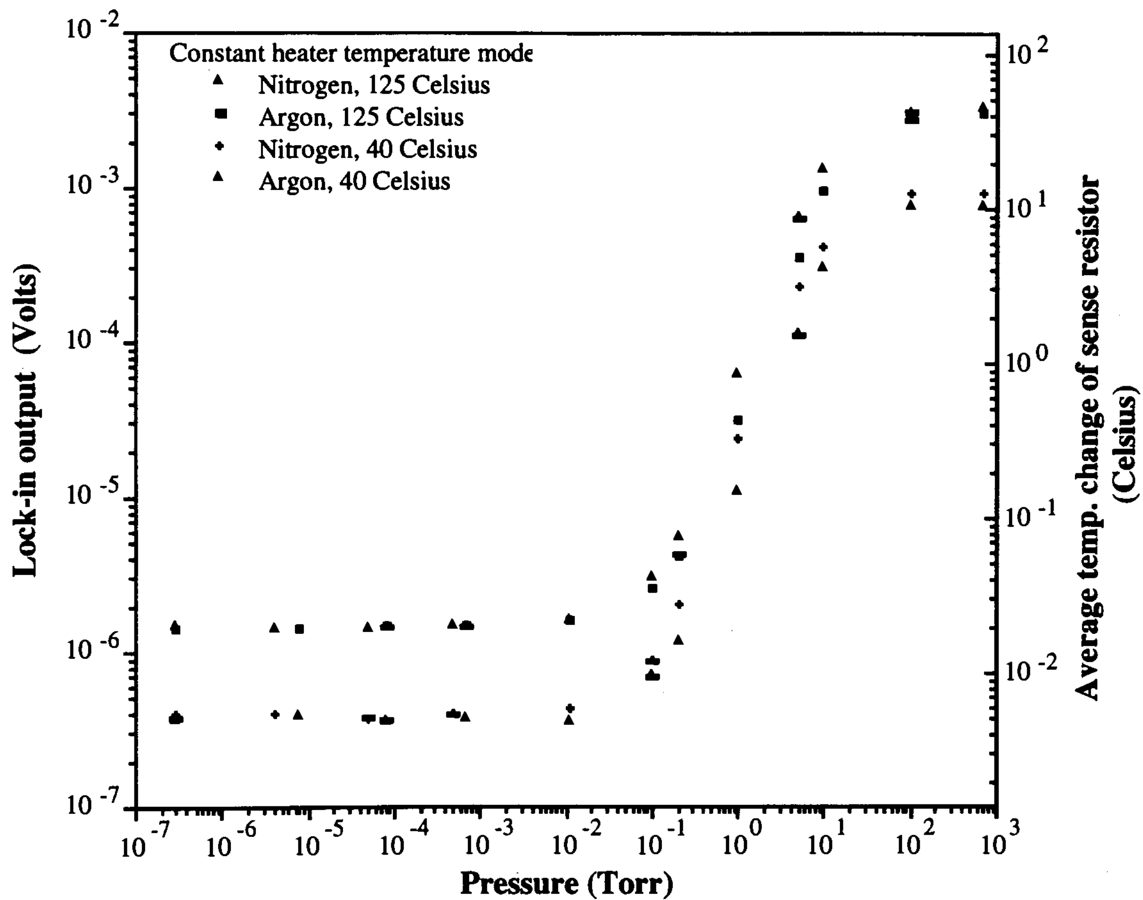

Figure 3.18 - Comparison of sensor response in nitrogen and argon atmosphere for constant heater temperature excitation of 125° C and 40° C.

4 Modeling

This chapter discusses finite element modeling of heat transfer from the heater resistor to the sense resistor of the designed silicon micromachined vacuum sensor. Modeling results are compared to experimental results, and the validity of the estimated average change in temperature of the sense resistor is established. The thickness of various layers constituting the NT's CMOS3 DLM microstructures, and their thermal conductivity is also reported.

4.1 Finite Element Analysis

Finite element modeling is a numerical method of solving engineering and mathematical physics problems in areas of structural analysis, heat transfer, fluid flow, mass transport, and electromagnetic potential, involving complicated geometries, loadings, and material properties.

Analytical solutions are given by a mathematical expression that yields the value of desired unknown quantities at any location in a body. These analytical solutions generally require the solution of ordinary or partial differential equations, which in case of the complex geometries, loadings and material properties, are not usually obtainable. Hence, numerical methods such as the finite element method, which formulates a system of simultaneous algebraic equations rather than requiring the solution of complex differential equations, are employed for acceptable solutions. This numerical method yields approximate values of the unknowns at a discrete number of points. This process of modeling a body by dividing it into an equivalent system of smaller bodies or finite elements interconnected at points common to two or more elements (nodal points or

nodes), and possibly boundary lines and surfaces is called discretization. Thus, instead of solving the problem for the entire body in one operation, one formulates the equations for each finite element and combines them to obtain the solution of the whole body.

Briefly, the solution for heat transfer problems typically involves to determining the temperatures at each node and the thermal flow within each element making up the structure that is subjected to loads such as internal heat generation, boundary temperature, etc.

With the advent of the computer and increased computation capability, numerous general-purpose and special-purpose programs have been written to handle various complicated structural, thermal, fluid, mass transport, and electromagnetic potential problems. ALGOR, ANSYS, GIFTS, IMAGES-3D, MSC/PAL, and TAB/SAP86 are a few of the finite element solver programs[52].

The educational institution version of finite element analysis software ANSYS by Swanson Associates Corp., available on the departmental UNIX network and running on Sun Sparcstation computer, was used for the thermal analysis of the designed microstructures. To use the program, a finite element model of the designed microstructural vacuum sensor is defined and information regarding the position of the element nodal coordinates, the manner in which the elements are connected, the material properties of the elements, the applied load and the boundary conditions, and the kind of analysis to be performed is fed into the program. This is the very first step of the procedure and is called as preprocessing. In the second step, solving, the program uses the information from the preprocessing step to generate and solve the equations to carry out the analysis. In the final step, postprocessing, the raw solution data generated after the solving step can be translated to colour graphs and contours for easy interpretation and viewing of the results.

The main purpose of the use of finite element modeling in this case was to establish the validity of the estimated average temperature change of the sense resistor for various heater power dissipation.

4.2 Thermal Analysis

The structure 3 plate beam-type poly resistor (see Figures 2.10 and 2.11), has the heater and sense resistors separated by a gap. For such a microstructure, the amount and mode of heat transfer from the heater resistor to the surrounding gas, and to the sense resistor across the gap, is not very certain. Another micromachined structure, 1 plate beam-type poly resistor (see Figures 2.8 and 2.9), has the heater and sense resistors on the same plate and separated only by a thin layer of silicon dioxide. If this device is excited in a vacuum environment, the heat generated by the heater resistor can transfer only through the support silicon dioxide arms and connecting metal leads to the substrate silicon acting as a heat sink. Due to the vacuum condition, there is no heat transfer to surrounding fluid, or gas. This simplifies the analysis of temperature distribution, and calculation of the amount of heat transfer to the sense resistor. Thus, finite element analysis is performed first on the 1 plate beam-type poly resistor structure. The assumptions, and results, are then extended to the analysis of 3 plate beam-type poly resistor structure.

The thickness and thermal conductivity of various layers of the designed microstructures, required for the finite element modeling are discussed in the next section.

4.3 Thickness of Various Layers

Figures 2.8a and 2.10a show the schematic cross-sectional view of the structures 1 plate beam-type poly resistor and 3 plate beam-type poly resistor respectively. The microbridges of the structures fabricated using NT's CMOS3 DLM IC fabrication process consist of many layers such as field oxide, polysilicon, CVD 1, Metal 1, CVD 2 and passivation layer[39]. The thickness of these layers was obtained from Northern Telecom and is shown in Table 4.1 .

Also, several unetched sample microstructure devices were cleaved at the center of the microbridge. They were dipped in buffered oxide etch (BOE) for 20 seconds to provide the separation marking between the oxide layers and silicon. Then the edge was photographed using a scanning electron microscope. Figure 4.1 shows one such photograph with a distinctively visible cross-section of a beam-type polysilicon resistor. The polysilicon resistor was designed to be 3.6 μm wide, and conforms to the width obtained from the photograph. The thickness of the polysilicon layer from the SEM

Layer	Thickness (μm)
Passivation	1.0
Metal 2	1.1
CVD 1, CVD 2	1.15
Metal 1	0.8
Field oxide	0.68
Polysilicon	0.5

Table 4.1 - Thickness of various layers of NT's CMOS3 DLM integrated circuit fabrication process.

Figure 4.1 - SEM photograph of the cross-section of a beam-type polysilicon resistor.

photograph was obtained as 0.8 μm. This is about 0.3 μm more than the thickness reported by Northern Telecom for the polysilicon layer. However, the thickness of various layers depends on the fabrication process, and will vary from one fabrication run to another. Since, all the experimentally tested microstructural devices are from the same run as the photographed structure, the thickness of the polysilicon layer is taken as 0.8 μm. The thickness of various other layers obtained from the SEM photograph match, within error, the thickness reported by Northern Telecom.

4.4 Thermal Conductivity of Various Layers

The thermal conductivity of various layers which make up the micromachined microstructures fabricated using NT's CMOS3 DLM process, is discussed below.

Thermal Conductivity of Field Oxide, CVDs and Passivation Layers

The field oxide, CVD 1, CVD 2 and passivation layers are essentially high-purity silicon dioxide layers. K.E. Petersen[7] reports the thermal conductivity of SiO_2 (fibers) as 0.014 W/cm °C, which is the thermal conductivity of bulk high-purity clear fused quartz at 27° C. However, H.A. Schafft, et al[53], report that the thermal conductivity of micrometer-thick films of silicon dioxide is much lower than the values reported for bulk specimens, and decreases with increasing temperatures, and falls with decreasing film thickness. They propose boundary scattering of phonons to be the cause for the reduced thermal conductivity. However, the values reported are dependent on the doping and thickness of the test samples, and not enough data points are provided to successfully extrapolate the thermal conductivity of SiO_2 films of thickness other than the reported test samples. During the fabrication process, the various oxide layers are grown or chemically deposited at very high temperatures. Thermally grown oxide layers, which form the base oxide, closely resemble high-purity clear fused quartz. The CVD layers are grown at lower temperatures than base oxide. For the ease of modeling and lack of relevant data, the thermal conductivity of bulk high-purity clear fused quartz[54] (see Figure 4.2a) is assumed as the thermal conductivity of various silicon dioxide layers of the microstructure. For temperatures from 22° C to 250° C, the thermal conductivity of SiO_2 layers is given by

$$k_{SiO_2}(T) = 1.3509e{-2} + 1.9066e{-5}\,T - 2.800e{-8}\,T^2 \quad \text{Watts/cm °C} \qquad (4.1)$$

where T is the temperature in degree Celsius.

Thermal Conductivity of Polysilicon Layer

The polysilicon layer forms the heater and the sense resistors of the designed microstructures. Unlike the monocrystalline substrate silicon, polysilicon is a large grain silicon. The thermal conductivity of monocrystalline silicon is given by

$$k_{mono}(T) = \frac{299}{T + 174} \text{ Watt/cm °C} \tag{4.2}$$

where T is the temperature in degree Celsius[55].

F. Volklein and H. Baltes[56] report the thermal conductivity of polysilicon films as 0.285 W/cm °C for the temperature range 0° C to 100° C, which is much smaller than the thermal conductivity of monocrystalline silicon. They report that the lower values of thermal conductivity in thin film polysilicon result due to the phonon scattering at grain boundaries. This value of thermal conductivity of polysilicon was used in the modeling of the microstructure, but the results obtained were substantially different from the experimental values. However, this value of thermal conductivity of polysilicon is fabrication process and thickness dependent. Hence, the relationship given by equation 4.2 is used to calculate the thermal conductivity of polysilicon at various temperatures (see Figure 4.2b).

Thermal Conductivity of Metal Layer

The metal layer is an aluminum film with a small percentage of copper, and is assumed to contain silicon to a lesser degree. The thermal conductivity for such samples is given by

$$k_{metal}(T) = 0.83 + \frac{256}{T + 273} \text{ Watt/cm °C} \tag{4.3}$$

where T is the temperature in degree Celsius[57]. This relationship is used to calculate the thermal conductivity of the metal layer at various temperatures (see Figure 4.2b).

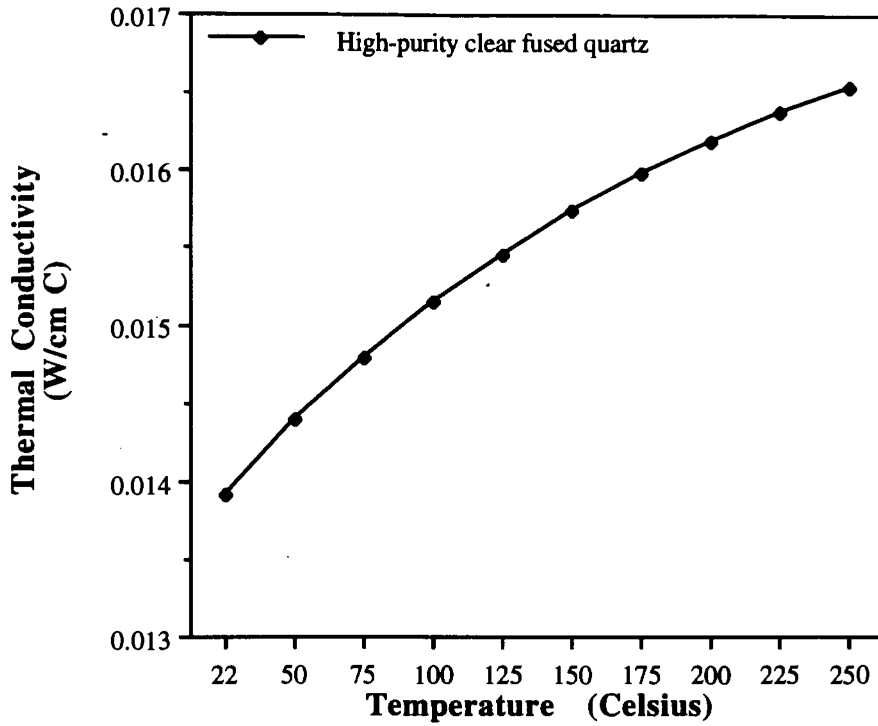

Figure 4.2a - Thermal conductivity of high-purity clear fused quartz, also assumed to be that of SiO_2 layers.

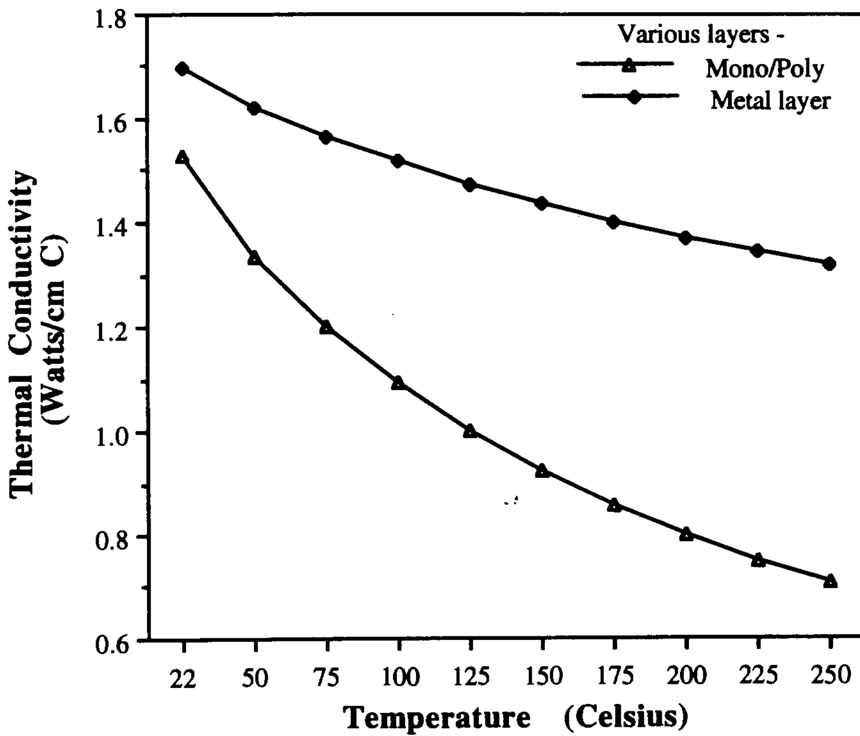

Figure 4.2b - Thermal conductivity of monocrystalline\poly layer and metal layer.

Figure 4.2 - Thermal conductivity of SiO_2, polysilicon and metal layers.

4.5 2-D Modeling using ANSYS

The available limited memory size educational institution version of the finite element ANSYS package was unable to handle the complexity of 3-D modeling of the designed microstructures, therefore an equivalent 2-D model was generated. The following section discusses the procedure and assumption of reducing a 3-D model to a 2-D model by merging the thermal conductivity of various layers as a ratio of their thickness. An example of a simple structure is reported to confirm the procedure.

Consider a beam-type polysilicon heater resistor sandwiched in between two layers of silicon dioxide (see Figure 4.3a). The poly heater is 0.8 μm thick, 1 μm wide and 10 μm long. Each SiO_2 layer is 1 μm thick, 1 μm wide and 10 μm long. For simplicity, the thermal conductivity of the polysilicon and silicon dioxide layer is assumed to be 2.85×10^{-1} W/cm °C and 1.4×10^{-2} W/cm °C at all temperatures, respectively. The two end-faces of the structure are assumed to be pinned at 0° C constant temperature. A power dissipation of 4 mW is assumed in the heater resistor.

A 3-D model of the example structure is created using the ANSYS. The units were consistently used as Watt, micrometer, and degree Celsius. The details of the procedure of creating the model, solving, and postprocessing using ANSYS is described in Appendix C.1 . The power dissipation in the poly layer was input as internal heat generation per unit volume assigned to the elements, termed as QE, of the poly layer. The volume of the poly layer is 8 μm^3, and for 4 mW power dissipation

$$QE_{3D} = \frac{4 \times 10^{-3}}{0.8 \times 1.0 \times 10} = \frac{4 \times 10^{-3}}{8} = 5 \times 10^{-4} \text{ Watts}/\mu m^3 \qquad (4.4)$$

The temperature distribution obtained by ANSYS after post processing is shown in Figure 4.4 . It shows a maximum temperature of 195.941° C at the central part of the structure.

A 2-D equivalent model of the structure is as shown in Figure 4.3b, and was created using ANSYS. However, for 2-D models ANSYS assumes a thickness of 1 μm and the volume of the 2-D structure is now equal to 10 μm^3. Thus, for a heater power

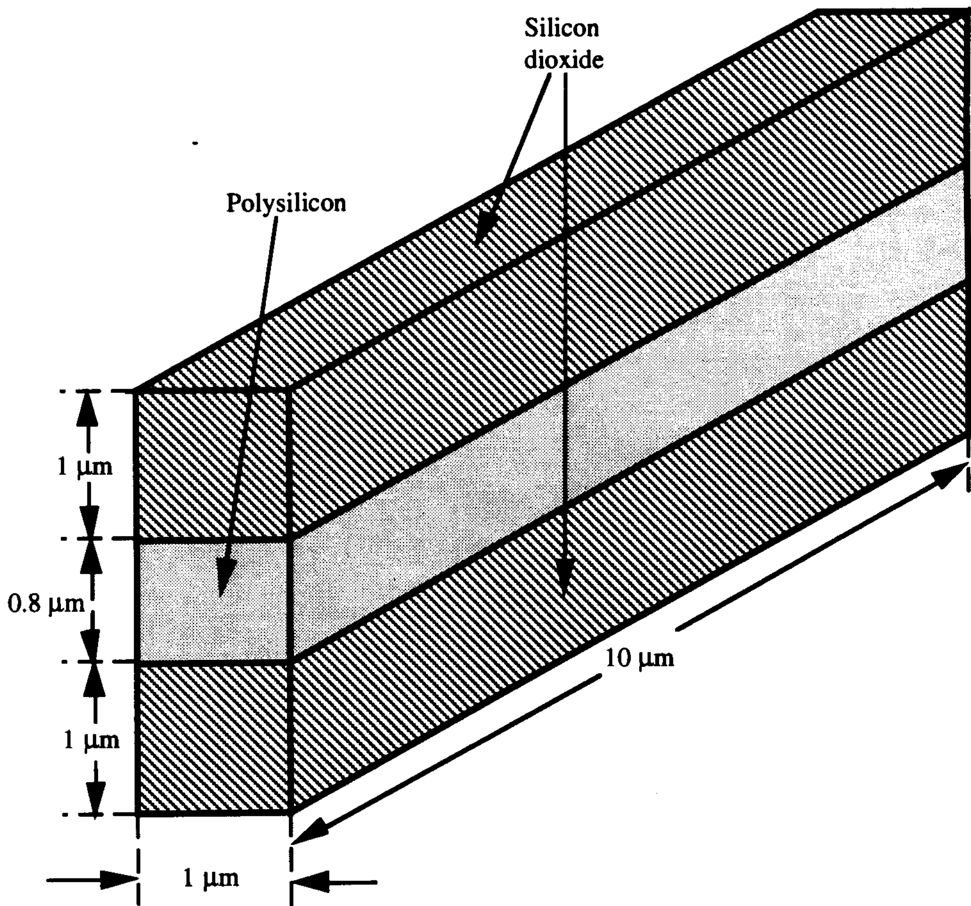

Figure 4.3a - Schematic of the example structure.

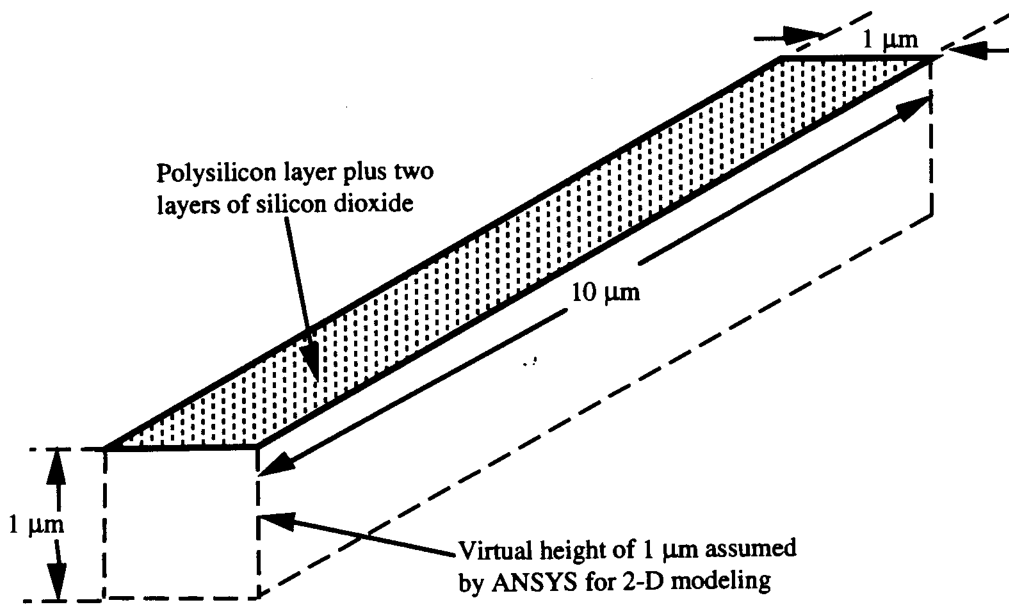

Figure 4.3b - Equivalent 2-D model as perceived by ANSYS.

Figure 4.3 - Equivalent 2-D ANSYS model of the example 3-D structure.

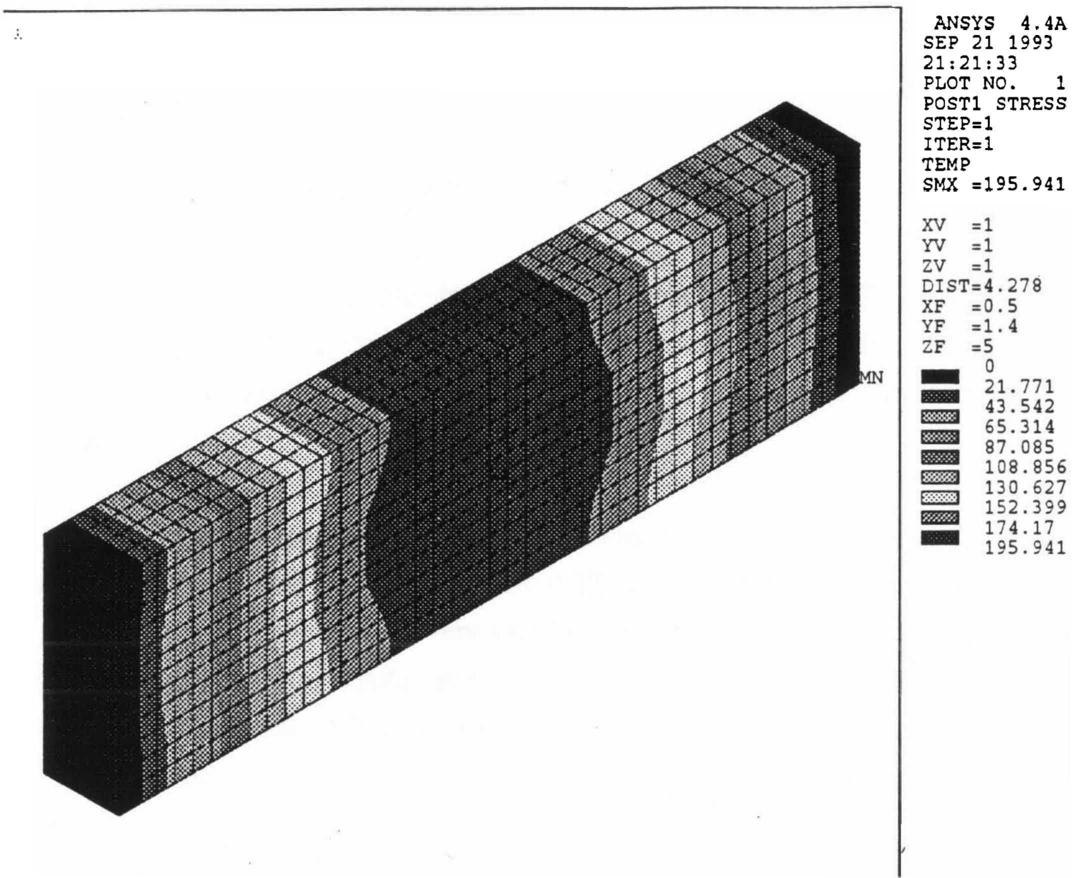

Figure 4.4 - Temperature distribution obtained by ANSYS for 3-D model of the example structure.

dissipation of 4 mW, the internal heat generation per unit volume is equal to

$$QE_{2D} = \frac{4 \times 10^{-3}}{1.0 \times 1.0 \times 10} = \frac{4 \times 10^{-3}}{10} = 4 \times 10^{-4} \text{ Watts}/\mu\text{m}^3 \quad (4.5)$$

Due to the merging of one poly layer and two SiO_2 layers, the equivalent thermal conductivity of one layer of the 2-D structure is the sum of the product of thermal conductivity and thickness of each layer, and is given by

$$TC_{eq} = 0.8 \times 2.85 \times 10^{-5} + 1.0 \times 1.4 \times 10^{-6} + 1.0 \times 1.4 \times 10^{-6} \text{ Watts}/\mu\text{m °C}$$

or,

$$TC_{eq} = 2.56 \times 10^{-5} \text{ Watts}/\mu\text{m °C} \quad (4.6)$$

A 2-D model of the example structure using these values of QE_{2D} and TC_{eq} was created using the ANSYS. Figure 4.5 shows the temperature distribution obtained after post processing. A maximum temperature of 195.313° C is obtained for the central part of the structure.

The maximum temperature obtained by 2-D modeling differs from the maximum temperature obtained by the 3-D modeling by 0.32 percent. In modeling of the designed micromachined structure, this error is very small compared to the uncertainty in the values of the thickness and thermal conductivity of the various layers. Also, the error occurs because the same 2-D model will be applicable to the other two possible arrangements of one poly layer and two SiO_2 layers.

Thus, for thermal analysis using ANSYS, a complex 3-D structure can be reduced to a simple 2-D model without any significant loss of accuracy. This results in reduced complexity of a problem which can then be successfully modeled using the limited capability educational institution version of the ANSYS program available.

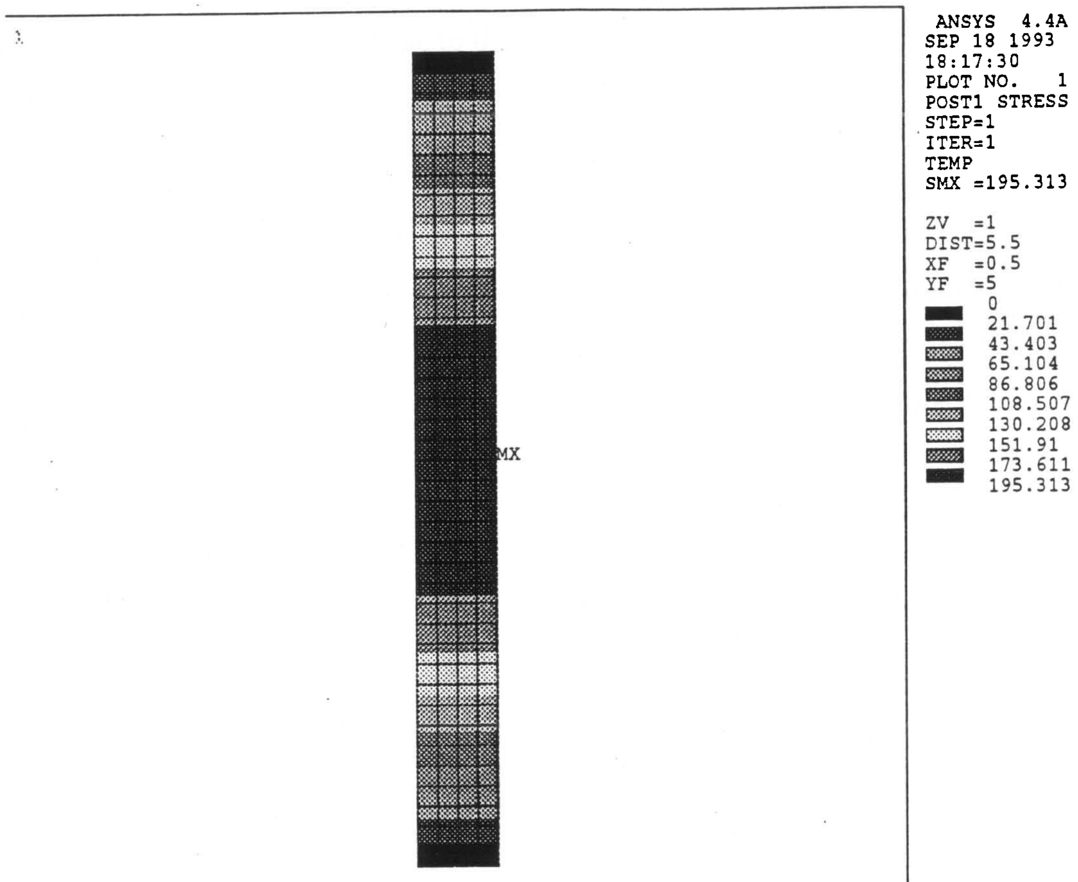

Figure 4.5 - Temperature distribution obtained by ANSYS for 2-D model of the example structure.

4.6 Modeling of 1 Plate Beam-type Poly Resistor Structure

First, for sake of simplicity as discussed earlier in Section 4.2, the modeling of heat distribution in microstructure at high vacuum pressure of 3 x 10^{-7} Torr is done. Any loss of heat to the surrounding gas molecules is neglected and, thus, the heat generated in the heater resistor should be lost only to the silicon substrate through the support arms consisting of metal leads and silicon dioxide layers. Figure 4.6 shows the 2-D model of the structure created using ANSYS. Due to the symmetry of the design, only one-half of the structure was modeled.

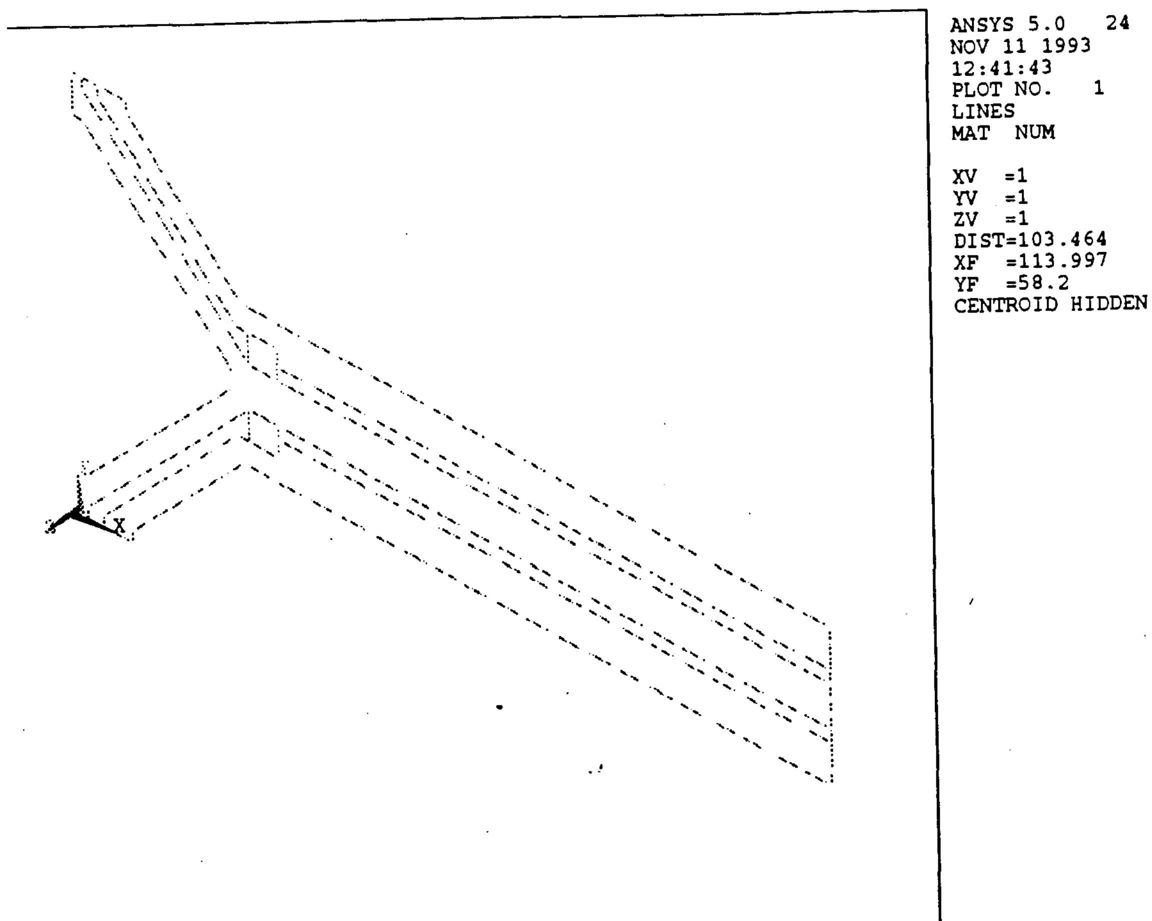

Figure 4.6 - 2-D model of structure 1 plate beam-type polysilicon resistor generated using ANSYS. Due to the symmetry of the design, only one-half of the structure was modeled.

The 2-D model of the structure has four different kinds of material layers (see Figure 4.7a), referred to as Mat 1, Mat 2, Mat 3 and Mat 4. Figure 4.7b show the 3-D composition of the four layers. Mat 1 layer is made up of passivation, CVD 2, CVD 1 and field oxide layers. The thermal conductivity of its equivalent 2-D layer, using the merging criteria discussed in Section 4.5, is given by

$$TC_{Mat1} = \left(t_{Passivation} + t_{CVD_2} + t_{CVD_1} + t_{Fieldoxide}\right) \times k_{SiO_2}(T) \quad \text{Watts}/\mu\text{m °C}$$

or,

$$TC_{Mat1} = 3.98 \times k_{SiO_2}(T) \quad \text{Watts}/\mu\text{m °C} \qquad (4.7)$$

where t is the thickness and $k_{SiO_2}(T)$ is the thermal conductivity of oxide layers given by equation 4.1 .

Mat 2 layer is made up of passivation, CVD 2, Metal 1, CVD 1 and field oxide. The thermal conductivity of its equivalent 2-D layer is given by

$$TC_{Mat2} = \left(t_{Passivation} + t_{CVD_2} + t_{CVD_1} + t_{Fieldoxide}\right) \times k_{SiO_2}(T) + t_{Metal_1} \times k_{metal}(T) \qquad (4.8)$$

or,

$$TC_{Mat2} = 3.98 \times k_{SiO_2}(T) + 0.8 \times k_{metal}(T) \quad \text{Watts}/\mu\text{m °C}$$

where $k_{metal}(T)$ is the thermal conductivity of metal layer given by equation 4.3 .

Mat 3 layer is the contact cut part, and is assumed to be made up of passivation, CVD 2, Metal 1, poly and field oxide. The thermal conductivity of its equivalent 2-D layer is given by

$$TC_{Mat3} = \left(t_{Passivation} + t_{CVD_2} + t_{Field\,oxide}\right) \times k_{SiO_2}(T) + t_{Metal_1} \times k_{metal}(T) + t_{Poly} \times k_{poly}(T)$$

or,

$$TC_{Mat3} = 2.83 \times k_{SiO_2}(T) + 0.8 \times k_{metal}(T) + 0.8 \times k_{poly}(T) \quad \text{Watts}/\mu\text{m °C} \qquad (4.9)$$

where $k_{poly}(T)$ is the thermal conductivity of polysilicon layer given by equation 4.2 .

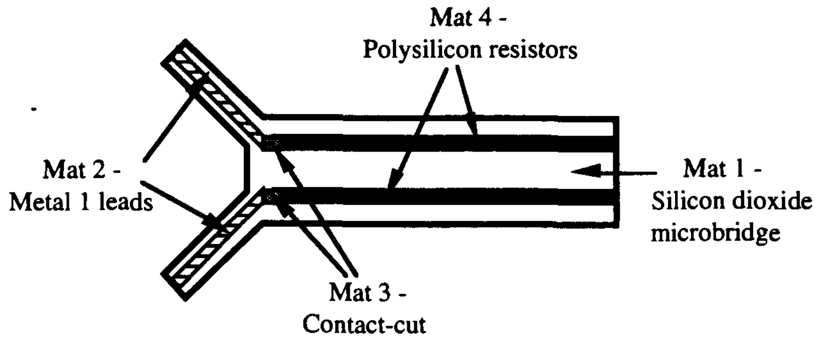

Figure 4.7a - The four different kinds of material layers constituting the 2-D model of the structure 1 plate beam-type poly resistor.

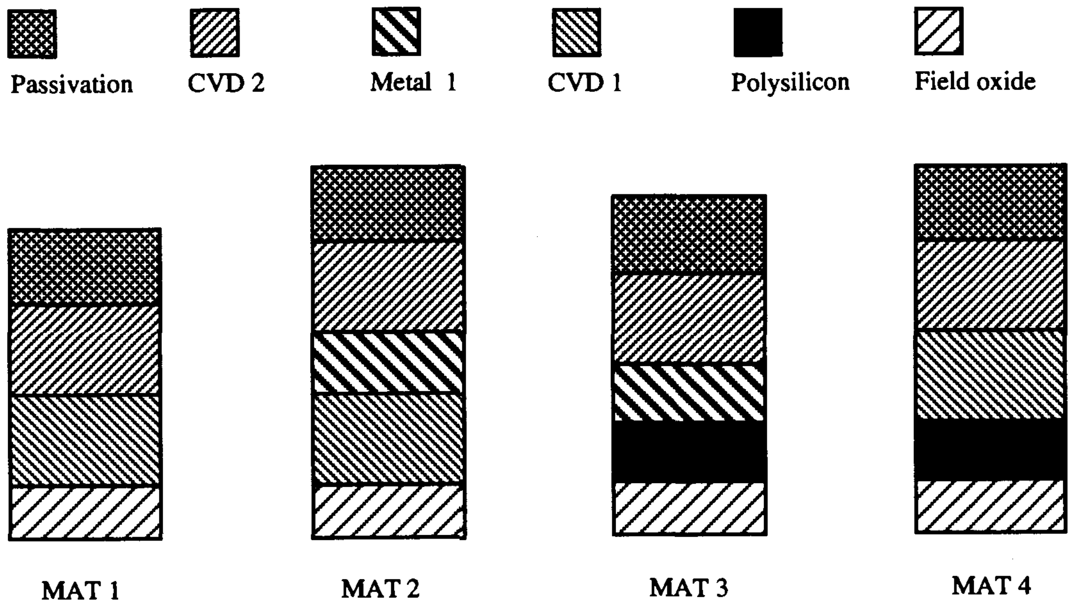

Figure 4.7b - Composition of the four material layers.

Figure 4.7 - Material layers and their composition for the structure 1 plate beam-type poly resistor.

Mat 4 layer is made up of passivation, CVD 2, CVD 1, poly and field oxide. The thermal conductivity of its equivalent 2-D layer is given by

$$TC_{Mat\,4} = \left(t_{Passivation} + t_{CVD_2} + t_{CVD_1} + t_{Fieldoxide}\right) \times k_{SiO_2}(T) + t_{Metal_1} \times k_{poly}(T) \tag{4.10}$$

or,

$$TC_{Mat\,4} = 3.98 \times k_{SiO_2}(T) + 0.8 \times k_{poly}(T) \text{ Watts/}\mu\text{m °C}$$

The power dissipation in the heater resistor is used as internal heat generation per unit volume specified to the elements, termed as QE, constituting the heater poly layer. For 2-D structures ANSYS assumes a virtual thickness of 1 unit. Thus, the volume of heater poly resistor is 1200.96 μm^3. For a power dissipation of 5.67×10^{-4} W, the QE load input is equal to

$$QE_{input} = \frac{5.67 \times 10^{-4}}{1200.96} = 4.72 \times 10^{-7} \text{ Watts/}\mu\text{m}^3 \tag{4.11}$$

The end points, or nodes, of the support arms connecting to the substrate silicon are pinned at 22° C, the room temperature at which the experiments were performed. A non-linear steady-state analysis is performed, and Appendix C.2 show the input listing. After postprocessing, the temperature distribution is obtained as shown in Figure 4.8 . To calculate the average change in temperature of the sense resistor, the nodal temperatures of all the elements constituting the sense resistor were extracted and the average value was calculated. For 5.67×10^{-4} W of heater power dissipation an average temperature change of 71.95° C was obtained for the sense resistor. Figure 4.9 compares the experimental and modeling values of the average change in temperature of the sense resistor to the change in heater power dissipation at 3×10^{-7} Torr. A deviation is noted for sense temperature detection of less than 0.1° C. As indicated from various other experimental results, it is due to saturation in the measured output of the device, and is analyzed in more detail in Chapter 5.

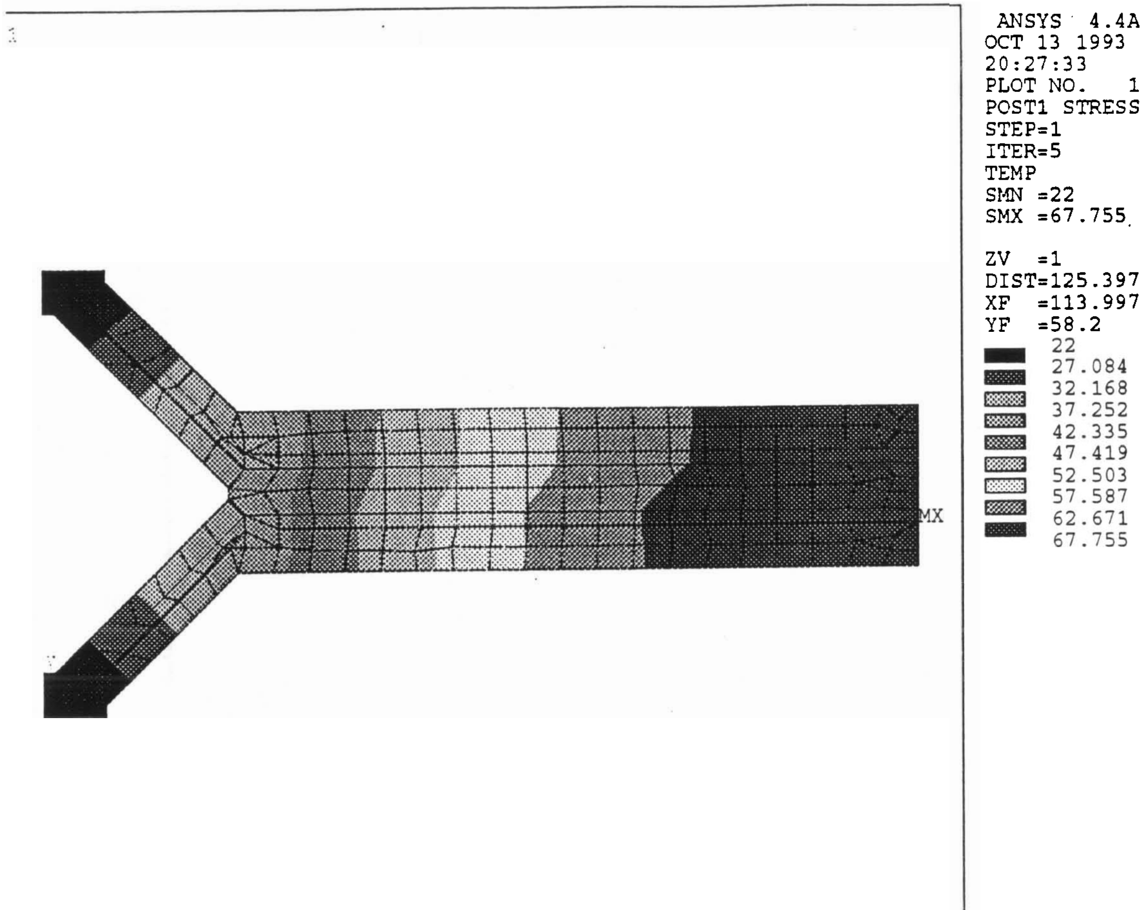

Figure 4.8 - Temperature distribution across the surface of structure 1 plate beam-type polysilicon resistor at 3 x 10^{-7} Torr. (For heater power dissipation of 5.67 x 10^{-4} W)

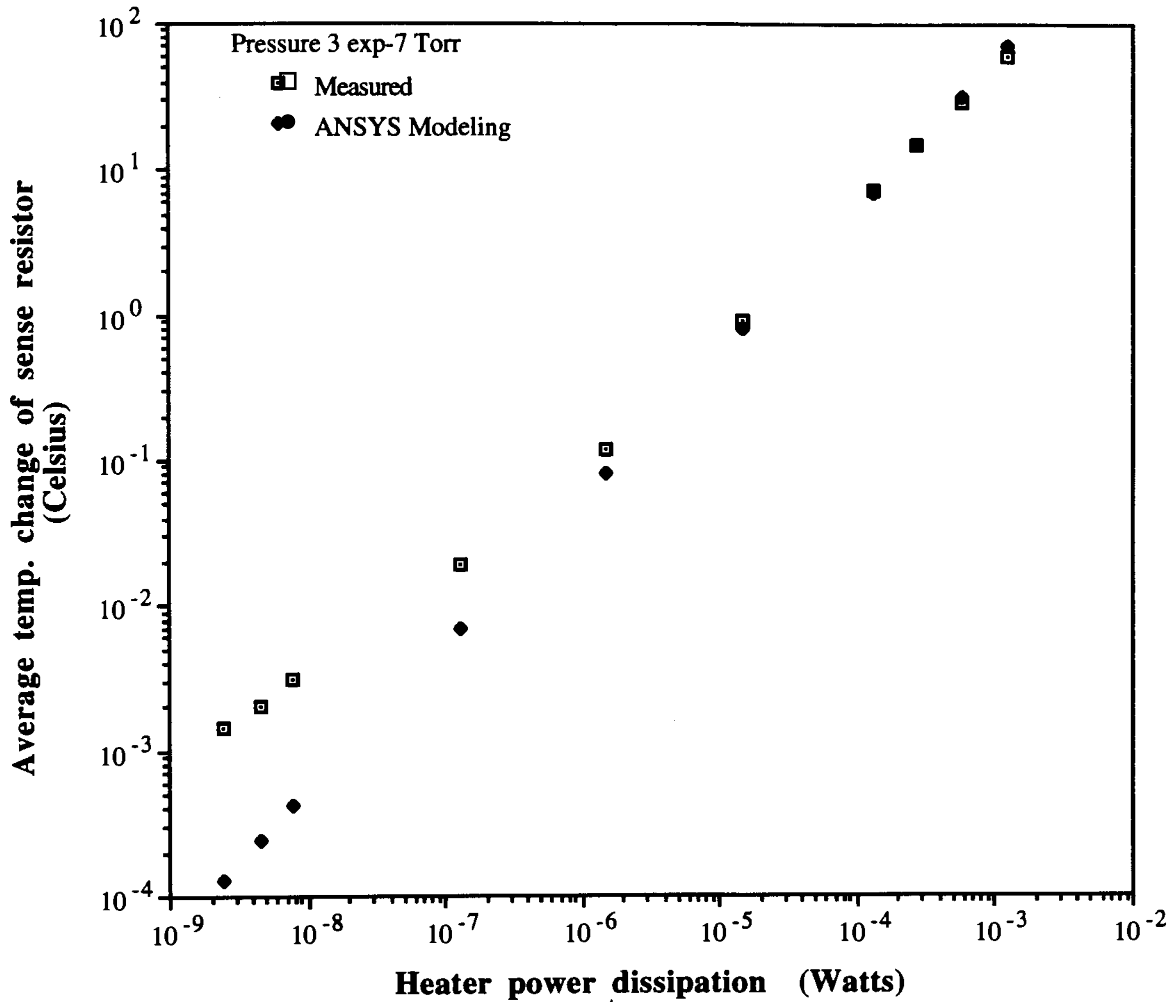

Figure 4.9 - Comparison of experimental and modeling values of average temperature change of sense resistor at 3 x 10^{-7} Torr for the structure 1 plate beam-type poly resistor.

For modeling the heat transfer at room pressure in nitrogen atmosphere, additions are required to incorporate the heat loss to the gas molecules present in the vicinity. An additional set of nodes, symmetrical to the existing nodes of the model but displaced by 20 μm in the z-direction, was generated and these nodes were pinned at room temperature of 22° C. A set of 3-D conduction bar elements, STIF33, was generated between the existing nodes of the surface of the 2-D model and the additional nodes created (see Figure 4.10).

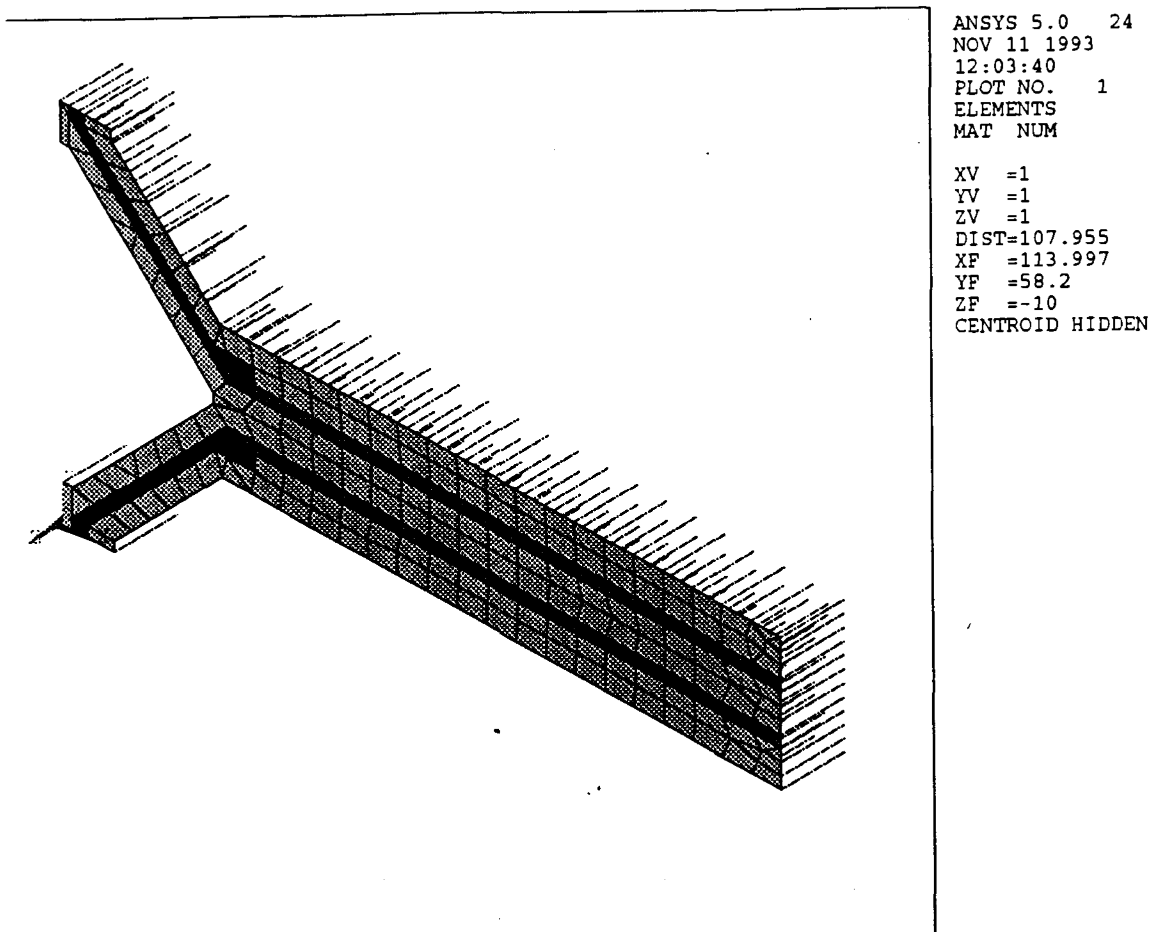

Figure 4.10 - Model of structure 1 plate beam-type poly resistor, showing 3-D conduction elements, used for simulation of heat transfer at room pressure.

Thus, a 2-D model was now converted to a 3-D model. The thermal conductivity of the element was specified as that of nitrogen gas at room pressure[58]. Although the depth of the etched cavity is about 50 µm, the length of the conduction bar elements had to adjusted to 20 µm to take into account the heat loss to the gas molecules at the top surface of the microbridge, as well as silicon substrate under the microbridge and the side walls of the cavity. The heat loss to the substrate and cavity walls have been reported for similar micromachined structures used as gas flow sensors[59]. It is essential to take into account these heat losses while modeling the heat flow at high pressure. The length of the conduction bar elements was the single parameter varied in order to obtain comparable modeling results. Figure 4.11 shows the temperature distribution obtained for 5.67×10^{-4} W of heater power dissipation.

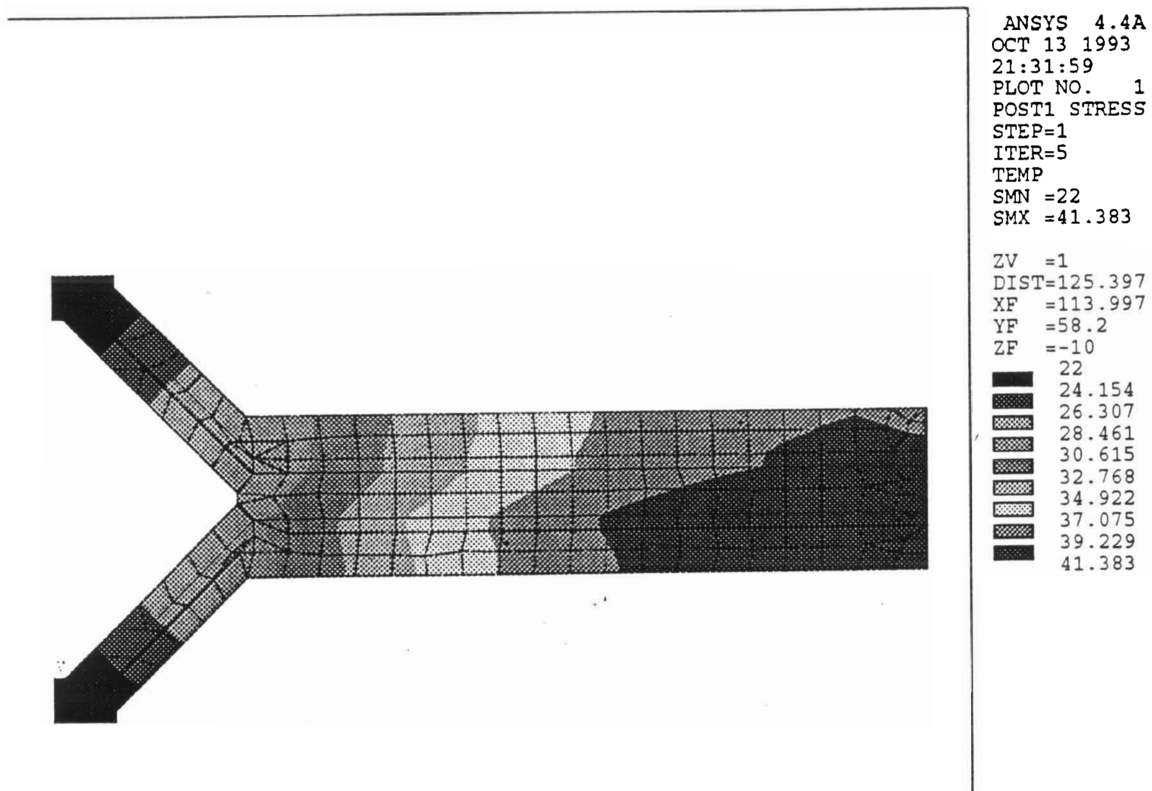

Figure 4.11 - Temperature distribution across the surface of structure 1 plate beam-type poly resistor at 700 Torr. (For heater power dissipation of 5.67×10^{-4} W)

Figure 4.12 compares the experimental and modeling values of the average change in temperature of the sense resistor to the change in heater power dissipation at room pressure. A deviation is again noted for sense temperature detection of less than 0.1° C. As discussed earlier, it is caused by the saturation in the measured output of the device, and is analyzed in more detail in Chapter 5.

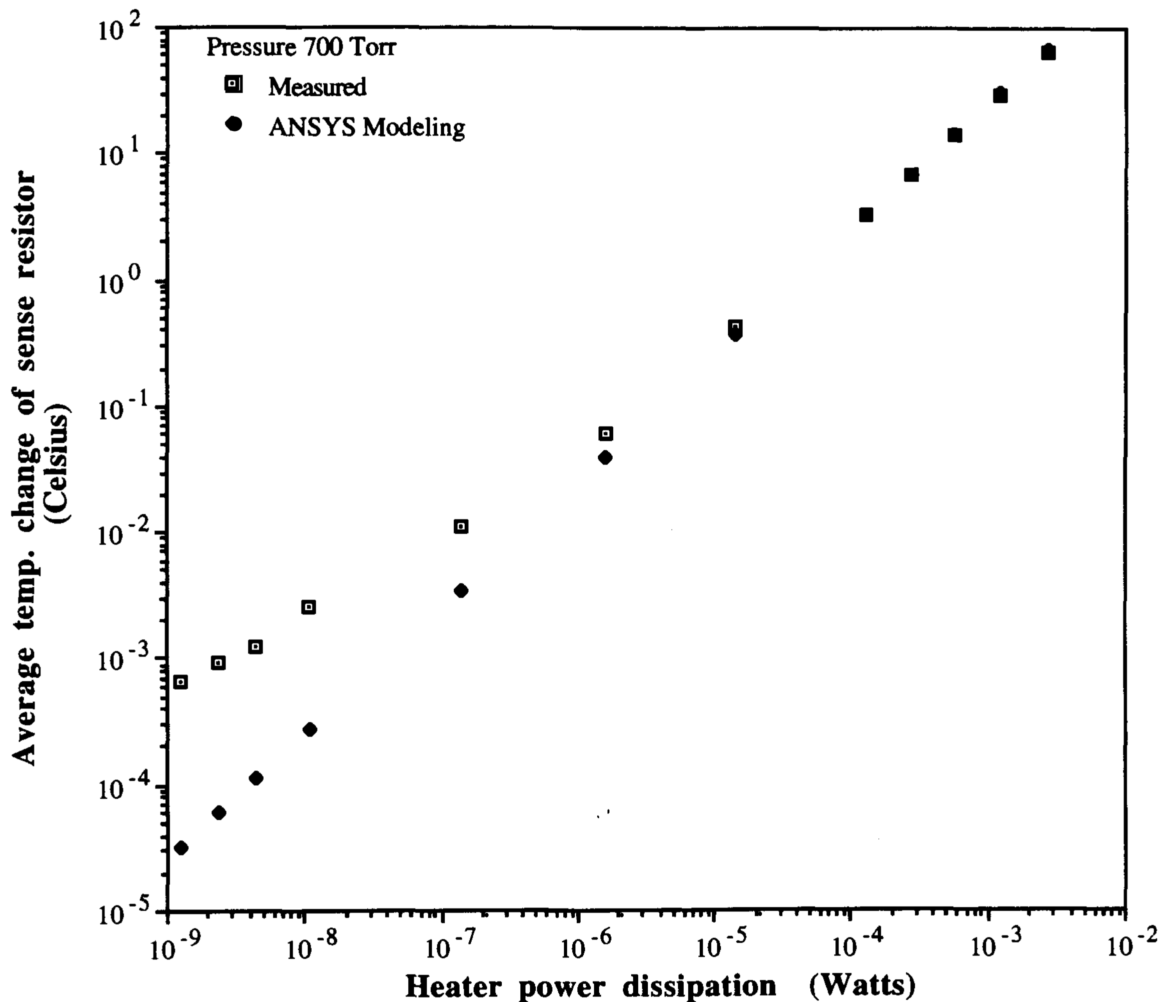

Figure 4.12 - Comparison of experimental and modeling values of average temperature change of sense resistor at 700 Torr for the structure 1 plate beam-type poly resistor.

4.7 Modeling of 3 Plate Beam-type Poly Resistor Structure

The modeling of the structure 3 plate beam-type polysilicon resistor was done at room pressure in nitrogen gas atmosphere. The coordinate values representing the structure were input in the preprocessing step of the ANSYS program, and STIF33 3-D conduction elements were generated to account for the heat loss to the silicon substrate under the microbridge, as well as the side walls of the cavity and gas molecules at the top surface of the microbridge. The input values of the thickness and thermal conductivity of the various layers are the same as those used in the modeling of the 1 plate beam-type polysilicon resistor structure (see Section 4.6). Appendix C.3 lists the input to the ANSYS required for the modeling of this structure. In order to obtain comparable results, the length of the 3-D conduction elements was varied, and best results were obtained for element length of 30 μm. When compared to the modeling of the structure 1 plate beam-type polysilicon resistor, this variation in the length of 3-D conduction elements can be attributed to a different cavity and structure size. Figure 4.13 shows the 2-D model of the 3 plate beam-type poly resistor structure generated by ANSYS. Figure 4.14 compares the experimental and modeling values of the average change in temperature of the sense resistor to change in heater power dissipation at room pressure. A similar deviation of the experimentally estimated values of the average temperature change of the sense resistor is noted from the modeling result, and is discussed in detail in Chapter 5.

4.8 Summary

The modeling results for the two structures, 1 plate beam-type poly resistor and 3 plate beam-type poly resistor, indicate a good correspondence to the experimental measured values for heater power dissipation higher than 10^{-5} W, where average temperature change of more than 0.1° C is detected. For lower heater power dissipation, a divergence is noted, with modeling results differing from the experimental estimated values by an approximate factor of 10 for the lowest detected average temperature change of the sense resistor. This confirms the saturation observed in the output of the device as noted earlier. However, the modeling does indicate that temperature change of less than 0.5 millidegree Celsius can be detected at the sense resistor. The next chapter discusses the analysis of the various experimental and modeling results, including saturation in the output of the device.

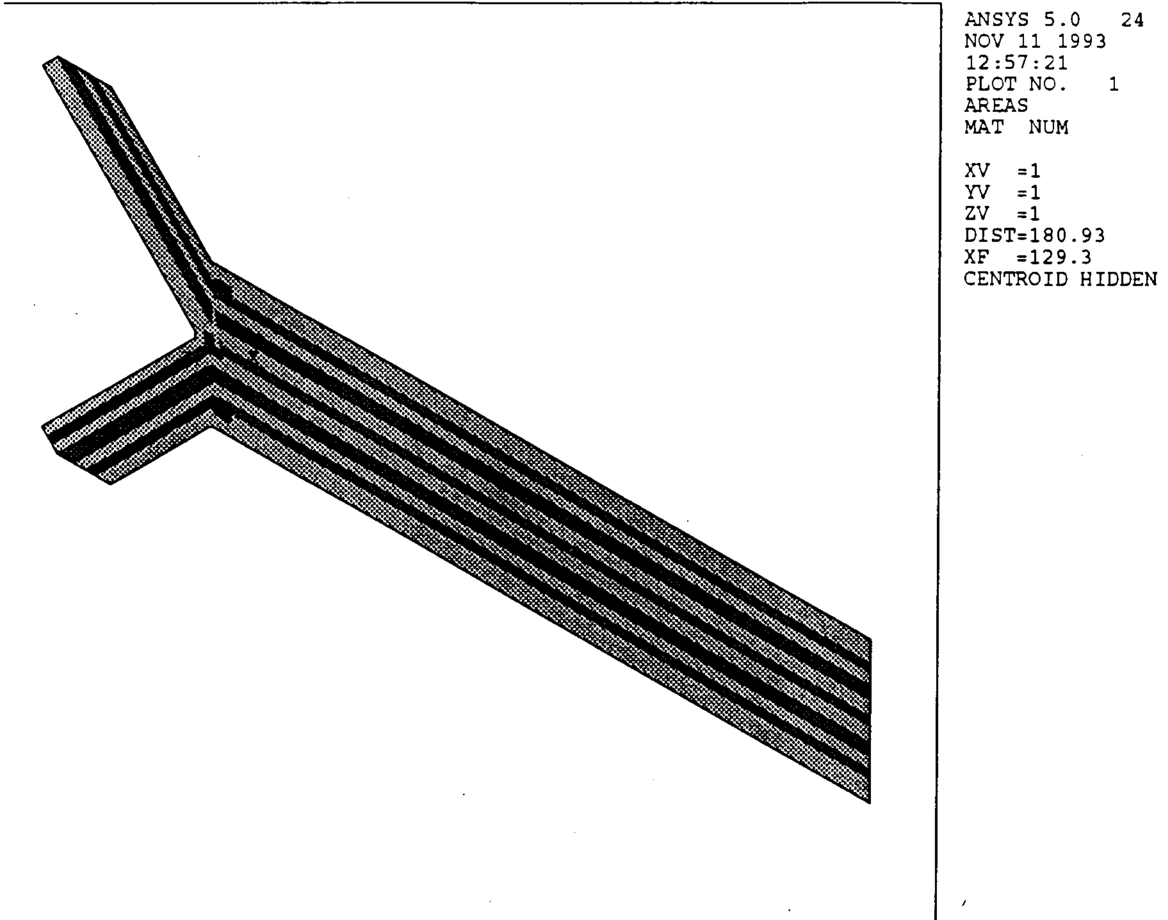

Figure 4.13 - Top view of the ANSYS model of structure 3 plate beam-type poly resistor.

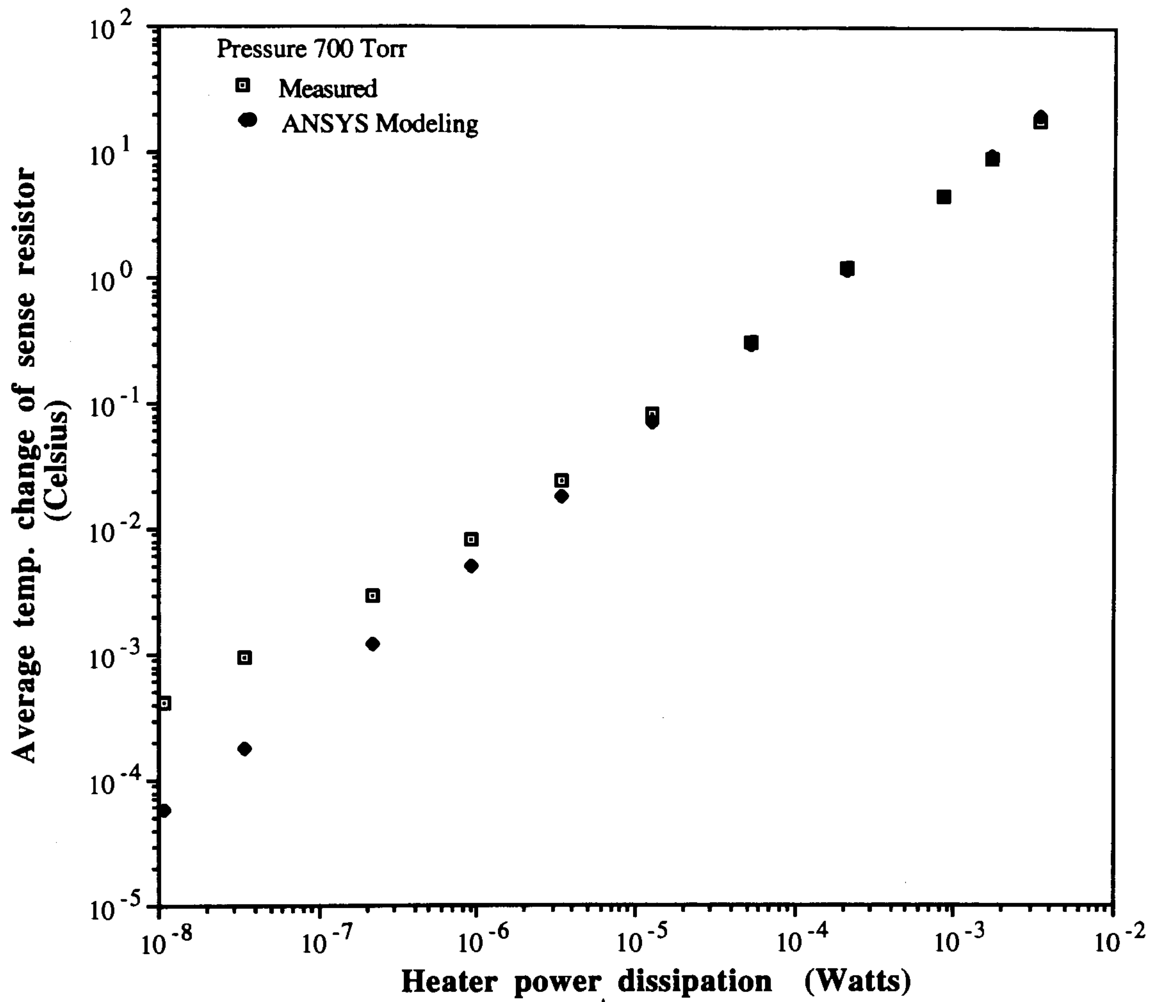

Figure 4.14 - Comparison of experimental and modeling values of average temperature change of sense resistor at 700 Torr for the structure 3 plate beam-type poly resistor.

5 Analysis and Future Work

Experimental and modeling results indicate that temperature change of less than 0.5 millidegree Celsius can be detected at the sense resistor by the application of phase-sensitive detection technique to the designed silicon microstructure. However, various experimental results, and comparisons with ANSYS modeling results (see Figure 4.12), indicate a deviation and saturation of the measured output. This chapter reports the analyses of the various results, and investigates the reasons for saturation of the output of the device. Proposed future work is also discussed.

5.1 Saturation of the Output

Ideally, the output voltage and estimated average temperature change of the sense resistor should be proportional to the heater power dissipation at a constant pressure. However, at constant pressure of 700 Torr, the device output shows a linear behavior for heater power dissipation greater than 10^{-6} W when output voltages of more than 1 μV (corresponding to estimated average temperature changes of more than 10^{-2} °C) are measured (see Figure 3.9). For heater power dissipation of less than 10^{-6} W, when the output voltages of less than 1 μV are measured (corresponding to estimated average temperature changes of less than 10^{-2} °C), a saturation in the output of the device is indicated as the measured output voltage start deviating from the weighted error line-fit. Also, for the operation of the designed microstructure as a vacuum sensor, the output and the estimated average temperature change of the sense resistor do not decrease by the same magnitude as the density of molecules in the vacuum chamber below 10^{-2} Torr (see Figures 3.14 and 3.16). The output of the device for constant heater temperature operation at 75° C and 40° C saturates at approximately 1 μV, which corresponds to estimated average

temperature change of 10^{-2} °C (see Figures 3.15 and 3.17). This is at least 15 times higher than the capability to measure less than 0.5 millidegree Celsius temperature change of the sense resistor (see Figures 3.9 and 3.10). This too indicates a saturation in the output voltage measurement of 1 μV, or below 10^{-2} °C temperature change of the sense resistor. Some of the factors which might cause the saturation in the measured output of the device are discussed.

5.2 Radiative Heat Transfer

Radiative heat transfer at low pressure, which is responsible for the saturation of the output of other vacuum gauges, might be responsible for the saturation of output of this device. Radiative heat transfer is highly dependent on the heater temperature, a T^4 Stefan-Boltzmann relationship (see Equation 2.1), and would have been expected to produce an earlier saturation in the case of high heater temperature excitation of 200° C when compared to 40° C excitation by a factor of at least

$$\frac{q_{200}}{q_{40}} = \frac{\sigma A \varepsilon \left(T_{200}^4 - T_{22}^4\right)}{\sigma A \varepsilon \left(T_{40}^4 - T_{22}^4\right)} = \left(\frac{473^4 - 295^4}{314^4 - 295^4}\right) \approx 20 \qquad (5.1)$$

where, q is the heat transfer, A is the facing area, ε is the emissivity, and σ is the Stefan-Boltzmann constant. However, the device shows similar response at low pressure for constant heater excitation of 200° C and 40° C (see Figures 3.15 and 3.17). Hence, radiative effect is not causing the saturation of the output of the device.

5.3 Crosstalk

The lock-in eliminates the asynchronous noise; the possibility of synchronous noise pick-up from external sources, and crosstalk between the heater driving signal and the measured signal was recognized. Efforts were made to minimize the noise by using coaxial cables, differential voltage connection, proper shielding and use of a common ground. Measurements were done to find out the degree of interference and crosstalk still occurring. Figure 5.1 shows the circuit setup, in which the sense resistor arm is short-circuited. Thus, no sensing DC signal flows through the sense resistor, and only extraneous synchronous signals are measured by the lock-in at the 1 KΩ R_{ss} resistor. The heater side

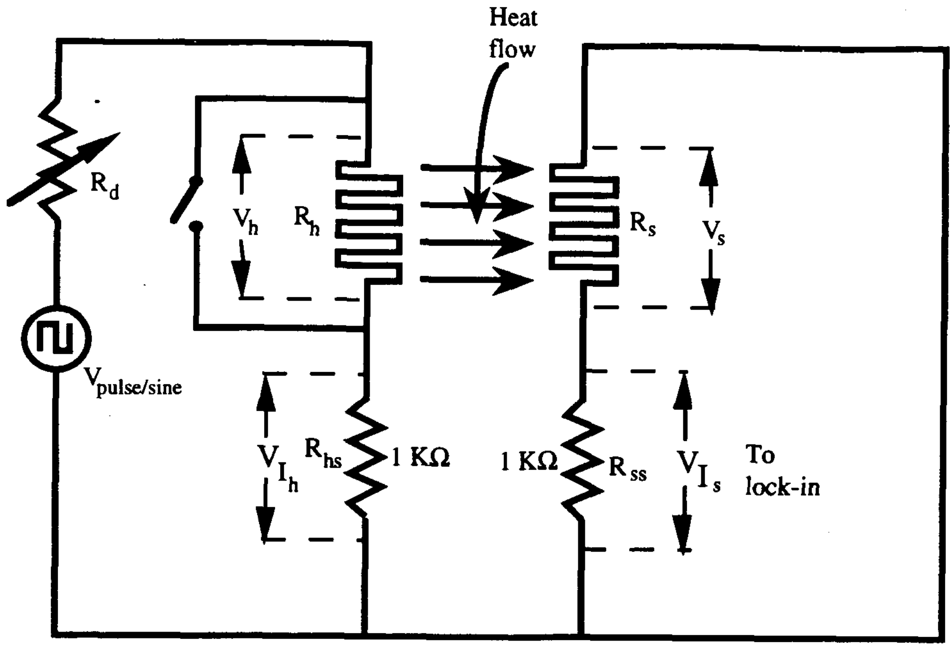

Figure 5.1 - Circuit setup to measure crosstalk.

Heater current	Heater power dissipation	Square-pulse		Sine-wave	
		Heater resistor not shorted (Volts)	Heater resistor shorted (Volts)	Heater resistor not shorted (Volts)	Heater resistor shorted (Volts)
420 μA	0.5 mW	8.01e-6	1.23e-7	6.28e-6	9.45e-8
330 μA	0.3 mW	5.80e-6	8.37e-8	4.52e-6	7.38e-8
270 μA	0.2 mW	4.96e-6	7.42e-8	3.88e-6	6.01e-8
180 μA	97 μW	3.16e-6	6.38e-8	2.47e-6	5.18e-8
20 μA	1.2 μW	3.32e-7	8.07e-9	2.59e-7	5.82e-9
10 μA	0.3 μW	1.71e-7	6.96e-9	1.38e-7	3.68e-9

Table 5.1 - Crosstalk measurements.

was then excited by square-pulse, and DC offseted sine-wave, for various peak currents. The measurements were then made by the lock-in amplifier at the sense load-resistor. Another set of values was measured after short-circuiting the heater resistor. The output of the lock-in amplifier is summarized in Table 5.1 .

For a heater current of 0.42 mA, the heater power dissipated is 0.5 mW, and the output voltage measured is 8.0 μV compared to 200 μV measured with the sensing signal through the sense resistor (see Figure 3.9). This implies noise interference of about 4%. For a heater current of 20 μA, the heater power dissipated is 1.2 μW, and the output voltage is 0.8 μV measured with the sensing signal through the sense resistor (see Figure 3.9). The estimated average temperature change of the sense resistor at this output voltage is 10^{-2} °C, and is the saturating limit for most of the measurements. However, for 20 μA heater current the output voltage measured with no sensing signal is 0.32 μV, and amounts to interference noise of about 40%. The percentage amount of interference increases drastically as lower than 1 μV output signals (corresponding to lower than 10^{-2} °C temperature changes) are measured, and thus becomes the dominating factor and saturates the device output.

The data in Table 5.1, which was obtained with the heater resistor shorted and no signal entering the chip, indicates a significant fraction of crosstalk occurs at the circuit board components, wires and connections. However, a higher crosstalk result when the heater resistor is not shorted indicating an on-chip crosstalk component. Note that both square-wave and sine-wave excitations generate about the same degree of crosstalk. The crosstalk signal level is also dependent on the geometry of the measurement setup.

The crosstalk voltages of Table 5.1 are comparable to the saturation limit seen in the output of device as reported in Chapters 3 and 4. Thus, in Figure 3.12, for constant heater voltage operation at 1.7 V, the lock-in output saturates at 3 μV which is comparable to 8 μV crosstalk voltage for about the same current magnitude of 420 μA. In Figure 3.14, for constant heater temperature operation at 200° C, the lock-in output saturates at 3 μV which is comparable to 6 μV crosstalk voltage for similar 330 μA current. In Figure 4.14, where ANSYS modeling values are compared with experimental values at various heater power dissipation, for 10^{-6} W heater power dissipation (corresponding to 20 μA current), the difference between the estimated and modeling value is 5 millidegree Celsius which corresponds to a voltage of 0.37 μV (see also Figure 3.9). This compares closely with the 0.33 μV crosstalk voltage measured for 20 μA current.

These examples clearly indicate that a significant portion of saturation of the output of the device is due to crosstalk, and can be minimized in future designs.

5.4 Electromagnetic Induction

Since a square-pulse was used to excite the heater resistor, there is a possibility that a voltage is induced in the sense circuit due to the approximate 5 μsec rise-time of the current pulse (see Figure 5.2), and that might cause the saturation of the output. Assuming the conductors to be circular, the voltage induced by a long conductor with time-varying current flowing through it, in another conductor parallel to it is given by

$$V_{induced} = \frac{\mu_o}{2\pi r}\frac{\Delta I_1}{\Delta t}LW \qquad (5.2)$$

where μ_o is the permeability constant, r is the separation between the two conductors,

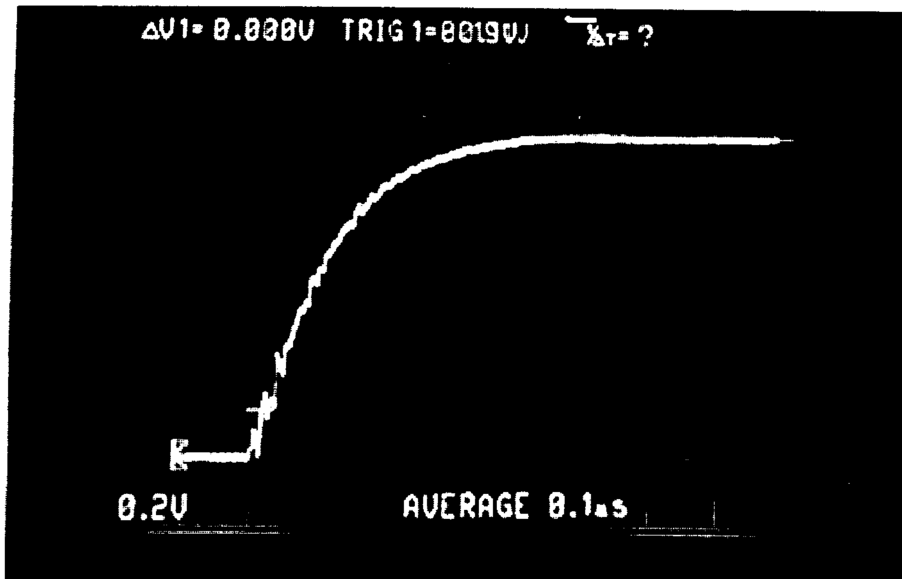

Figure 5.2 - Rise time of heater current.

t is the time, L is the length and W is the width of the conductor in which the voltage is induced[60].

The sense resistor is approximately 700 μm long, 3.6 μm wide and is separated from the heater by 25 μm. Thus, for a heater current of 1 mA, the voltage induced is about 4 nV. This is negligible compared to the measured output voltage of 1.4 mV. Similarly, for low heater current of 20 μA, when the saturation becomes noticeable, the voltage induced in the sensor is approximately 0.08 nV. This is again negligible compared to the measured output voltage of 1.0 μV. Also, slowly varying sine-wave excitation of the heater shows the same behavior as that of square-wave (see Table 5.1), and thus, saturation due to induction is ruled out. The comparison of output obtained by the square-pulse and sine-wave excitation also indicates the nature of interference as crosstalk, rather than induction, in the measurement circuit setup.

5.5 Outgassing

There is a possibility of an outgassing phenomenon occurring at the device surface at low pressure. Silicon dioxide layers which make up the device are highly porous and might adsorb gaseous molecules. Adsorbed molecules are released from the surface at low pressure, forming a local high pressure area which might cause the rise or saturation in the output of the device. Conventional ionization gauges have to be degassed every time they are exposed to high pressure in order to give accurate pressure readings. Degassing is the process of removal of adsorbed gases by heating the gauge at high temperatures of 1000° C. To perform a similar degassing procedure on the designed vacuum sensor, a high wattage ceramic resistor was attached underneath a ceramic DIP 24-pin package containing an IC with a sample vacuum sensor device to heat the chip to investigate the effect of degassing on the sensor readings. Similar to the degassing of the ionization gauge, the vacuum chamber was pumped down to 10^{-6} Torr, and a current was injected in the ceramic heating resistor to heat the device at approximately 100° C. Figure 5.3 compares the average change in the temperature of the sense resistor before, and after the degassing, for constant temperature operation of the heater resistor. As it can be seen there is no significant difference in the sensor readings after degassing at 100° C. However, degassing does require heating at higher temperatures such as in the ionization gauge, and this experiment might not reveal the true effect of degassing.

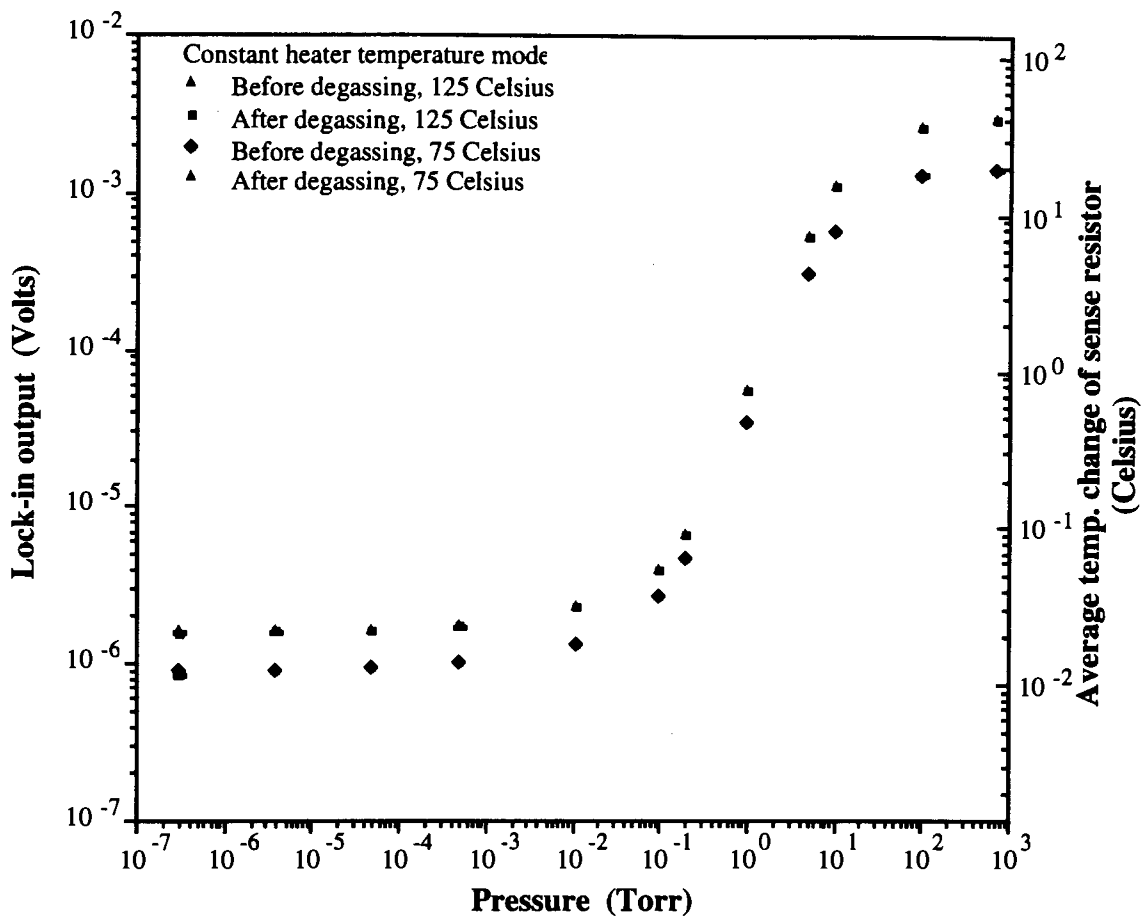

Figure 5.3 - Comparison of output voltage measured, and estimated average temperature change of the sense resistor, before and after degassing of a sample device at 100° C. (For constant heater temperature operation at 125° C and 75° C).

5.6 Future Work

More investigations are required to understand the saturation in the output of the device. A more carefully built measuring circuit setup, including triaxial cable to incorporate ground and earth, to reduce interference and cross-talk is suggested. To reduce interference and crosstalk at the chip level, designs with ground-lines placed in between the signal lines, and a ground-plane over the signal lines can be implemented.

Improvements in the design of the vacuum sensor can be made by designing structures which do not allow bending of the side-microbridges. This should result in the same separation between the heater and the sense resistor for all the fabricated structures. Further improvements can also be made by back etching the silicon substrate and opening the cavity (see Figure 5.4). This would result in less thermal loss to the silicon substrate below the suspended microbridges, and more surface area of the microbridges would be exposed to the vacuum chamber. Sensitivity of the designed vacuum sensor can be further enhanced by increasing the facing area between the heater and the sense resistor by realizing a set up similar to Figure 2.5 . The use of a material with higher TCR for the sense resistor would enhance the sensitivity, but would result in the loss of CMOS compatibility.

A square-pulse signal is used for the time-varying excitation of the heater in the reported set of experiments. However, the response of the device to other time-varying signals such as DC offseted sine-wave, triangular-wave, ramp, or others can also be explored. On the sensor side, instead of using a sensing signal of 0.2 mA current, application of time-varying signals and observing the frequency modulation caused by the heater time-varying signal can be investigated.

The response of the vacuum sensor to various other gases can be investigated. Since the device can note temperature changes of less than 0.5 millidegree Celsius, it's operation as a flow sensor can be investigated.

Also to be explored are various ways of integrating the required signal processing circuitry for phase-sensitive detection with the sensor device on a single chip that allow to replace the DSP lock-in amplifier used in the experiments. The low frequency used in the measurement technique should result in modest digital signal processing requirements to emulate the lock-in function.

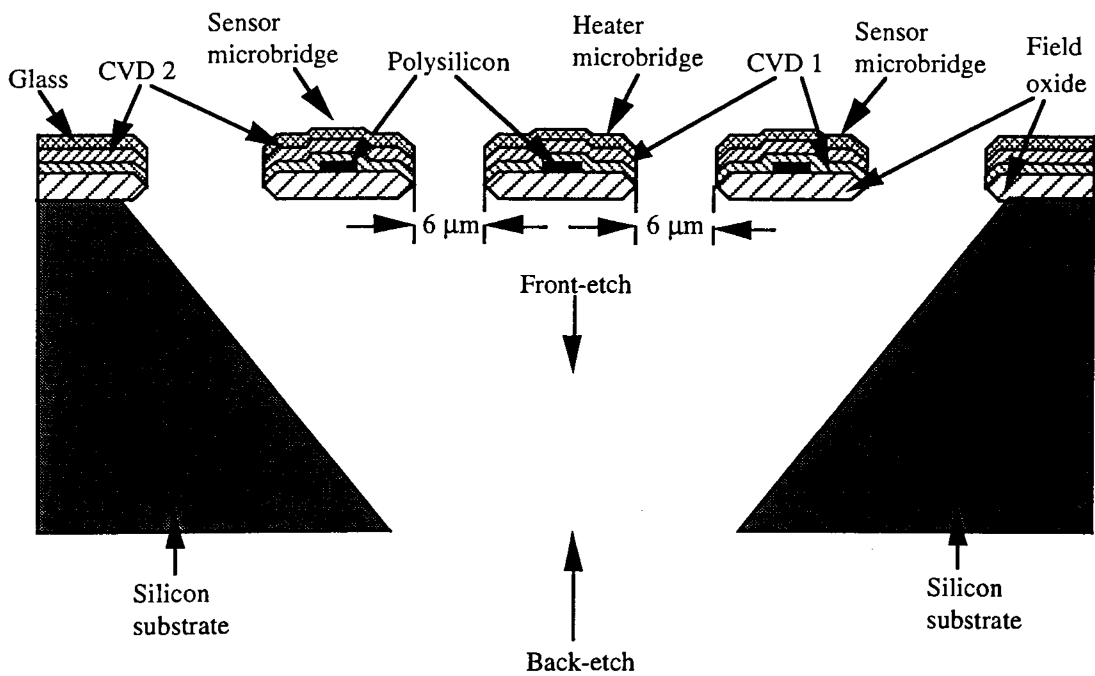

Figure 5.4 - Proposed improvement in design by back-etching the silicon substrate to open the cavity.

6 Conclusion

A micromachined CMOS-compatible wide-range vacuum sensor has been developed. It employs a novel design in which microbridges separated by a 6 μm gap are thermally isolated over a cavity. Unlike existing silicon micromachined vacuum sensors which measure change in the heater temperature with pressure, heat flow by molecules across a 6 μm gap to a sense resistor is detected. AC measurement technique of phase-sensitive detection was successfully employed to measure the heat flow in the designed vacuum sensor, thus laying the foundation for employing this measurement technique to other applications of silicon microstructures. Phase-sensitive detection technique has been shown to be highly sensitive, being capable of detecting induced temperature changes of less than 0.5 millidegree Celsius. The operation of the designed vacuum sensor was explored for constant heater voltage and the sense response was found to saturate below 10^{-2} Torr. The constant voltage excitation resulted in a variation of the heater temperature as pressure varied from 760 Torr to 10^{-2} Torr. This suggested the excitation of heater resistor at a constant temperature. Output voltage was then measured for various constant heater temperature excitations, and the estimated average temperature change of the sense resistor was calculated. However, below 10^{-2} Torr the heat transfer from the heater resistor to the sense resistor does not decrease in the same proportion as the density of molecule in the vacuum chamber. Crosstalk is shown to cause most of the saturation of the output. Further investigations are required to minimize this saturation in the output. Finite-element modeling of heat transfer from the heater resistor to the sense resistor of the designed microstructure was done using ANSYS. The modeling results confirmed that average temperature change of less than 0.5 millidegree Celsius at the sense resistor can be detected. The vacuum sensor has maximum sensitivity from 100 Torr to 10^{-2} Torr. It has extended range from 100 Torr to 760 Torr, and from 10^{-2} Torr to below 10^{-4} Torr at lower sensitivity. With improved circuit designs that eliminate the crosstalk, it is expected that considerably low pressures can be measured due to a reduction in the saturation of the output signal.

Appendix

Appendix A - CDL Program

C Design Language program to generate the structure 3 plate beam-type polysilicon resistor:

```
#ifdef JLS
#define FUTURE
#endif

#include <scdl.h>
#include <stdio.h>
#include <math.h>

#define Xpad        0       /* centre abscissa */
#define Ypad        0       * centre ordinate */
#define Gapwd       700     /* width of the gap */
#define Inplx       6000    /* length of the inner plate */
#define Inply       170     /* width of the inner plate */
#define Brgwd       100     /* width of the bridge */
#define M1wid       30      /* width of metal1 line */
#define M1exni      75      /* extension of metal1 line*/
#define M1exn       100     /* extension of metal1 line outside sensor wire */
#define Polywid     30      /* width of the poly resistor */
#define Polygap     35      /* gap between the poly lines */
#define Polylen     1000    /* length of poly resistor */
#define Consz       35      /* half of contact size (both Mp and Ml) */
#define Brggap      50      /* gap between the two bridges */
#define Plgap       50      /* gap between the two plates */
#define Splwid      180     /* sensor plate width */
#define Splbrg      120     /* sensor plate bridge width */
#define Splmetl     30      /* sensor plate metal line width */
#define Smlgap      0       /* sensor plate gap between the meatl line */
#define Smldis      40      /* sensor plate metal line distance from the edge */
#define Pd          25      /* perpendicular distance so as to avoid acute
                                    angles in the polygon */
```

```
#define TRUE    1
#define FALSE   0

/* IAen = 25 Nplus enclosure of Active */
/* NAen = 40 Nwell enclosure of Active */
/* WAen = 40 Pwell enclosure of Active */
/* JAen = 25 Pplus enclosure of Active */


int  i,ix,iy;


main()
{
 ix = Xpad+Inplx/2;
 iy = Ypad+Inply/2;


 start_cell("O3plw1");

  i = TRUE ;                    /*setting up the flag*/

  layer ( active );
   cavity4();

  layer ( cut );
   cavity4();

  layer ( via );
   cavity4();

  layer ( glass );
   cavity4();

  metal1_line();

  layer ( nplus );
   box(-(ix+Gapwd+IAen),-(iy+Gapwd+IAen), ix+Gapwd+IAen,iy+Gapwd+IAen);
   printf("coordinates of the nplus box: %d,%d %d,%d\n", -(ix+Gapwd+IAen),
         -(iy+Gapwd+IAen),ix+Gapwd+IAen,iy+Gapwd+IAen);

  layer ( nwell );
   box(-(ix+Gapwd+NAen),-(iy+Gapwd+NAen), ix+Gapwd+NAen,iy+Gapwd+NAen);
   printf("coordinates of the nwell box: %d,%d %d,%d\n", -(ix+Gapwd+NAen),
         -(iy+Gapwd+NAen), ix+Gapwd+NAen,iy+Gapwd+NAen);

  define_points();

 end_cell();
exit(0);
}



/* subroutine to define the points */
define_points()
{
```

```
 defn ( "sus_cnt", Xpad,Ypad);
  printf("defined point `sus_cnt' co-ordinates  %d,%d\n", Xpad,Ypad);
 defn ( "nw", -(ix+Gapwd),(iy+Gapwd));
  printf("defined point `nw' co-ordinates  %d,%d\n", -(ix+Gapwd),
         (iy+Gapwd));
 defn ( "sw", -(ix+Gapwd),-(iy+Gapwd));
  printf("defined point `sw' co-ordinates  %d,%d\n", -(ix+Gapwd),
         -(iy+Gapwd));
 defn ( "ne", (ix+Gapwd),(iy+Gapwd));
  printf("defined point `ne' co-ordinates  %d,%d\n", (ix+Gapwd),
         (iy+Gapwd));
 defn ( "se", (ix+Gapwd),-(iy+Gapwd));
  printf("defined point `se' co-ordinates  %d,%d\n", (ix+Gapwd),
         -(iy+Gapwd));

 defn ( "nwi", -(ix),(iy));
  printf("defined point `nwi' co-ordinates  %d,%d\n", -(ix),
         (iy));
 defn ( "swi", -(ix),-(iy));
  printf("defined point `swi' co-ordinates  %d,%d\n", -(ix),
         -(iy));
 defn ( "nei", (ix),(iy));
  printf("defined point `nei' co-ordinates  %d,%d\n", (ix),
         (iy));
 defn ( "sei", (ix),-(iy));
  printf("defined point `sei' co-ordinates  %d,%d\n", (ix),
         -(iy));

}

/* end subroutine define_points() */



/* subroutine, given a side of an isoceles right triangle, calculates the
   integer hypotenuse of the triangle */
int hypo_dis(howwide)
int howwide;
{
  int b1,c1,d1;
  float a1;

 a1 = 1.414;

 b1 = (int) howwide*a1;
 c1 = b1%5;
 d1 = b1 - c1;
 return(d1);
 }

/* end subroutine hypo_dis() */



/* subroutine, given the hypotenuse, calculates the side(integer) of an
   isolceles right triangle */
int vert_dis(howwide)
int howwide;
```

```
{
 int    b1,c1,d1;
 float  a1;

 a1 = 0.707;

 b1 = (int) howwide*a1;
 c1 = b1%5;
 d1 = b1 - c1;
 return(d1);
}
/* end subroutine vert_dis() */



/* subroutine to find the smaller side of the inner plate */
int min()
{ int min;

 if ( Inplx > Inply )
   min = Inply/2;
 else
   min = Inplx/2;

 return(min);

}
/* end subroutine min() */



/* subroutine to generate the four cavity polygons */
cavity4()
{
 int    a1,b1,c1,d1,g1,h1,x1,x2,y1,y2,xi,xo,yi,yo;
 int    a2,i1,j1,k1,l1,p1,n1,o1;
 float  e1,f1;


 a1 = hypo_dis(Brggap);
 b1 = sqrt(2.0*a1*a1);
 c1 = hypo_dis(Splbrg);
 d1 = vert_dis(Brgwd);
 e1 = sqrt(2.0*d1*d1);
 f1 = sqrt(2.0*min()*min());
 x1 = ix-d1;
 x2 = ix+Gapwd-Pd-d1;
 y1 = iy-d1;
 y2 = iy+Gapwd-Pd-d1;
 xi = ix;
 xo = ix+Gapwd;
 yi = iy;
 yo = iy+Gapwd;
 g1 = (yo-Pd)-(yi+Plgap+Splwid);
 h1 = (yo-Pd)-(yi+Plgap);

/* west polygon */
 polygon(-xi,y1, -xo+Pd,y2, -xo,y2, -xo,-y2, -xo+Pd,-y2, -xi,-y1, END );
```

```
/* east polygon */
  polygon(xi,-y1, xo-Pd,-y2, xo,-y2, xo,y2, xo-Pd,y2, xi,y1, END );

/* north polygon structure */
  polygon(x1,yi, x2,yo-Pd, x2,yo, x2-a1,yo, x2-a1,yo-Pd, x2-a1-h1,yi+Plgap,
        -x2+a1+h1,yi+Plgap, -x2+a1,yo-Pd, -x2+a1,yo, -x2,yo, -x2,yo-Pd,
        -x1,yi, END );
  polygon(x2-a1-c1,yo, x2-a1-c1,yo-Pd, x2-a1-c1-g1,yi+Plgap+Splwid,
        -x2+a1+c1+g1,yi+Plgap+Splwid, -x2+a1+c1,yo-Pd,
        -x2+a1+c1,yo, END );

/* south polygon structure */
  polygon(x1,-yi, x2,-(yo-Pd), x2,-yo, x2-a1,-yo, x2-a1,-(yo-Pd),
        x2-a1-h1,-(yi+Plgap), -x2+a1+h1,-(yi+Plgap), -x2+a1,-(yo-Pd),
        -x2+a1,-yo, -x2,-yo, -x2,-(yo-Pd), -x1,-yi, END );
  polygon(x2-a1-c1,-yo, x2-a1-c1,-(yo-Pd), x2-a1-c1-g1,-(yi+Plgap+Splwid),
        -x2+a1+c1+g1,-(yi+Plgap+Splwid), -x2+a1+c1,-(yo-Pd),
        -x2+a1+c1,-yo, END );

  if ( i == TRUE )
  {

   /* printf statements of the co-ordinates of the polygon */
   printf("west polygon co-ordinates - %d,%d, %d,%d, %d,%d, %d,%d, %d,%d, %d,%d\n", -xi,y1,
-xo+Pd,y2, -xo,y2, -xo,-y2, -xo+Pd,-y2, -xi,-y1);
   printf("east polygon co-ordinates - %d,%d, %d,%d, %d,%d, %d,%d, %d,%d, %d,%d\n", xi,-y1, xo-Pd,-y2,
xo,-y2, xo,y2, xo-Pd,y2, xi,y1);
   printf("north separating polygon co-ordinates - %d,%d, %d,%d, %d,%d, %d,%d, %d,%d, %d,%d, %d,%d,
%d,%d, %d,%d, %d,%d, %d,%d, %d,%d\n", x1,yi,
         x2,yo-Pd, x2,yo, x2-a1,yo, x2-a1,yo-Pd, x2-a1-h1,yi+Plgap,
        -x2+a1+h1,yi+Plgap, -x2+a1,yo-Pd, -x2+a1,yo, -x2,yo, -x2,yo-Pd,
        -x1,yi);
   printf("north polygon co-ordinates - %d,%d, %d,%d, %d,%d, %d,%d, %d,%d, %d,%d\n", x2-a1-c1,yo,
x2-a1-c1,yo-Pd, x2-a1-c1-g1,yi+Plgap+Splwid,
         -x2+a1+c1+g1,yi+Plgap+Splwid, -x2+a1+c1,yo-Pd,
         -x2+a1+c1,yo);
   printf("south separating polygon co-ordinates - %d,%d, %d,%d, %d,%d, %d,%d, %d,%d, %d,%d, %d,%d,
%d,%d, %d,%d, %d,%d, %d,%d, %d,%d\n", x1,-yi,
        x2,-(yo-Pd), x2,-yo, x2-a1,-yo, x2-a1,-(yo-Pd),
        x2-a1-h1,-(yi+Plgap), -x2+a1+h1,-(yi+Plgap), -x2+a1,-(yo-Pd),
        -x2+a1,-yo, -x2,-yo, -x2,-(yo-Pd), -x1,-yi);
   printf("north polygon co-ordinates - %d,%d, %d,%d, %d,%d, %d,%d, %d,%d, %d,%d\n", x2-a1-c1,-yo,
x2-a1-c1,-(yo-Pd), x2-a1-c1-g1,-(yi+Plgap+Splwid),
        -x2+a1+c1+g1,-(yi+Plgap+Splwid), -x2+a1+c1,-(yo-Pd),
        -x2+a1+c1,-yo);

    i1 = hypo_dis(Splmetl);
    j1 = hypo_dis(Smldis);
    k1 = hypo_dis(Smlgap);
    p1 = vert_dis(Splmetl);
    n1 = vert_dis(Smlgap);
    l1 = i1+j1+k1;
    o1 = p1+n1;
    layer ( metal1 );
    {
/* north sensor including metal lines and poly resistor */
    polygon(-x2+a1+j1,yo+M1exn, -x2+a1+j1,yo-Pd, -x2+a1+h1,yi+Plgap+j1,
          -x2+a1+h1+p1,yi+Plgap+j1, -x2+a1+h1+p1,yi+Plgap+j1+p1,
```

```
        -x2+a1+h1+p1-(yo-(Pd+yi+Plgap+j1+p1)),yo-Pd,
        -x2+a1+h1+p1-(yo-(Pd+yi+Plgap+j1+p1)),yo+M1exn, END );
    printf("north plate west metal1 line %d,%d, %d,%d, %d,%d, %d,%d, %d,%d, %d,%d, %d,%d\n",
-x2+a1+j1,yo+M1exn, -x2+a1+j1,yo-Pd, -x2+a1+h1,yi+Plgap+j1,
         -x2+a1+h1+p1,yi+Plgap+j1, -x2+a1+h1+p1,yi+Plgap+j1+p1,
        -x2+a1+h1+p1-(yo-(Pd+yi+Plgap+j1+p1)),yo-Pd,
        -x2+a1+h1+p1-(yo-(Pd+yi+Plgap+j1+p1)),yo+M1exn);

    box(-x2+a1+h1,yi+Plgap+j1, -x2+a1+h1+Consz,yi+Plgap+j1+2*Consz);
    box(-x2+a1+h1-Consz,yi+Plgap+j1+Consz,
       -x2+a1+h1+Consz,yi+Plgap+j1+2*Consz);
     printf("north plate west metal1 box  %d,%d, %d,%d\n", -x2+a1+h1,yi+Plgap+j1,
-x2+a1+h1+p1+o1,yi+Plgap+j1+o1+p1);
     printf("north plate west metal1 box  %d,%d, %d,%d\n", -x2+a1+h1-Consz,yi+Plgap+j1+Consz,
-x2+a1+h1+Consz,yi+Plgap+j1+2*Consz);

  Ml(-x2+a1+j1,yo+M1exn);
   printf("north plate west Ml contact position - %d,%d\n", -x2+a1+j1,yo+M1exn);

    polygon(x2-a1-j1,yo+M1exn, x2-a1-j1,yo-Pd, x2-a1-h1,yi+Plgap+j1,
         x2-a1-h1-p1,yi+Plgap+j1, x2-a1-h1-p1,yi+Plgap+j1+p1,
        x2-a1-h1-p1+(yo-(Pd+yi+Plgap+j1+p1)),yo-Pd,
        x2-a1-h1-p1+(yo-(Pd+yi+Plgap+j1+p1)),yo+M1exn, END );
    printf("north plate east metal1 line  %d,%d, %d,%d, %d,%d, %d,%d, %d,%d, %d,%d, %d,%d\n", x2-
a1-j1,yo+M1exn, x2-a1-j1,yo-Pd, x2-a1-h1,yi+Plgap+j1,
         x2-a1-h1-p1,yi+Plgap+j1, x2-a1-h1-p1,yi+Plgap+j1+p1,
        x2-a1-j1-i1,yo-Pd, x2-a1-j1-i1,yo+M1exn);

    box(x2-a1-h1,yi+Plgap+j1, x2-a1-h1-Consz,yi+Plgap+j1+2*Consz);
    box(x2-a1-h1+Consz,yi+Plgap+j1+Consz, x2-a1-h1-Consz,yi+Plgap+j1+2*Consz);
     printf("north plate east metal1 box  %d,%d, %d,%d\n", x2-a1-h1,yi+Plgap+j1, x2-a1-h1-p1-
o1,yi+Plgap+j1+o1+p1);
     printf("north plate east metal1 box  %d,%d, %d,%d\n", x2-a1-h1+Consz,yi+Plgap+j1+Consz, x2-a1-
h1-Consz,yi+Plgap+j1+2*Consz);

/* south sensor structure */
    polygon(-x2+a1+j1,-(yo+M1exn), -x2+a1+j1,-(yo-Pd),
         -x2+a1+h1,-(yi+Plgap+j1),
         -x2+a1+h1+p1,-(yi+Plgap+j1), -x2+a1+h1+p1,-(yi+Plgap+j1+p1),
        -x2+a1+h1+p1-(yo-(Pd+yi+Plgap+j1+p1)),-(yo-Pd),
        -x2+a1+h1+p1-(yo-(Pd+yi+Plgap+j1+p1)),-(yo+M1exn), END );
    printf("south plate west metal1 line  %d,%d, %d,%d, %d,%d, %d,%d, %d,%d, %d,%d, %d,%d\n",
-x2+a1+j1,-(yo+M1exn), -x2+a1+j1,-(yo-Pd),
         -x2+a1+h1,-(yi+Plgap+j1),
         -x2+a1+h1+p1,-(yi+Plgap+j1), -x2+a1+h1+p1,-(yi+Plgap+j1+p1),
        -x2+a1+h1+p1-(yo-(Pd+yi+Plgap+j1+p1)),-(yo-Pd),
        -x2+a1+h1+p1-(yo-(Pd+yi+Plgap+j1+p1)),-(yo+M1exn));

    box(-x2+a1+h1,-(yi+Plgap+j1), -x2+a1+h1+Consz,-(yi+Plgap+j1+2*Consz));
    box(-x2+a1+h1-Consz,-(yi+Plgap+j1+Consz),
       -x2+a1+h1+Consz,-(yi+Plgap+j1+2*Consz));
     printf("south plate west metal1 box  %d,%d, %d,%d\n", -x2+a1+h1,-(yi+Plgap+j1),
-x2+a1+h1+p1+o1,-(yi+Plgap+j1+o1+p1));

  Ml(-x2+a1+j1,-(yo+M1exn));
   printf("south plate west Ml contact position - %d,%d\n", -x2+a1+j1,-(yo+M1exn));

    polygon(x2-a1-j1,-(yo+M1exn), x2-a1-j1,-(yo-Pd),
```

```
          x2-a1-h1,-(yi+Plgap+j1),
          x2-a1-h1-p1,-(yi+Plgap+j1), x2-a1-h1-p1,-(yi+Plgap+j1+p1),
          x2-a1-h1-p1+(yo-(Pd+yi+Plgap+j1+p1)),-(yo-Pd),
          x2-a1-h1-p1+(yo-(Pd+yi+Plgap+j1+p1)),-(yo+M1exn), END );
      printf("south plate east metal1 line  %d,%d, %d,%d, %d,%d, %d,%d, %d,%d, %d,%d, %d,%d\n", x2-
a1-j1,-(yo+M1exn), x2-a1-j1,-(yo-Pd),
          x2-a1-h1,-(yi+Plgap+j1),
          x2-a1-h1-p1,-(yi+Plgap+j1), x2-a1-h1-p1,-(yi+Plgap+j1+p1),
          x2-a1-j1-i1,-(yo-Pd), x2-a1-j1-i1,-(yo+M1exn));

    box(x2-a1-h1,-(yi+Plgap+j1), x2-a1-h1-Consz,-(yi+Plgap+j1+2*Consz));
    box(x2-a1-h1+Consz,-(yi+Plgap+j1+Consz),
       x2-a1-h1-Consz,-(yi+Plgap+j1+2*Consz));
     printf("south plate east metal1 box  %d,%d, %d,%d\n",
          x2-a1-h1,-(yi+Plgap+j1), x2-a1-h1-p1-o1,-(yi+Plgap+j1+o1+p1));
     printf("south plate east metal1 box  %d,%d, %d,%d\n",
          x2-a1-h1+Consz,-(yi+Plgap+j1+Consz),
          x2-a1-h1-Consz,-(yi+Plgap+j1+2*Consz));

  }


/* north sensor structure */
    Ml(x2-a1-j1,yo+M1exn);
     printf("north plate east Ml contacts position - %d,%d\n",
          x2-a1-j1,yo+M1exn);

     Mp(-x2+a1+h1+p1+o1,yi+Plgap+j1+Consz);
    Mp(x2-a1-h1-p1-o1,yi+Plgap+j1+Consz);
     printf("north plate west Mp contacts position - %d,%d\n",
          -x2+a1+h1+p1+o1,yi+Plgap+j1+Consz);
     printf("north plate east Mp contacts position - %d,%d\n",
          x2-a1-h1-p1-o1,yi+Plgap+j1+Consz);

   layer ( poly );
    box(-x2+a1+h1+p1+o1-Consz,yi+Plgap+j1, x2-a1-h1-p1-o1+Consz,
       yi+Plgap+j1+Polywid);
     printf("north plate poly box %d,%d, %d,%d\n",
          -x2+a1+h1+p1+o1-Consz,yi+Plgap+j1,
          x2-a1-h1-p1-o1+Consz, yi+Plgap+j1+Polywid);


/* south sensor structure */
    Ml(x2-a1-j1,-(yo+M1exn));
     printf("south plate east Ml contacts position - %d,%d\n",
          x2-a1-j1,-(yo+M1exn));

     Mp(-x2+a1+h1+p1+o1,-(yi+Plgap+j1+Consz));
    Mp(x2-a1-h1-p1-o1,-(yi+Plgap+j1+Consz));
     printf("south plate west Mp contacts position - %d,%d\n",
          -x2+a1+h1+p1+o1,-(yi+Plgap+j1+Consz));
     printf("south plate east Mp contacts position - %d,%d\n",
          x2-a1-h1-p1-o1,-(yi+Plgap+j1+Consz));
    layer ( poly );
    box(-x2+a1+h1+p1+o1-Consz,-(yi+Plgap+j1), x2-a1-h1-p1-o1+Consz,
       -(yi+Plgap+j1+Polywid));
     printf("south plate poly box %d,%d, %d,%d\n",
          -x2+a1+h1+p1+o1-Consz,-(yi+Plgap+j1),
```

```
        x2-a1-h1-p1-o1+Consz, -(yi+Plgap+j1+Polywid));

  if ( e1 > f1 )
   printf("Error: the bridge is too wide. Undesirable structure results.\n");

   printf("actual width of the bridge =  %f\n", e1);

    i = FALSE;
  }
}
/* end subroutine cavity4() */



/* subroutine to draw the metal lins and the poly resistor */
metal1_line()
{
 int  m1xi,m1yi,m1xo,m1yo,d1;
 int  disx,dis,polyturns,endpoly;
 float compfact;
 int    y1,y2,y3,y4,xst,xst1,xst2,xst3,xend,j,k,l;

 m1xi = ix-M1exni;
 m1yi = iy-M1exni;
 m1xo = ix+Gapwd+M1exni;
 m1yo = iy+Gapwd+M1exni;

 d1 = vert_dis((int) M1wid/2);

 layer ( metal1 );
 {
 polygon(-(m1xo+d1),-(m1yo-d1), -(m1xi+d1),-(m1yi-d1), -(m1xi-d1),-(m1yi-d1),
      -(m1xi-d1),-(m1yi+d1), -(m1xo-d1),-(m1yo+d1),-(m1xo+d1),-(m1yo+d1),
       END );
 polygon((m1xo+d1),-(m1yo-d1), (m1xi+d1),-(m1yi-d1), (m1xi-d1),-(m1yi-d1),
      (m1xi-d1),-(m1yi+d1), (m1xo-d1),-(m1yo+d1), (m1xo+d1),-(m1yo+d1),
       END );
 }

 Mp(-(m1xi-d1),-(m1yi-d1));
  printf("centre plate west Mp contact position - %d,%d\n", -(m1xi-d1),-(m1yi-d1));

 Mp((m1xi-d1),-(m1yi-d1));
  printf("centre plate east Mp contact position - %d,%d\n", (m1xi-d1),-(m1yi-d1));

 layer ( poly );
  box(-(m1xi-d1),-(m1yi-d1)-Polywid/2, (m1xi-d1),-(m1yi-d1)+Polywid/2);
   printf("centre plate poly box co-ordinates - %d,%d\n", -(m1xi-d1),-(m1yi-d1)-Polywid/2, (m1xi-d1),-
(m1yi-d1)+Polywid/2);

 Ml(-(m1xo-d1),-(m1yo-d1));
  printf("centre plate west Ml contact position - %d,%d\n", -(m1xo-d1),-(m1yo-d1));

 Ml((m1xo-d1),-(m1yo-d1));
  printf("centre plate east Ml contact position - %d,%d\n", (m1xo-d1),-(m1yo-d1));

}
/* end subroutine metal1_line() */
```

Appendix B - Integrated Circuit Designs

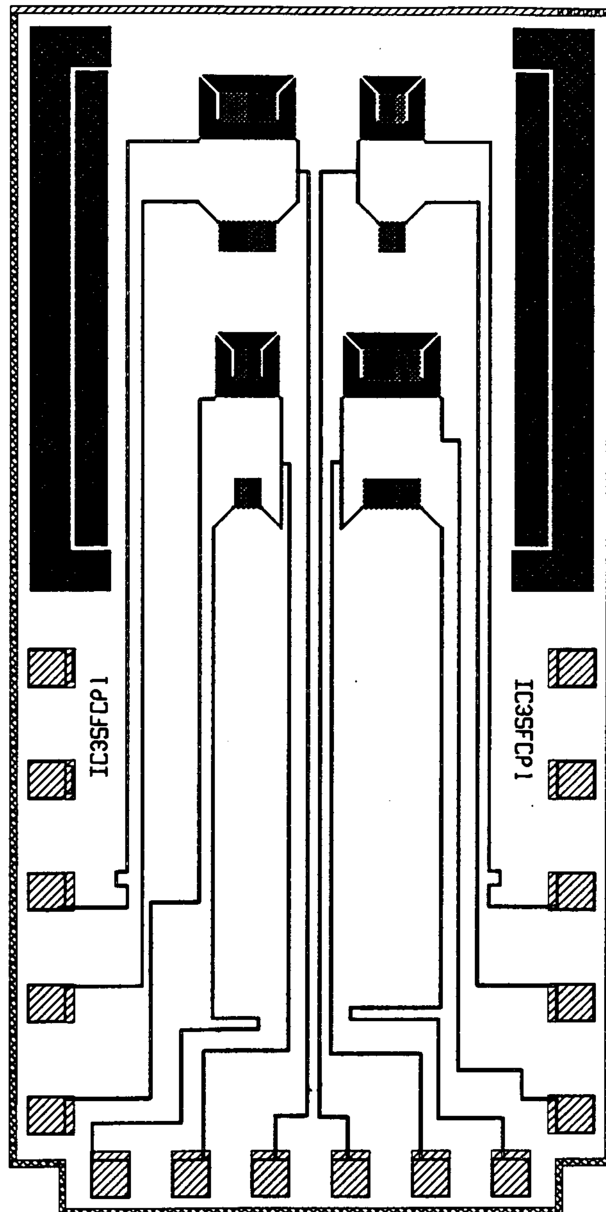

IC3SFCP1

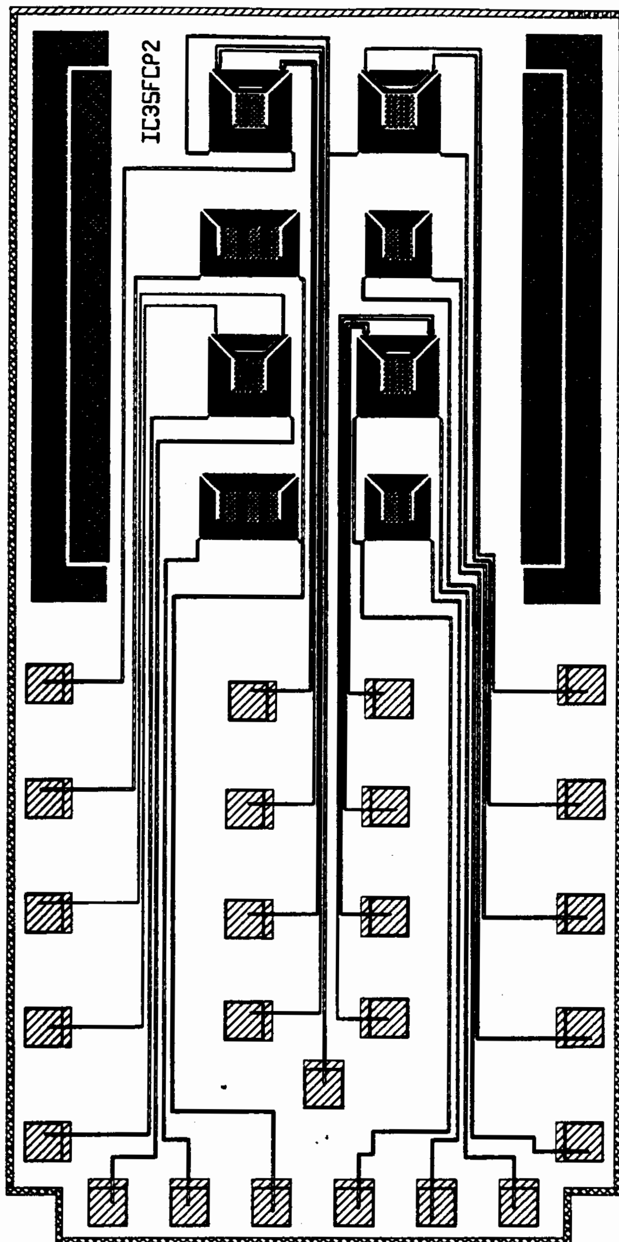

IC3SFCP2

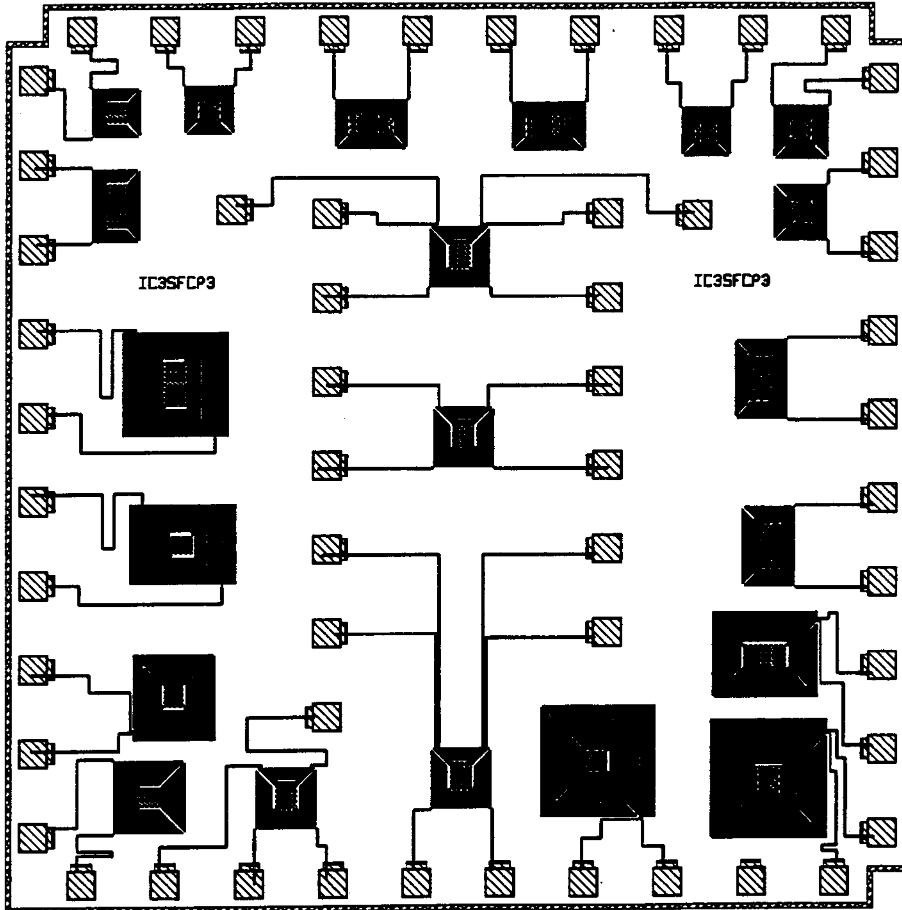

IC3SFCP3

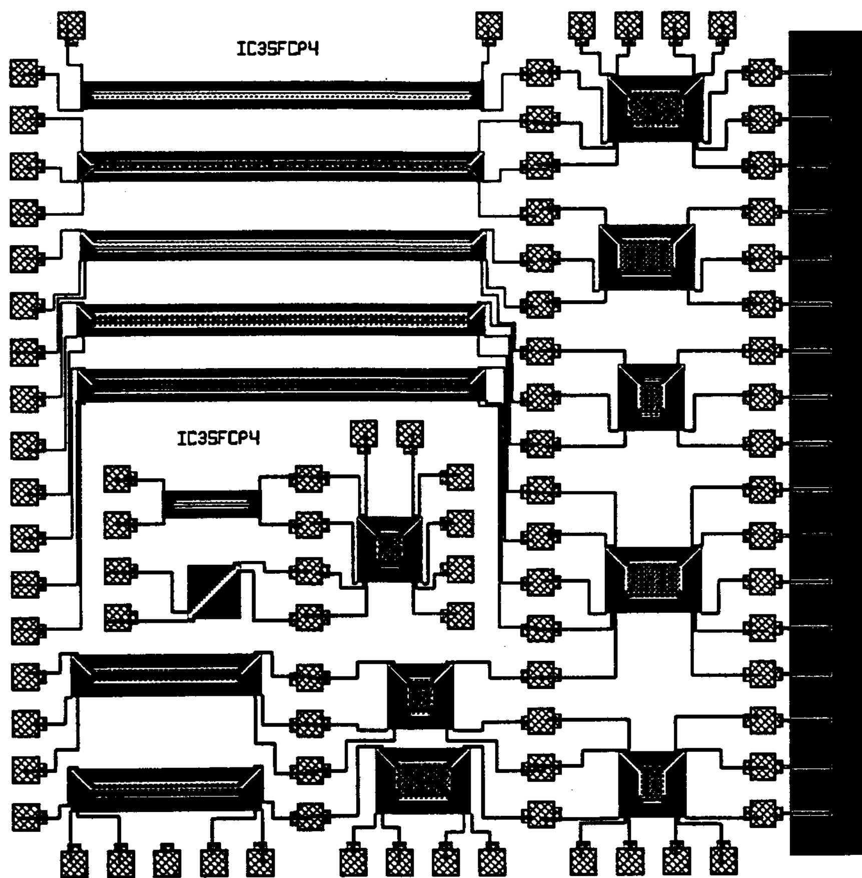

IC3SFCP4

Appendix C : ANSYS Finite Element Analysis Listings

Appendix C.1 - ANSYS 4.4 Input Listing for Thermal Conductivity Merging Example

Input Listing for 3-D Model

```
/INTER,NO
/SHOW,X11
/PREP7
/TITLE,Thermal Conductivity Merging 3-D Model
KAN,-1
ET,1,70
MP,KXX,1,1.4E-6
MP,KXX,2,2.85E-5
K,,0,0,0
K,,1,0,0
K,,1,1,0
K,,0,1,0
K,,0,0,10
K,,1,0,10
K,,1,1,10
K,,0,1,10
K,,0,1.8,0
K,,1,1.8,0
K,,0,1.8,10
K,,1,1.8,10
K,,0,2.8,0
K,,1,2.8,0
K,,0,2.8,10
K,,1,2.8,10
V,1,2,3,4,5,6,7,8
V,4,3,10,9,8,7,12,11
V,9,10,14,13,11,12,16,15
LSSEL,LINE,2,4,2
LSASEL,LINE,21,23,2
LSASEL,LINE,8,12,4
LSASEL,LINE,24,28,4
LDVS,ALL,,4
LSALL
LSSEL,LINE,1,3,2
LSASEL,LINE,14,22,8
LSASEL,LINE,6,10,4
LSASEL,LINE,18,26,8
LDVS,ALL,,4
LSALL
LSSEL,LINE,13,15,1
LSASEL,LINE,16,20,4
LDVS,ALL,,4
LSALL
LLIST
LSSEL,LINE,5,7,2
```

```
LSASEL,LINE,9,11,2
LSASEL,LINE,17,19,2
LSASEL,LINE,25,27,2
LDVS,ALL,,40
VLSEL,VOLU,1,3,2
MAT,1
TYPE,1
VMESH,ALL
VLALL
VLSEL,VOLU,2
MAT,2
TYPE,1
VMESH,2
ARSEL,AREA,1,6,5
ARASEL,AREA,7,11,4
ARASEL,AREA,12,16,4
NAREA,1
NT,ALL,TEMP,0
NALL
ARALL
KTEMP,-1
VLSEL,VOLU,2
EVOLU
QE,ALL,1E-4
EALL
VLAL
/PNUM,KPOI,1
/PNUM,LINE,1
/PNUM,AREA,1
/PNUM,MAT,1
NUMMRG,ALL
NUMC,ALL
WSORT,Z
AFWR
FINI
/EOF
```

Input Listing for 2-D Model

```
/INTER,NO
/SHOW,X11
/PREP7
/TITLE,Thermal Conductivity Merging 2-D Model
KAN,-1
ET,1,55
MP,KXX,1,2.56E-5
K
K,,1
K,,1,10
K,,,10
A,1,2,3,4
LSSE,LINE,1
LSAS,LINE,3
LDVS,ALL,,4
LSALL
```

```
LSSE,LINE,4
LSAS,LINE,2
LDVS,ALL,,40
LSALL
MAT,1
TYPE,1
AMESH,1
LSSE,LINE,1
LSAS,LINE,3
NLINE,1
NT,ALL,TEMP,0
NALL
LSALL
KTEMP,-1
QE,ALL,8E-5
/PNUM,KPOI,1
/PNUM,LINE,1
/PNUM,AREA,1
/PNUM,MAT,1
NUMMRG,ALL
NUMCMP,ALL
WSORT,Y
AFWRITE
FINI
/EOF
```

Appendix C.3 - ANSYS 4.4 Input Listing for Modeling of Structure 1 Plate Beam-type Polysilicon Resistor

```
/INTER,NO
/SHOW,X11
/PREP7
/TITLE, 1 Plate Beam-type Poly Resistor
Structure
KAN,-1
K,,0,0
/PNUM,KPOI,0
K,,5,0
K,,13,0
K,,27,0
K,,27,5
K,,84,62
K,,1580,62
K,,1580,81
K,,1580,87
K,,1580,107
K,,1580,113
K,,1580,132
K,,84,132
K,,27,189
K,,27,194
K,,13,194
K,,5,194
K,,0,194
K,,0,175
K,,5,175
K,,80,99
K,,80,94
K,,5,19
K,,0,19
KPSEL,X,0,30,1
KPSEL,Y,0,194,1
KPALL
KPSEL,Y,0,194
KPASEL,X,0,30
KPSEL,Y,194
KPASEL,X,30
KPALL
KPSEL,Y,194
KPASEL,X,90
KPSEL,Y,0,194
KPASEL,X,,90
KPSEL,Y,0
KPASEL,X,,90
KPALL
K,,13,5
K,,81,73
K,,87,73
K,,87,87
K,,5,5
```

```
K,,5,189
K,,87,107
K,,87,121
K,,81,121
K,,13,189
/PNUM,KPOI,0
KPALL
KPSEL,Y,0
KPASEL,X,,90
KPALL
KPALL
K,,102,73
K,,102,81
K,,102,87
K,,102,107
K,,102,113
K,,102,121
KSCALE,0,ALL,,,.6,.6
L,1,2
L,2,3
L,3,4
L,4,5
L,5,6
L,6,7
L,7,8
L,8,9
L,9,10
L,10,11
L,11,12
L,12,13
L,13,14
L,14,15
L,15,16
L,16,17
L,17,18
L,18,19
L,19,20
L,20,21
L,21,22
L,22,23
L,23,24
L,24,1
L,25,26
L,26,27
L,27,28
L,28,29
L,29,2
LSSEL,LINE,25,29,1
LSALL
L,30,31
L,31,32
L,32,33
L,33,34
L,34,16
L,35,36
L,36,37
L,37,28
L,38,39
L,39,40
L,40,32
L,3,25
L,17,30
L,27,35
L,31,38
L,36,8
L,9,37
L,31,9
L,10,33
LDELE,47,48,1
L,38,10
L,11,39
LDELE,6,12,1
LDEL,45,45,1,    0
LDEL,46,46,1,    0
LDEL,47,47,1,    0
LDEL,48,48,1,    0
KPSEL,KPOI,7,12,1
KSCALE,0,7,12,1,.2405
KPALL
KPALL
L,6,7
L,7,8
L,8,9
L,9,10
L,10,11
L,11,12
L,12,13
L,36,8
L,37,9
L,38,10
L,39,11
ET,1,55
LDVS,1
LDVS,1,,1
LDVS,2,,1
LDVS,3,,1
LDVS,4,,1
LDVS,5,,5
LDVS,6,,19
LDVS,5,,6
LDVS,7,,2
LDVS,8,,1
LDVS,9,,2
LDVS,9,,3
LDVS,7,,3
LDVS,10,,1
LDVS,11,,3
LDVS,12,,19
LDVS,13,,6
LDVS,14,,1
LDVS,15,,1
LDVS,16,,1
LDVS,17,,1
LDVS,18,,1
LDVS,19,,1
LDVS,20,,7
```

```
LDVS,21,,1
LDVS,22,,7
LDVS,23,,1
LDVS,24,,1
LDVS,25,,1
LDVS,24,,1
LDVS,25,,5
LDVS,25,,6
LDVS,26,,1
LDVS,27,,1
LDVS,27,,2
LDVS,28,,7
LDVS,29,,1
LDVS,30,,1
LDVS,30,,7
LDVS,31,,2
LDVS,32,,1
LDVS,33,,6
LDVS,34,,1
LDVS,35,,1
LDVS,36,,1
LDVS,37,,1
LDVS,38,,1
LDVS,39,,1
LDVS,40,,1
LDVS,41,,1
LDVS,42,,1
LDVS,43,,1
LDVS,44,,1
LDVS,45,,1
LDVS,45,,18
LDVS,46,,18
LDVS,47,,18
LDVS,48,,18
LSSEL,LINE,3,7,1
LSASEL,LINE,25,26,1
LSASEL,LINE,41,45,2
LSASEL,LINE,35
AL,ALL
LSALL
LSSEL,LINE,11,15,1
LSASEL,LINE,32,34,1
LSASEL,LINE,39,40,1
LSASEL,LINE,48
AL,ALL
LSALL
LSSEL,LINE,1,9,8
LSASEL,LINE,28,30,1
LSASEL,LINE,37,47,10
LSASEL,LINE,42,46,2
LSASEL,LINE,17,24,1
AL,ALL
LSALL
LSSEL,LINE,2,41,39
LSASEL,LINE,25,29,1
AL,ALL
LSALL
LSSEL,LINE,16,42,26
LSASEL,LINE,30,34,1
AL,ALL
LSALL
LSSEL,LINE,27,43,16
LSASEL,LINE,35,37,1
AL,ALL
LSALL
LSSEL,LINE,31,44,13
LSASEL,LINE,38,40,1
AL,ALL
LSALL
LSSEL,LINE,8,36,28
LSASEL,LINE,45,46,1
AL,ALL
LSALL
LSSEL,LINE,10,38,28
LSASEL,LINE,47,48,1
AL,ALL
LSALL
MPTEMP,1,0,22,50,75,100,125
MPTEMP,7,150,175,200,225,250
MPDATA,KXX,1,1,5.377E-6,5.538E-6,5.727E-
6,5.881E-6,6.021E-6,6.146E-6
MPDATA,KXX,1,7,6.257E-6,6.353E-6,6.436E-
6,6.504E-6,6.557E-6
MPDATA,KXX,2,1,1.468E-4,1.414E-4,1.355E-
4,1.311E-4,1.273E-4,1.240E-4
MPDATA,KXX,2,7,1.211E-4,1.185-4,1.161E-
4,1.140E-4,1.121E-4
MPDATA,KXX,3,1,2.827E-4,2.618E-4,2.407E-
4,2.255E-4,2.129E-4,2.022E-4
MPDATA,KXX,3,7,1.931E-4,1.852E-4,1.782E-
4,1.721E-4,1.666E-4
MPDATA,KXX,4,1,1.428E-4,1.276E-4,1.125E-
4,1.019E-4,9.332E-5,8.615E-5
MPDATA,KXX,4,7,8.008E-5,7.489E-5,7.039E-
5,6.645E-5,6.297E-5
MPDATA,KXX,5,1,2.406E-8,2.576E-8,2.787E-
8,2.971E-8,3.150E-8,3.325E-8,
MPDATA,KXX,5,7,3.496E-8,3.662E-8,3.823E-
8,3.980E-8,4.133E-8
MAT,1
TYPE,1
AMESH,1,3,1
MAT,2
AMESH,4,5,1
MAT,3
AMESH,6,7,1
MAT,4
AMESH,8,9,1
ET,2,33
R,1,37.189
MP,KXX,5,5
NGEN,2,1000,ALL,,,,,-20.0
MAT,5
REAL,1
TYPE,2
E,1,1001
```

```
EGEN,255,1,227
/PNUM,MAT,1
NUMMRG,ALL
NUMCMP,ALL
WSORT,X
LSSE,LINE,15
LSAS,LINE,16
LSAS,LINE,17
LSAS,LINE,18
LSAS,LINE,24
LSAS,LINE,1
LSAS,LINE,2
LSAS,LINE,3
NLINE,1
NASEL,Z,-20
NT,ALL,TEMP,22
NALL
LSALL
/PBC,ALL,1
ARSEL,AREA,9
EAREA
QEDEL,ALL
/COM, KTEMP,-1
/COM, QE,ALL,1.042E-12
EALL
ARALL
ARSEL,AREA,8
EAREA
KTEMP,-1
QE,ALL,1.042E-12
EALL
ARALL
ITER,5,1,1
CNVR,1,,,,0,5
KBC,1
LWRITE
AFWRITE
FINISH
```

```
/INPUT,27
FINISH
```

```
/POST1
STRESS,THER
SET
NSEL,NODE,77,183,106
NASEL,NODE,117,134,1
NASEL,NODE,186,203,1
/OUTPUT,STEMP
PRTEMP
/OUTPUT
NALL
NSEL,NODE,29
NASEL,NODE,32,49,1
NASEL,NODE,164,182,1
/OUTPUT,HTEMP
PRTEMP
/OUTPUT
NALL
/SHOW,PLOTFILE
PLNSTR,TEMP
/SHOW,UNUSED
/SHOW,X11
FINI
/EOF
```

Appendix C.3 - ANSYS 4.4 Input Listing for Modeling of Structure 3 Plate Beam-type Polysilicon Resistor

```
/INTER,NO
/SHOW,X11
/PREP7
/TITLE, 3 Plate Beam-type Poly Resistor
Structure
KAN,-1
K,1,-143,-147
K,2,-138,-152
K,3,-124,-152
K,4,-113,-152
K,5,-105,-152
K,6,-91,-152
K,7,-2,-63
K,8,583,-63
K,9,583,-44
K,10,583,-38
K,11,583,-27
K,12,583,-17
K,13,583,-3
K,14,583,3
K,15,583,17
K,16,583,27
K,17,583,38
K,18,583,44
K,19,583,63
K,20,-2,63
K,21,-91,152
K,22,-105,152
K,23,-113,152
K,24,-124,152
K,25,-138,152
K,26,-152,138
K,27,-17,3
K,28,-17,-3
K,29,-152,-138
K,30,-147,-143
K,31,-3,-7
K,32,7,-7
K,53,7,-3
K,33,7,3
K,34,7,7
K,35,-7,7
K,36,-7,-3
K,37,1,-46
K,38,1,-52
K,39,16,-52
K,40,16,-44
K,41,16,-38
K,42,1,-38
K,43,1,38
K,44,16,38
```

```
K,45,16,44
K,46,16,52
K,47,1,52
K,48,1,46
K,49,1,-27
K,50,-3,-17
K,51,-3,17
K,52,1,27
KSCALE,0,ALL,,,.6,.6
/COM, lInes for Outer boundary
L,1,2
L,2,3
L,3,4
L,4,5
L,5,6
L,6,7
L,7,8
L,8,9
L,9,10
L,10,11
L,11,12
L,12,13
L,13,14
L,14,15
L,15,16
L,16,17
L,17,18
L,18,19
L,19,20
L,20,21
L,21,22
L,22,23
L,23,24
L,24,25
L,25,26
L,26,27
L,27,28
L,27,28
L,28,29
L,29,30
L,30,1
L,31,32
L,32,53
/COM, Line number corresponds to the first
number for above line inputs
/COM, Line number corresponds to the last
number for below line inputs
L,53,33
L,33,34
L,34,35
L,35,36
L,36,31
L,37,38
L,38,39
L,39,40
L,40,41
L,41,42
L,42,37
L,43,44
L,44,45
L,45,46
L,46,47
L,47,48
L,48,43
/COM, Metal Lines 50-55 (Centre,bottom,top)
L,1,31
L,36,30
L,5,37
L,4,42
L,23,43
L,48,22
/COM, Air Gap Lines 56-63(Top,bottom)
L,2,50
L,50,12
L,11,49
L,49,3
L,24,52
L,52,16
L,15,51
L,51,25
/COM, Poly Lines 64-69(Centre,bottom,top)
L,53,13
L,33,14
L,41,10
L,40,9
L,44,17
L,45,18
LDVS,1,,1
LDVS,2,,1
LDVS,3,,1
LDVS,4,,1
LDVS,5,,1
LDVS,6,,7
LDVS,7,,32
LDVS,8,,2
LDVS,9,,1
LDVS,10,,1
LDVS,11,,1
LDVS,12,,1
LDVS,13,,1
LDVS,14,,1
LDVS,15,,1
LDVS,16,,1
LDVS,17,,1
LDVS,18,,2
LDVS,19,,32
LDVS,20,,7
LDVS,21,,1
LDVS,22,,1
LDVS,23,,1
LDVS,24,,1
LDVS,25,,2
LDVS,26,,10
LDVS,27,,1
LDVS,28,,10
LDVS,29,,1
```

```
LDVS,30,,1
/COM, Contacts
LDVS,31,,1
LDVS,32,,1
LDVS,33,,1
LDVS,34,,1
LDVS,35,,1
LDVS,36,,1
LDVS,37,,1
LDVS,38,,1
LDVS,39,,1
LDVS,40,,1
LDVS,41,,1
LDVS,42,,1
LDVS,43,,1
LDVS,44,,1
LDVS,45,,1
LDVS,46,,1
LDVS,47,,1
LDVS,48,,1
LDVS,49,,1
/COM, Metal Lines
LDVS,50,,11
LDVS,51,,11
LDVS,52,,9
LDVS,53,,9
LDVS,54,,9
LDVS,55,,9
/COM, Air Lines
LDVS,56,,11
LDVS,57,,32
LDVS,58,,32
LDVS,59,,10
LDVS,60,,10
LDVS,61,,32
LDVS,62,,32
LDVS,63,,11
/COM, Poly Lines
LDVS,64,,32
LDVS,65,,32
LDVS,66,,31
LDVS,67,,31
LDVS,68,,31
LDVS,69,,31
/COM, Area Formation
/COM, SiO2 Areas(Bottom to Top)
AL,5,6,7,8,67,40,39,38,52
AL,3,53,42,66,10,58,59
AL,1,56,57,12,64,32,31,50
LSSEL,LINE,14
LSASEL,LINE,25,29,1
LSASEL,LINE,34,36,1
LSASEL,LINE,62,63,1
LSASEL,LINE,51,65,14
AL,ALL
LSALL
AL,23,60,61,16,68,44,54
AL,21,55,48,47,46,69,18,19,20
/COM, Metal Lines(Bottom to Top)
AL,52,43,53,4
AL,50,37,51,30
AL,54,49,55,22
/COM, Contact Cuts(Bottom to Top)
AL,38,39,40,41,42,43
AL,31,32,33,34,35,36,37
AL,44,45,46,47,48,49
/COM, Poly Lines(Bottom to Top)
AL,67,9,66,41
AL,64,13,65,33
AL,68,17,69,45
/COM, Air Gap(Bottom to Top)
AL,24,63,62,15,61,60
AL,2,59,58,11,57,56
/COM, Element Assignment
/COM, ET,1,35 * 6-node quadratic isoparametric
triangle
ET,1,55
ET,2,33
/COM, Material Assignment
MPTEMP,1,0,22,50,75,100,125
MPTEMP,7,150,175,200,225,250
MPDATA,KXX,1,1,5.377E-6,5.538E-6,5.727E-
6,5.881E-6,6.021E-6,6.146E-6
MPDATA,KXX,1,7,6.257E-6,6.353E-6,6.436E-
6,6.504E-6,6.557E-6
MPDATA,KXX,2,1,1.468E-4,1.414E-4,1.355E-
4,1.311E-4,1.273E-4,1.240E-4
MPDATA,KXX,2,7,1.211E-4,1.185-4,1.161E-
4,1.140E-4,1.121E-4
MPDATA,KXX,3,1,2.827E-4,2.618E-4,2.407E-
4,2.255E-4,2.129E-4,2.022E-4
MPDATA,KXX,3,7,1.931E-4,1.852E-4,1.782E-
4,1.721E-4,1.666E-4
MPDATA,KXX,4,1,1.428E-4,1.276E-4,1.125E-
4,1.019E-4,9.332E-5,8.615E-5
MPDATA,KXX,4,7,8.008E-5,7.489E-5,7.039E-
5,6.645E-5,6.297E-5
MPDATA,KXX,5,1,2.406E-8,2.576E-8,2.787E-
8,2.971E-8,3.150E-8,3.325E-8,
MPDATA,KXX,5,7,3.496E-8,3.662E-8,3.823E-
8,3.980E-8,4.133E-8
/COM, Meshing of elements
MAT,1
TYPE,1
AMESH,1,6,1
MAT,2
AMESH,7,9,1
MAT,3
AMESH,10,12,1
MAT,4
AMESH,13,15,1
MAT,5
AMESH,16,17,1
/COM, Generation of nodes for bottom air
conduction rods
NGEN,2,1000,ALL,,,,,-30.0
```

```
TYPE,2
MAT,5
R,1,53.02
E,1,1001
EGEN,627,1,605-
NUMMRG,ALL
NUMCMP,ALL
WSORT,X
LSSEL,LINE,1,5,1
LSASEL,LINE,21,25,1
LSASEL,LINE,29,30,1
NLINE,1
NT,ALL,TEMP,22
NALL
NSEL,Z,-30
NT,ALL,TEMP,22
NALL
LSAL
/PBC,ALL,1
ARSEL,AREA,13
EAREA
QEDEL,ALL
KTEMP,-1
QE,ALL,5.111E-8
EALL
ARALL
ARSEL,AREA,14
EAREA
KTEMP,-1
QE,ALL,6.843E-7
EALL
ARALL
ITER,5,1,1
CNVR,1,,,,0,5
KBC,1
LWRITE
SAVE
AFWRITE
FINISH


/INPUT,27
FINISH

/POST1
STRESS,THER
SET
NSEL,NODE,42
NASEL,NODE,44,74,1
NASEL,NODE,129,160,1
/OUTPUT,STEMP
PRTEMP
/OUTPUT
NALL
NSEL,NODE,296
NASEL,NODE,249,281,1
NASEL,NODE,378,409,1
/OUTPUT,HTEMP
PRTEMP
/VIEW,1,1,1,1
/OUTPUT
/SHOW,PLOTFILE
PLNSTR,TEMP
/SHOW,UNUSED
/SHOW,X11
FINI
/EOF
```

List of References

[1] A. Roth, Vacuum Technology, North-Holland, 1990.

[2] L.I. Maissel and R. Glang, ed., Handbook of Thin Film Technology, Chapter 2, McGraw-Hill New York, 1970, pp. 115 - 128.

[3] S. Wolf and R.N. Tauber, Silicon Processing for the VLSI Era, Volume 1, Process Technology, Lattice Press, 1986.

[4] J.R. Davy, Industrial High Vacuum, Sir Isaac Pitman & Sons, London, 1951.

[5] K. Diels and R. Jaeckel, translated by H. Adam and J. Edwards, Leybold Vacuum Handbook, Pergamon Press, 1966.

[6] G.L. Weissler and R.W. Carlson, ed., Vacuum Physics and Technology, 1979, Academic Press, New York.

[7] K.E. Peterson, "Silicon as a Mechanical Material", Proceedings of the IEEE, vol. 70, no. 5, May 1982, pp. 420 - 457.

[8] R.S. Muller, "Microdynamics", Sensors and Actuators, A21 - A23 (1990), pp. 1 - 8.

[9] W. Gopel, J. Hesse, J.N. Zemel, ed., T. Grandke and W.H. Ko, volume ed., Sensors - Fundamentals and General Aspects, Volume 1, VCH Publishers, 1989.

[10] R.T. Howe, R.S. Muller, K.J. Gabriel and W.S.N. Trimmer, "Silicon Micromechanics: Sensors and Actuators on a Chip", IEEE Spectrum, July 1990, pp. 29 - 35.

[11] S. Middelhoek and A.C. Hoogerwerf, "Smart Sensors: When and Where", Sensors and Actuators, 8 (1985), pp. 39 - 48.

[12] R. Schorner, M. Poppinger and J. Eibl, "Silicon Pressure Sensor with Frequency Output", Sensors and Actuators, A21 - A23, 1990, pp. 73 - 78.

[13] J. Neumeister, G. Schuster and W. von Munch, "A Silicon Pressure Sensor using MOS Ring Oscillators", Sensors and Actuators, 7, 1985, pp. 167 - 176.

[14] J.R. Mallon Jr., F. Pourahmadi, K. Peterson, P. Barth, T. Vermeullen and J. Bryzek, "Low-Pressure Sensors Employing Bossed Diaphragms and Precision Etch-Stopping", Sensors and Actuators, A21 - A23 (1990), pp. 89 -95.

[15] A.W. van Herwaarden, P.M. Sarro and H.C.Meijer, "Integrated vacuum sensor", Sensors and Actuators, 1985, pp. 187 - 196.

[16] A.W. van Herwaarden, D.C. van Duyn and J. Groeneweg, "Small-size Vacuum Sensors Based on Silicon Thermopiles", Sensors and Actuators, 1991, pp. 565 - 569.

[17] C.H. Mastrangelo and R.S. Muller, " Fabrication and Performance of a Fully Integrated Pirani Pressure Gauge with Digital Readout", Transducers 91, International conference on Solid-State Sensors and Actuators, pp. 245 - 248.

[18] J. Huang and Q. Tong, "Integrated Multi-function Sensor for Flow Velocity, Temperature and Vacuum Measurements", Sensors and Actuators, 1989, pp. 3 - 11.

[19] A.M. Robinson, P. Haswell, R.P.W. Lawson and M. Parameswaran, "A Thermal Conductivity Microstructural Pressure Sensor Fabricated in Standard Complimentary Metal-Oxide Semiconductor", Review of Scientific Instruments, 1992, pp. 2026 - 2029.

[20] S.D. James, R.G. Johnson and R.E. Higashi, "A Broad Range Absolute Pressure Microsensor", IEEE Solid-State Sensor and Actuator Workshop, 1988, pp. 107 -108.

[21] J. Bretschi, "A Single Crystal Semiconductor Vacuum Gauge with Extended Range", Journal of Physics E: Scientific Instruments, 9, 1976, pp. 261 - 262.

[22] S.M. Patel and M.D. Mahajan, "Use of GaSb films as Residual Gas Pressure Monitors", Journal of Physics E: Scientific Instruments, 14, 1981, pp. 378 - 380.

[23] M. Parameswaran, A.M. Robinson, Lj. Ristic, K. Chau and W. Allegretto, "A CMOS Thermally Isolated Gas Flow Sensor", Sensors and Materials, 2, 1 (1990), pp. 17 - 26.

[24] T.R. Ohnstein, R.G. Johnson, R.E. Higashi, D.W. Burns, J.O. Holmen, E.A. Satren and G.M. Johnson, "Environmentally Rugged, Wide Dynamic Range Microstructure Airflow Sensor", IEEE Solid-State Sensor and Actuator Workshop, 1990, pp. 158 - 160.

[25] B.W. van Oudheusden and A.W. van Herwaarden, "High-sensitivity 2-D Flow Sensor with an Etched Thermal Isolation Structure", Sensors and Actuators, A21 - A23, 1990, pp. 425 - 430.

[26] D. Moser, R. Lenggenhager and H. Baltes, "Silicon Gas Flow Sensors using Industrial CMOS and Bipolar IC Technology", Sensors and Actuators, A25 - A27 (1991), pp. 577 - 581.

[27] J. Bryzek, K. Peterson, J.R. Mallon Jr., L. Christel and F. Pourahmadi,"Silicon Sensors and Microstructures", Nova Sensor, June 1990.

[28] S. Middelhoek, P.J. French, J.H. Huijsing and W.J. Lian, "Sensors with Digital or Frequency Output", Sensors and Actuators, 1988, pp. 119 - 133.

[29] J.P. Holman, Heat Transfer, McGraw-Hill, 1990.

[30] A.W. van Herwaarden and P.M. Sarro, "Performance of Integrated Thermopile Vacuum Sensors", Journal of Physics, E: Scientific Instruments, 21, 1988, pp. 1162 - 1167.

[31] H.V. Ubisch, "On the Conduction of Heat in Rarefied Gases and its Manometric Applications", Applied Science Research, Vol. A2, pp. 364 - 440.

[32] M. Parameswaran, H.P. Baltes, Lj. Ristic, A.C. Dhaded and A.M. Robinson, "A New Approach for the Fabrication of the Micromechanical Structures", Sensors and Actuators, 19, 1989, pp. 289 - 307.

[33] M. Parameswaran, Microelectronic and Micromechanical Sensors and Actuators in CMOS Technology - a Novel Scheme Towards Regularization and Integration, Ph.D Thesis, Department of Electrical Engineering, University of Alberta, Edmonton, 1990.

[34] M.J. Syrzycki, L. Carr, G.H. Chapman and M. Parameswaran, "A Wafer Scale Visual-to-Thermal Converter", Proceedings of International Conference on Wafer Scale Integration, 1993, pp. 1 - 10.

[35] M. Parameswaran, A.M. Robinson, D.L. Blackburn, M. Gaitan and J. Geist, "Micromachined Thermal Radiation Emitter from a Commercial CMOS Process", IEEE Electron Device Letters, Vol. 12, No. 2, 1991, pp. 57 - 59.

[36] T.I. Kamins, "Design Properties of Polycrystalline Silicon", Sensors and Actuators, A21 - A23 (1990), pp. 817 - 824.

[37] E. Obermeier, P. Kopystynski and R. Niebl, "Characteristics of Polysilicon Layers and their Application in Sensors", IEEE Solid-State Sensors Workshop, 1986, pp. 83 - 86.

[38] H. Guckel, D.W. Burns, C.R. Rutgilano, D.K. Showers and J. Uglow, "Fine Grained Polysilicon and its Application to Planar Pressure Transducers", Transducers '87, Recordings of the 4th International Conference on Solid-State Sensors and Actuators, 1987, pp. 277 - 282.

[39] Northern Telecom's CMOS3 DLM process description and design rules manual.

[40] D.J. Gamble, R.F. Hobson, D.J. McKie and J.L. Simmons, C Design Language User's Manual, School of Computing Science, Simon Fraser University, 1992.

[41] R.M. Finne and D.L. Klein, "A Water-Amine-Complexing Agent System for Etching Silicon", Journal of Electrochemical Society: Solid State Science, September, 1967, pp. 965 - 970.

[42] M.L. Mead, Lock-in Amlifiers: Principles and Applications, IEE electrical measurement series, No. 1, Peregrinus London, 1983.

[43] SR850 DSP Lock-in amplifier Operating Manual, Stanford Research Systems, 1992.

[44] R. Baylor, A. Hindie, D. Melick and J. Wang, "Lock-in Amplifiers Go Digital", Lasers and Optronics, April 1991.

[46] E. Obermeier, P. Kopystynski and R. Niebl, “Characteristics of Polysilcion Layers and their Applications in Sensors”, Recordings of the IEEE Solid-State Sensors Workshop, 1986, pp.83 - 86.

[47] P.R. Bevington, Data Reduction and Error Analysis for the Physical Sciences, McGraw-Hill, 1969.

[48] Manual Corona SFU sputter coater system.

[49] Instruction manual, Series 275 Mini-convectron vacuum gauges with analog output and process relay, Granville-Phillips Co., Boulder, Colorado, USA.

[50] Operating instructions, Varian ratiomatic gauge controls, Varian, Lexington, Massachusetts, USA.

[51] S. Dushman, Scientific Foundations of Vacuum Technique, John Wiley and Sons, 1962.

[52] D.L. Logan, A First Course in the Finite-Element Method, PWS-KENT Publishing Company, Boston, 1992.

[53] H.A. Schafft, J.S. Suehle and P.G.A. Mirel, "Thermal Conductivity Measurements of Thin-Film Silicon Dioxide", Proceedings IEEE 1989 International Conference on Microelectronic Test Structures, Vol. 2, No. 1, March 1989, pp. 121 - 125.

[54] R.W. Powell, C.Y. Ho and P.E. Liley, "Thermal Conductivity of Selected Materials", NSRDS-NBS 8, Nov. 25, 1966, pp. 100 - 106.

[55] S.S. Cohen and G.H. Chapman, "Laser Beam Processing and Wafer-Scale Integration", VLSI Electronics: Microstructure Science, Vol. 21, pp. 19 - 111.

[56] F. Volklein and H. Baltes, "A Microstructure for Measurement of Thermal Conductivity of Polysilicon Thin Films", Journal of Microelectromechanical Systems, Vol. 1, No. 4, Dec. 1992, pp. 193 - 196.

[57] S.S. Cohen, P.W. Wyatt and G.H. Chapman, "Laser-Induced Melting of Thin Conducting Films: Part I-The Adiabatic ASpproximation", IEEE transactions on Electron Devices, Vol.38, No. 9, Sept. 1991, pp. 2042 - 2050.

[58] W.M. Rosenshaw, J.P. Hartnett and E.N. Ganic, editors, Handbook of Heat Transfer Fundamentals, McGraw-HillBook Company, 1985.

[59] B.W. van Oudheusden, “The Thermal Modeling of a Flow Sensor Based on Differential Convective Heat Transfer”, Sensors and Actuators A, 29 (1991), pp. 93 - 106.

[60] A.F. Kip, Fundamentals of Electricity and Magnetism, McGraw-Hill, 1969.